THE UNIVERSITY OF CHICAGO

LILAC: DESIGNING AND IMPLEMENTING A LIGHT-SENSITIVE ACTIN-BINDING PEPTIDE

A DISSERTATION SUBMITTED TO

THE FACULTY OF THE DIVISION OF THE PHYSICAL SCIENCES

AND

THE FACULTY OF THE DIVISION OF THE BIOLOGICAL SCIENCES

AND THE PRITZKER SCHOOL OF MEDICINE

IN CANDIDACY FOR THE DEGREE OF

DOCTOR OF PHILOSOPHY

GRADUATE PROGRAM IN BIOPHYSICAL SCIENCES

BY

KOURTNEY LILLIAN KROLL

CHICAGO, ILLINOIS

AUGUST 2023

To my parents, thank you for getting me here.

TABLE OF CONTENTS

LIST OF FIGURES

ACKNOWLEDGMENTS

I am deeply grateful to my mentors, Tobin Sosnick and Ron Rock, for their invaluable guidance throughout this transformative journey. Their boundless passion for science and genuine excitement in celebrating new discoveries have been contagious, making each step of this research both thrilling and rewarding. Moreover, they generously allowed me the space to explore my own ideas while providing unwavering support whenever I needed it. Learning from such humble, thorough, and creative scientists has been an extraordinary privilege. My dogs, Dexter and Maple, played a crucial role by offering comforting snuggles during long writing sessions, helping me maintain a work-life balance that kept me engaged and excited in the lab. I owe a special thanks to my partner, Evan, whose unwavering support has been a constant source of strength and inspiration. He has been my comedian during stressful times, my science advisor in moments of doubt, my best friend throughout this journey, and an exceptional dog co-parent. Without him, this path would have been much more challenging. I cannot overlook the immense sacrifices and support of my family, especially my parents. Their selfless dedication and belief in my potential allowed me to pursue my undergraduate education, ultimately leading me to the University of Chicago for graduate school. Their unwavering assistance, from chauffeuring me to and from the airport to caring for my beloved pups while I was away, has been nothing short of extraordinary. Weekends spent with them provided an invaluable opportunity to recharge, reconnect with my roots, and create cherished family memories. I love them so much.

ABSTRACT

Cytoskeletal structure and dynamics are key for cells to function. Not only does the cytoskeleton give static support to the cell, its self-organization and restructuring are critical for cytokinesis, muscle movement, lamellipodia driven cell movement and more. Visualization of the actin cytoskeleton is necessary for various fields of biological research, and there are several actin labels available. For live-cell imaging, the most popular label is Lifeact, a 17 amino-acid peptide derived from actin binding protein (ABP) 140 in yeast. Despite its use in over 7,000 studies, Lifeact has several known concentration-dependent side effects, likely due to its competitive binding with important ABPs, cofilin and myosin. I addressed this problem by creating a light-sensitive version of Lifeact that has low affinity in the dark, but high affinity for actin when excited by blue light. Using previous designs of optogenetic tools as a guide, I designed LILAC (Light-Induced Label for ACtin) by strategically integrating Lifeact into the reversibly unfolded Jα helix of AsLOV2, a photosenstive protein from oat. Reversible, light-induced recruitment of LILAC to filamentous actin was validated both in live cells and with purified proteins. Pre-illumination subtraction and correlative imaging allow for enhanced visualization of actin, and the recovery time constant can be modulated with buffer conditions. I also utilized LILAC to pattern actin filaments *in vitro*, a tool that could be applied to elucidate how components of the actin cytoskeleton are integrated spatiotemporally to form complex structures. In my thesis, I describe the development and application of LILAC as an imaging and patterning tool, though a wide array of other applications remain.

CHAPTER 1

INTRODUCTION

1.1 The measurement problem

An overarching issue in science is that as we observe things, we inevitably perturb them. This principle permeates nearly all length scales. On the quantum scale, this is known as the measurement problem. When we observe or measure the spin of a particle, we disrupt its quantum state and force it to assume a definite spin value. The act of measurement introduces an unavoidable interaction between the measured system and the measurement apparatus, leading to the collapse of the wave function and the manifestation of a particular spin state. On the ecological scale, let us use the example of birds. To observe their migration, we must track them, which can be done with several methods. The simplest method is to just observe birds in their wild habitat. Obviously this is the least intrusive, yet gives us the least resolved and least accurate data, as the observers cannot confidently know which bird they are seeing and can only study a small number of locations. Another method is to catch the birds and tag them with small labeled bands, then periodically catch them and document when and where each specific bird is. Clearly this is better than the simple observation method, as each bird can be accurately identified, but requires considerable intervention with the birds each time data is collected. The best data comes from attaching trackers that relay real-time global positioning system (GPS) data. However, these data could be from perturbed samples. For all we know, the birds with GPS trackers cannot fly for as long, are not incorporated into the flock normally, fly slower, etc. This is all to say that when we observe more thoroughly, we are often interacting with our system of interest more, until we are changing the system so much that it is no longer a good representative of the system of interest. In sum, better data, comes at a higher cost.

In the field of cellular biology, our birds are cellular molecules, and our GPS trackers

are molecular labels. The relative scales of these molecules vary widely, and often include large molecular labels for small cellular molecules. Imagine a tiny finch with a gigantic GPS tracker the size of a refrigerator; this is sometimes all we have available in our toolkit as cellular biologists. What if we could leave the birds be, but only when we wanted the GPS coordinates, the tracker magnetized instantly and appeared on the bird's foot. Then, we quickly obtain the data, and the tracker de-magnetizes and fell off. Therefore, the bird is only perturbed for the short period of time where we acquired the coordinates. This is the principle behind LILAC, a light-sensitive actin-binding peptide, where our bird is actin, a structural, cytoskeletal protein, and our tracker is a fluorescent protein.

1.2 The actin cytoskeleton

1.2.1 Introduction to the cytoskeleton

Cells require exquisite coordination to perform the various functions necessary for life. Cells crawl, grow, divide, transport cargo, and much more [Blanchoin et al., 2014]. Specific cell types such as cochlear hair cells have long protrusions to sense sound and relay the signal to the brain [Vélez-Ortega and Frolenkov, 2019]. Ciliated cells in the lungs transport foreign molecules to clear the airways and in the Fallopian tubes, they facilitate the movement of eggs and embryos through the reproductive tract [Brooks and Wallingford, 2014]. Muscle fibers contract to produce enormous force generated by small repeating structures known as sarcomeres [Rassier, 2017]. To execute these incredible tasks successfully, cells use an ever-changing architectural network known as the actin cytoskeleton.

The actin cytoskeleton consists of thin filaments of polymerized actin, a 42 kDa protein that exists in monomeric (G-actin) and filamentous states (F-actin) and forms a double-stranded right handed helix [Dominguez and Holmes, 2011]. Actin binds to adenosine triphosphate (ATP) as an energy source for polymerization, as well as an indicator of fila-

ment age [Dominguez and Holmes, 2011]. Newly formed filaments contain ATP, while older filaments contain the hydrolyzed product, ADP [Oosterheert et al., 2022]. The turnover of ATP to ADP is necessary for recycling of actin.

F-actin, in conjunction with many other actin binding proteins (ABPs), form a diverse array of substructures within cells [Kadzik et al., 2020, Michelot and Drubin, 2011]. For example, thin filaments are bundled together tightly by bundling proteins, such as fascin, to create structures including filopodia, long protrusions used for environmental sensing [Bartles, 2000, Courson and Rock, 2010, Jansen et al., 2011]. Stress fibers form by bundling actin filaments with alpha-actinin, a bundler that leaves more space between the filaments [Courson and Rock, 2010, Foley and Young, 2014, Ribeiro et al., 2014]. Vinculin, another ABP, anchors the ends of stress fibers to adhesion molecules on the outside of the cell to facilitate cell migration [Kadzik et al., 2020, Michelot and Drubin, 2011]. Protein complexes like the Arp2/3 complex create branch sites, allowing for highly intricate, dense networks of actin at the leading edge of the cell, critical for movement [Rogers et al., 2003]. These structures, known as lamellipodia, also must be disassembled at the rear of the moving cell so the parts can be recycled for use elsewhere. Along these various structures, myosin motors walk, carrying cargo around of the cell [Hartman and Spudich, 2012]. Extreme coordination of these molecules in a spatiotemporal manner is necessary for each of these processes to occur. Yet, we do not fully understand how the pool of the individual parts coalesce to perform this sophisticated orchestra of actions.

As such an integral component for a plethora of cellular processes, interruption in cytoskeletal function has implications in several diseases. Cancer growth and metastasis relies on cell division, migration and invasion. Each of these processes are highly reliant on the actin cytoskeleton, thus it is no surprise that disruption of the actin cytoskeleton is implicated in cancer [Ong et al., 2020]. Neuronal cells are highly polarized, morphologically distinct cells that require cytoskeletal coordination to form synapses and transport cellular

components long distances. In diseases such as Alzheimer's, Parkinson's, and Huntington's disease, cytoskeletal abnormalities are observed [Muñoz-Lasso et al., 2020]. As actin is a main component of muscle contraction, alterations to actin and its associated proteins have implications in cardiac diseases and muscular diseases [Parker et al., 2020, Rassier, 2017]. In total, the actin cytoskeleton is an essential structure, and dependable visualization of its structure is critical for many areas of research.

1.2.2 Cytoskeleton imaging

The visualization of actin-based structural features is critical for cell biologists. To visualize cells, we use a number of microscopy methods. One of the most common methods for visualizing cells is phase contrast microscopy, which allows for visualization of clear samples, such as single cells, and does not require labeling, staining, or other sample preparation. However, it does not specifically label cellular structures of interest. In contrast, fluorescence microscopy uses fluorescent molecules to specifically label molecules of interest within the cell. Multiple colors can be combined to image various structures simultaneously, and single molecule resolution is possible. Several different fluorescent probes can be used to label the molecule of interest within cells. Dyes like AlexaFluor dyes and quantum dots are useful tools, but can be challenging to conjugate to proteins in cells [Bera et al., 2010, Panchuk-Voloshina et al., 1999]. Green fluorescent protein (GFP), a protein found in bioluminescent jellyfish, was a monumental discovery, as it could be directly expressed with and attached to proteins in cells for labeling [Chalfie et al., 1994]. Derivatives of GFP have been developed to provide an array of colors, stability, and multimerization states [Rodriguez et al., 2017]. These tools for live-cell imaging allow us to dependably visualize the cytoskeleton in cells.

We currently have a suite of labels for actin visualization, each with its own benefits and drawbacks [Melak et al., 2017, Belin et al., 2014]. The gold standard for actin filament labeling is phalloidin, a toxin from the death cap mushroom. Phalloidin is a small molecule

that very specifically binds actin filaments, not monomers. Fluorophores of various colors are attached to phalloidin for fluorescence microscopy. The drawbacks to phalloidin labeling are that it stabilizes actin filaments, and cannot permeate the plasma membrane, therefore lending it not suitable for live-cell imaging, only fixed staining. Another common method is to express actin monomers in cells with a fluorescent protein (FP) attached. However, over-expression of FP-actin is unsuitable for cells, and this method can lead to high background signal from labeled monomers [Aizawa et al., 1997]. Another method for live-cell actin labeling is to use FP-tagged actin binding proteins, such as Lifeact, F-tractin and utrophin [Riedl et al., 2008, Brehm et al., 2004, Burkel et al., 2007]. Downsides to these labels are that they often bind certain actin structures more than others and can have side effects at high expression levels.

Lifeact, the most common of these labels, is a 17 amino-acid peptide derived from ABP140 in yeast [Riedl et al., 2008]. It is remarkably popular, having been used in around 7,000 studies, typically at unspecified concentrations. Though widespread in its use, negative side effects of Lifeact overexpression are widely reported and range from sterility in Drosophila, altered actin patch dynamics in yeast, and altered stem cell morphology [Spracklen et al., 2014, Courtemanche et al., 2016, Flores et al., 2019, Xu and Du, 2021]. Recently, the structure of the Lifeact-F-actin structure was solved, revealing that Lifeact binds at the D-loop on the actin filament [Kumari et al., 2020, Belyy et al., 2020]. This is the same location that cofilin, a disassembly protein, and myosin, a motor protein, bind. Thus, it is easy to imagine that constitutive Lifeact binding alters the disassembly of actin filaments and the movement of motor proteins.

Returning to the bird tracking example, our actin label Lifeact, alters the dynamics we wish to observe. In other words, our bird (actin) is affected by interacting with our tracking device (Lifeact). We aim to reduce the negative effects of Lifeact labeling by temporally controlling labelling using optogenetics.

1.3 Optogenetics

1.3.1 Overview of optogenetics

With actin as our metaphorical bird and Lifeact as our GPS tracker, we now need a magnetization system. For this, we turn to optogenetics. Optogenetics utilizes light-sensitive proteins found in nature. These proteins are involved in phototropism, the underlying mechanism for how plants and algae sense and grow towards the sunlight.

The field of optogenetics consists of two main branches: light-activated ion channels called opsins, and soluble, non-opsin photosensitive proteins that change conformation in response to light. Light-sensitive ion channels like channelrhodopsins (ChRs) and its relatives are ideal for spatiotemporal control of voltage-sensitive cells, as light-activation can be used to depolarize specific cells [Deisseroth, 2015, Paoletti et al., 2019]. This allows for the study of complex neuronal circuits in a non-invasive way in comparison to the use of probes for activation. This has revolutionized the field of neurobiology, allowing for the enhanced understanding of the complex relationships between neuronal activation and behavior. With this technology, we have advanced our understanding of the mechanisms behind processes such as learning, memory, and sensory processing, and also diseases like addiction and depression [Adamantidis et al., 2015, Adesnik and Abdeladim, 2021, Chen et al., 2022]. Channelrhodopsin optogenetics have also been used to study other polarizable cells such as cardiomyocytes, or heart muscle cells [Ambrosi et al., 2014, Abilez, 2012, Joshi et al., 2020]. Light-sensitive muscle tissue can be grown with ChRs, and has been integrated to create optogenetic robots. These robots come in a variety of shapes, from swimming fish to walking bots, and are controllable by direction and speed with light pulses [Lee et al., 2022, Ricotti et al., 2017, Park et al., 2016, Kim et al., 2023]. Though incredible, the field of ChR optogenetics can only actuate with electrochemical signaling. The other branch of non-opsin optogenetics utilizes a number of plant-derived photosensitive proteins to actuate a diverse

array of intracellular signals.

1.3.2 Non-opsin optogenetics

A number of non-opsin systems have been characterized and implemented as optogenetic tools (Figure 1.1) [Lu et al., 2020]. Most of these are dimerization or oligomerization systems that form upon blue light excitation. For example, a fungal receptor, VVD, homodimerizes in its wild-type form, allowing for precise control of protein protein interactions (PPIs). However, this interaction has a relatively low affinity, just 13 µM, and as a homodimer, one cannot bring two different proteins together [Zoltowski et al., 2007]. To extend the capabilities of VVD, a positively charged version (pMag) and negatively charged version (nMag) were developed as a way to force heterodimerization instead of homodimerization [Kawano et al., 2015]. They refer to this set of proteins as the magnet system, and developed a number of variants to improve switching and kinetics.

Cryptochrome 2 (CRY2) is another photosensitive protein used in optogenetics. The first CRY2-based tool is the CRY2-CIB1 heterodimerization system. Upon illumination, these two units bind, and recovery times are rather slow at 16 minutes [Liu et al., 2008]. For systems in which minimizing the number of blue light pulses is ideal, this can be beneficial. However, the wild type CRY2-CIB1 system had limitations including low expression and unwanted nuclear localization, which was resolved through rational mutation of the sequence [Taslimi et al., 2016]. CRY2-CIB1 has been used to control gene-expression, cell signaling, cell death, movement and more [Duan et al., 2017]. In addition to forming heterodimers with CIB1, CRY2 forms homo-oligomers upon photoactivation. These clusters can be large enough to be visualized with microscopy, but require high concentrations, and the oligomerization tendency of the attached proteins plays a role as well [Park et al., 2017]. Mutants with increased propensity to cluster such as CRY2olig CRY2clust were developed to solve this problem [Park et al., 2017, Taslimi et al., 2016]. CRY2olig was used to cluster myosin motor

heads together to create a functional motor upon photo-excitation. This induced filopodia formation in a light-dependent manner, allowing for the investigation into the role of filopodia in axolotl limb regeneration [Zhang et al., 2021]. The multi-modal abilities of CRY2 can be useful, but it is important to consider that when using the CRY2-CIB1 system, there is homo-oligomerization occurring upon photo-excitation as well. Also, the recovery time is much longer than that of other optogenetic tools, which can be either a pro or a con depending on the use. In Drosophila embryonic development, slow recovery of CRY2-CIB1 is ideal, and short pulses lead to long-term furrow formation in response to light [Izquierdo et al., 2018]. Overall, CRY2 is an optogenetic tool with a number of variants and multimerization modes, lending itself to broad applications.

1.3.3 AsLOV2 dynamics and chemistry

AsLOV2 (LOV2) is the second light-oxygen-voltage (LOV) domain from oat phototropinI [Sakai et al., 2001, Kennis et al., 2004]. This protein has been highly studied and characterized, lending itself remarkably useful as a base for optogenetic tool development. AsLOV2 contains two main structural elements, its PAS core, containing beta sheets that bind to the flavin chromophore at the center, and the A'α and Jα helices, which dynamically and reversibly unfold in response to blue light.[Crosson and Moffat, 2002, 2001, Harper et al., 2003, Zayner et al., 2019] The N-terminal A'α helix is 7 amino acids long, and the C-terminal Jα helix is 24 amino acids long. When the flavin mononucleotide (FMN) chromophore is photo-excited, it forms an adduct with cysteine 450 of the core, causing a conformational change that induces unfolding of the A'α and Jα helices [Christie et al., 1999, Halavaty and Moffat, 2007]. Then, after the chromophore is quenched, the helices refold. The timing of this refolding is 80 second in vitro with wild-type protein, but can vary from tens of seconds to multiple minutes by varying buffer conditions and with mutations in LOV2 [Zoltowski et al., 2009, Zayner and Sosnick, 2014, Zayner et al., 2013]. For example, the Q513D muta-

tion reduces the recovery time to 5 seconds, while the Q513L mutation lengthens recovery time to 1793 seconds [Zayner and Sosnick, 2014]. Recovery time is also sensitive to pH and reduces greatly with the addition of imidazole [Zayner and Sosnick, 2014]. This tunability is useful in optogenetic systems where specific kinetics are required.

1.3.4 Optogenetic dimerization systems using AsLOV2

A number of optogenetic tools have been developed using LOV2. The Zdk protein was developed as a binding partner to LOV2 in its folded, dark state, but does not bind the light-activated, unfolded state [Wang et al., 2016]. Zdk-LOV2 is used as a light-sensitive dimerization system where two proteins can be chimerically attached to Zdk and LOV2 respectively. The proteins will remain in close proximity in the dark, but upon activation, they will separate with the release of Zdk and LOV2.

Conversely, a number of protein dimerization systems have been designed such that LOV2 does not bind its target in the dark, but has high affinity for the target in the light. This is achieved by incorporating helical peptides or proteins into the Jα helix of LOV2 such that the peptide is caged by the core of LOV2 and cannot bind its target in the dark. Upon photoexcitation, the Jα helix unfolds and becomes flexible, allowing for the peptide to bind its target (Figure 1.1). One of these LOV2-based dimerization systems is TULIPs, which cages the PDZ-binding peptide "pep" in the dark, but is active after blue light illumination [Strickland et al., 2012].

Another common LOV2-based dimerization system is iLID [Lungu et al., 2012, Guntas et al., 2015]. ILID incorporates the SsrA peptide into the Jα helix, with SspB as the target protein [Lungu et al., 2012]. Multiple variations of iLID were developed with varying binding affinities in the light vs dark, but retain similar dynamic ranges [Guntas et al., 2015]. For example, iLID nano has very weak binding affinity in the dark, but also relatively low binding in the light, while iLID milli has much higher lit-state binding, but also has higher dark-

state binding. Depending on the use case and the system, different variations of iLID can be ideal. For a system where dark-state activity is highly unwanted, the iLID nano system is more appealing, whereas for a system in which high activity is needed in the light, the iLID milli system is an ideal candidate. One popular implementation of LOV2-dimerization systems is local recruitment of guanine exchange factors (GEFs) to induce contractions in adherent cells [Wagner and Glotzer, 2016, Varadarajan et al., 2022, Cavanaugh et al., 2020]. Recruitment of GEFs to the membrane increases their local concentration, resulting in signal cascades leading to cell contraction.

LOV2-based dimerization systems are ideal as they are well-characterized and tunable. They are "plug and play" systems that do not require detailed characterization to obtain a functional system. The modularity and versatility of these tools allows for users to simply add these domains to the protein pair that they would like to control and are off to the races.

1.3.5 Other AsLOV2-based optogenetic systems

In addition to dimerization systems, there is a suite of LOV2-based optogenetic tools resulting from the incorporation of peptides of interest into the Jα helix. Examples include: photo-activatable myosin cargo binding peptides (LOVDab), nuclear localization signals (LEXY/LINUS), and calcium/potassium channel effectors (BACCS/BLINK) [French et al., 2017, Niopek et al., 2014, Ishii et al., 2015]. Unlike the dimerization systems, each of these requires trial and error to ensure the joining between the LOV2 domain and the peptide leads to maximal dynamic range between light and dark state activities. However, it allows for modulation of systems that would not otherwise be able to be controlled with spatiotemporal resolution. We took this approach with Lifeact, as we wanted to control the specific activity of a small peptide.

A variety of other highly creative tools have been developed using LOV2. MyLOV builds a gear-shifting myosin motor from the ground up with a wild-type catalytic head domain,

spectrin repeats as rigid arms, and LOV2 as a light-sensitive hinge [Nakamura et al., 2014, Chen et al., 2012]. Light changes the step length of this motor, leading to differences in motor activity and direction. Z-lock harnesses the LOV2-Zdk interaction as a clamp with a protein of interest in between the two [Stone et al., 2019]. The LOV2-Zdk interaction blocks the catalytic domain in the dark, caging the protein of interest, but upon excitation, the catalytic domain becomes exposed and active. Circularly permutated LOV2 (cpLOV2) alters the location of the N and C termini such that the C-terminus of peptides can be integrated into the Jα helix, rather than the N-terminus [Kumar et al., 2013, He et al., 2021]. Each of these approaches utilizes the conformational change of LOV2 in a distinct manner to alter protein activity.

The breadth of LOV2-based optogenetic tools highlights the utility of such spatiotemporal control of proteins. With a base of knowledge and previous work to inspire us, we built LILAC (Light-Induced Localization to ACtin). In the following chapters, I describe the design, validation, and implementation of LILAC, first as an imaging tool, and second, as a patterning tool.

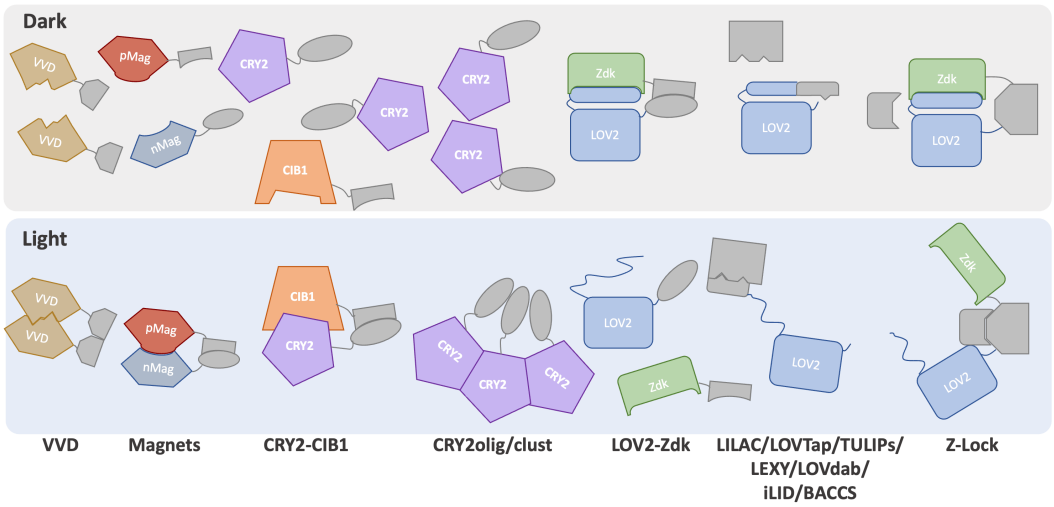

Figure 1.1: Schematic of non-opsin optogenetics.

CHAPTER 2

DESIGN AND VALIDATION OF LILAC

2.1 Design based on structure/residue assessment

Avena Sativa LOV2 (AsLOV2 or LOV2) is the second LOV (light-oxygen-voltage) domain of photosenstive protein found in oat [Sakai et al., 2001, Kennis et al., 2004]. The LOV domain is part of the Per-Arnt-Sim (PAS) protein fold family, and binds to a chromophore, flavin mononucleotide (FMN) [Christie et al., 1999, Halavaty and Moffat, 2007]. Upon blue light excitation, the FMN forms an adduct with cysteine 450, causing a conformational change core which leads to unfolding of the N-terminal A'α and C-terminal Jα helices (Figure 2.1) [Crosson and Moffat, 2002, 2001]. This conformational change of AsLOV2 has been utilized to create a number of optogenetic tools. In general, an optogenetic tool is a protein that is able to be turned on/off using light. A popular set of LOV2-based optogenetics utilizes LOV2 to create light-sensitive dimers [Strickland et al., 2012, Lungu et al., 2012, Guntas et al., 2015, Wang et al., 2016]. A second sector of LOV2-based optogenetics harnesses the conformational changes of LOV2 with light to disrupt the activity of a protein of interest (POI) [He et al., 2021, Stone et al., 2019]. By inserting LOV2 into the loops of the POI, one can disrupt the structure when the Jα helix of LOV2 unfolds.

Another convenient method of creating optogenetic tools is with helical peptides Strickland et al. [2012], Lu et al. [2020], French et al. [2017], Niopek et al. [2014], Ishii et al. [2015]. Because the Jα helix of LOV2 is dynamic in response to light, it is intuitive to add other helical peptides at the end of the Jα helix (Figure 2.1). The Jα helix has two surfaces, visualized easily with a helical wheel representation (Figure 2.2a) [noa, 2022]. Shown as the top half in the figure, one side, which faces solution, has more polar and charged groups. The other side, with hydrophobic residues, contacts LOV2's core. For a successful design, it is important to not disrupt the hydrophobic residues, as they are critical for refolding of

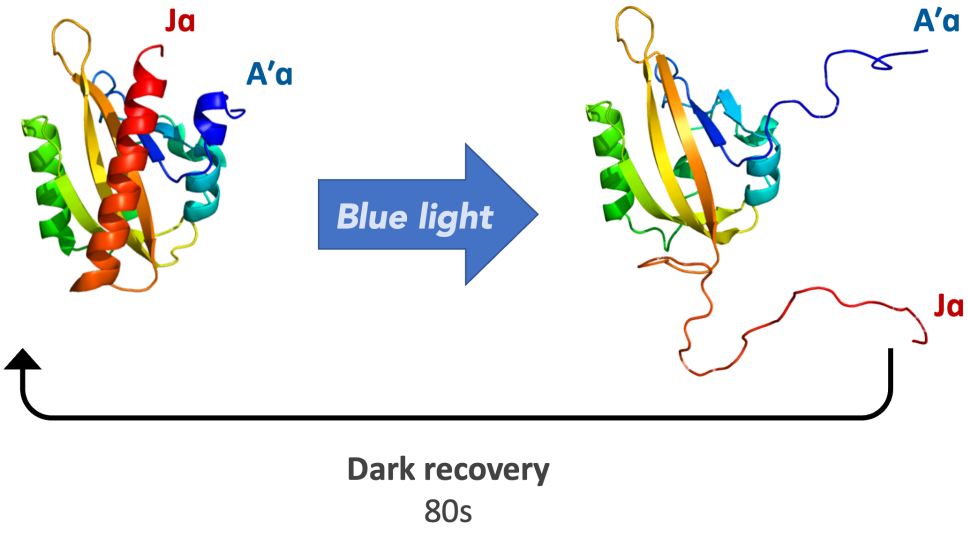

Figure 2.1: Structure of the AsLOV2 helix in the dark and lit states. In the dark, the Ja and A'a helices and folded (shown in red and blue). Upon excitation with blue light, these helices unfold reversibly, as modeled here. The recovery time of wild type AsLOV2 is 80 seconds in vitro. Adapted from PDB 2V1A.

the Jα helix and caging of the peptide. This is exemplified by the I539E mutation, which mutates a hydrophobic residue on the hydrophobic face of the Jα helix (shown in Figure 2.2a) to a charged glutamic acid, resulting in the Jα helix remaining unfolded, in a constant lit-mimetic state.

Here, we designed LILAC(Light-induced localization to actin), an optogenetic version of Lifeact, an actin binding peptide [Riedl et al., 2008]. The actin cytoskeleton is critical for myriad cellular processes, including cell transport, division, movement, and more [Blanchoin et al., 2014]. Therefore, visualization of the cytoskeleton with microscopy is important for the field of cellular biology. Lifeact, an actin label for live-cell microscopy, has concentration-dependent negative side effects on cells despite its widespread use [Spracklen et al., 2014, Courtemanche et al., 2016, Flores et al., 2019, Xu and Du, 2021]. By reducing Lifeact's affinity for the cytoskeleton in the dark, we aimed to reduce these negative effects. Also, the ability to switch Lifeact on and off with optogenetics allows for new image processing

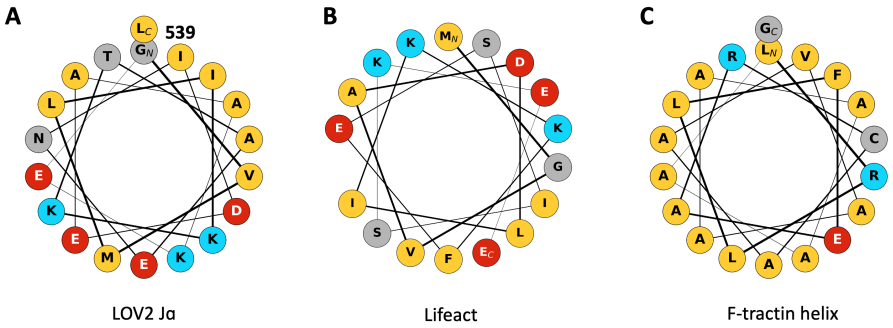

Figure 2.2: Helical wheel representation of the LOV2 Jα helix. (a), Lifeact (b), and the predicted F-tractin helix (c). Nonpolar residues are yellow,, polar uncharged residues are grey, polar positively charged residues are red, and polar negatively charged residues are blue. Made using `https://cpt.tamu.edu/galaxy-pub`.

methods for enhanced actin imaging.

When designing a new optogenetic tool, the first consideration should be the structure of the protein of interest. Now, with the availability of structure prediction models such as Alphafold, a quick prediction can be obtained on the protein of interest [Tunyasuvunakool et al., 2021, noa, 2023]. If the sequence is a small peptide, the prediction might result in a helical structure, an ideal candidate for incorporation into the Jα helix. This can also be predicted with helicity-predicting software such as Agadir [Müller et al., 2017]. In our example, Lifeact is a small, 17 amino acid, helical peptide, perfect for incorporation into the Jα helix. By incorporating Lifeact into the C-terminal Jα helix, it is caged, and unable to bind actin in the dark (Figure 2.3a). For the example of F-tractin, another actin-binding sequence, the N-terminus of the Alphafold-generated model is unfolded with a helical C-terminus(Figure 2.4) [Brehm et al., 2004]. The lack of helical structure at the N-terminus would likely not work for a canonical addition of the peptide to the C-terminus of the Jα

helix. However, recent work has shown success of a circularly permutated LOV2 variant, cpLOV2, in which the N and C-terminus of wild type LOV2 are fused, and a new N-terminus is created at the beginning of the Jα helix [Kumar et al., 2013, He et al., 2021]. Therefore, the Jα helix is now at the N-terminus, instead of the C-terminus of the protein. This allows for optogenetic control of peptides like F-tractin, with structured C-terminal helices. In this design, the N-terminus of F-tractin would be unstructured at the N-terminus of the protein, and the C-terminus of F-tractin would integrate into the Jα helix. It should be noted that if the unstructured N-terminus is sufficient to bind actin, this design would likely not cage F-tractin in the dark.

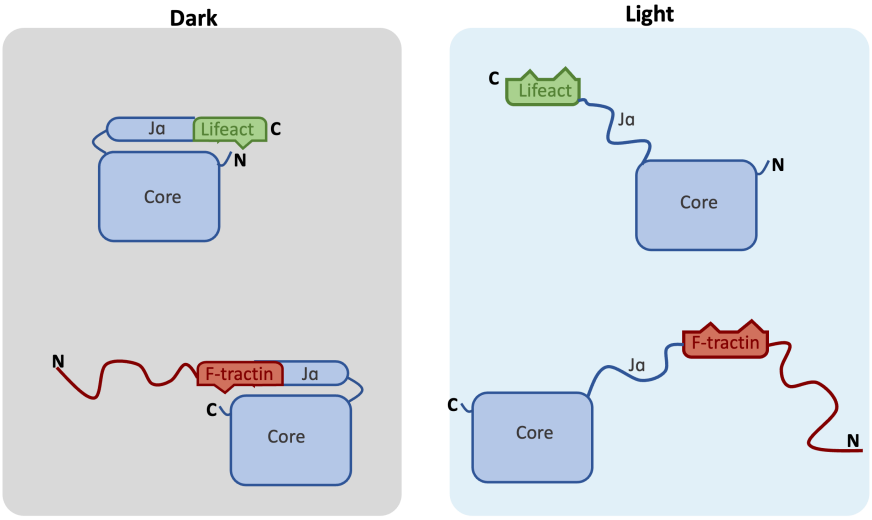

Figure 2.3: Schematic of LOV2-based optogenetics for Lifeact and F-tractin. Schematic demonstrating the need for a circularly permutated LOV2 to cage F-tractin. Wild type LOV2 can cage Lifeact with it's C-terminal Jα helix. However, due to the unstructured N-terminus of F-tractin, it must be joined to cpLOV2, which is reconfigured to have the Jα helix at the N-terminus.

When deciding at which exact residues to combine the Jα helix and the peptide of interest, creating a peptide wheel can be helpful. Helical wheels can allow for easy visualization of amphipathic helices, where one face of the helix is hydrophobic and the other is hydrophilic. If this is the case, the hydrophilic and hydrophobic faces of the peptide of interest can be

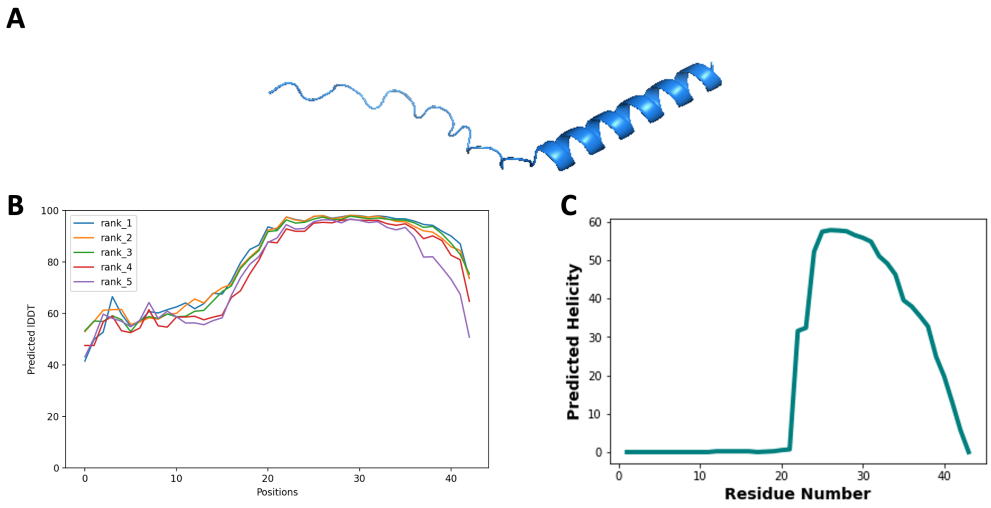

Figure 2.4: Predicted structure of F-tractin. (a) Alphafold-predicted structure of F-tractin, an actin binding peptide. (b) Predicted lDDT (a confidence metric) for the Alphafold-predicted structures. (c) Predicted helicity of each residue of F-tractin. Structure prediction from Alphafold (`https://github.com/deepmind/alphafold`) and Agadir (`http://agadir.crg.es/`).

aligned with the corresponding faces on the Jα helix for better chances of being refolded in the dark. Not only does this have the benefit of not disrupting the hydrophobic interaction between the Jα and core of LOV2, but it also places the hydrophobic face, which likely is the binding interface, towards the core of LOV2, occluding the POI from its binding partner. For Lifeact, there are two distinct faces, allowing for relatively easy integration into the Jα helix (Figure 2.2b). The F-tractin helix is highly non-polar, meaning nearly any way it is integrated with the Jα helix, it should not significantly disrupt the non-polar interactions between the helix and the core (Figure 2.2c).

With this in mind, a suite of possible designs can be created with different conjugation points between the Jα helix and POI. To find the design with the highest dynamic range, at least a few of these designs should be expressed and tested. If the POI is inserted too far into the Jα helix, the helix will not be able to refold, resulting in strong dark-state binding. Contrarily, if the POI is not inserted far enough into the Jα helix, it will dangle away from

LOV2 and always be able to bind, also resulting in dark-state binding. To test our design, we examined binding of LILAC to actin structures in live cells using TIRF (total internal fluorescence microscopy) and actin cosedimentation.

2.2 Assay development and fluorescent protein selection

When working with light-sensitive proteins, the selection of fluorescent proteins (FPs) is crucial for visualization of both the optogenetic tool and any other proteins that need to be visualized simultaneously [Rodriguez et al., 2017]. LOV2 is excited by blue light, complicating the use FPs that are either blue or excited by blue light, such as GFP and CFP [Chalfie et al., 1994]. The easiest option is to use red-shifted colors, such as red FPs like mCherry or near-infrared FPs like mIFP663 [Shaner et al., 2004, Liu et al., 2022]. By using red-shifted labels, one can be sure that the excitation and emission spectra of the FPs would not excite LOV2, allowing for visualization of these FPs while LOV2 is in its dark-state.

On the other hand, blue-shifted FPs including GFP and CFP can be used in conjunction with LOV2-based tools, if they are used strategically. For example, if only the photo-excited image is necessary, GFP can be directly attached to the LOV2-based protein and both can be excited simultaneously. Alternatively, if an RFP is attached to LOV2, it can be visualized first, in the dark. Then, a second GFP-tagged protein can be imaged, simultaneously exciting LOV2. Then the RFP-LOV2 can be imaged again, this time in the excited state from the blue light used to excite GFP. To ensure that LOV2 is excited, both the RFP and LOV2 can be excited with green and blue lasers. Therefore, the recovery dynamics between the GFP image and excited LOV2 image are not of concern.

2.3 S2 cell maintenance and information

Drosophila melanogaster Schneider 2, or S2 cells are a common insect cell line derived from early stage fly embryos. We chose to use S2 cells for a number of reasons: they are popular, have a characteristic and prominent actin ring after spreading, and are simple to transfect and maintain.

Our maintenance protocol is based on Bunch et al. [1988].

2.3.1 Materials

- T25 or T75 tissue culture flasks
- Schneider's insect media
- Insect media supplement
- Penicillin/Streptomycin for cell culture
- Kimwipes
- 70% ethanol
- Autoclaved 1.5 mL microcentrifuge tubes

2.3.2 Equipment

- Hemocytometer
- Phase contrast microscope
- Tissue culture hood

2.3.3 S2 cell maintenance

S2 cells must be handled in a tissue culture hood and divide in Schneider's insect media supplemented with 10% fetal bovine serum (FBS) or 10% insect media supplement. Because media supplement is more consistent and cheaper, this is often preferred, but notably, cells are often shipped/frozen in FBS and must slowly be weaned to media supplement. To reduce contamination, antibiotics such as penicillin (50 units/mL) and streptomycin (50 /textmu g/mL) are often also added. S2 cells are conveniently stored in the dark at room temperature without CO_2 and can either be shaken in suspension flasks or grown in a monolayer in tissue culture flasks, as they are semi-adherent. Cells can be stored up to 28°C for faster growth.

At around 5*10^6 cells/mL, cells are confluent and typically float and form clumps, which does not have negative effects on the cells. When working with S2 cells, pipette up and down, ensuring that cells are dislodged from the surface while pipetting. The bottom of the flask will look clearer where cells have been dislodged, and the clumps will be broken up. Cells can begin to reattach within minutes, so make sure to resuspend them each time they are pipetted.

Cells are counted using a hemocytometer. Begin by resuspending the cells. Then dilute the cells 1:10 by adding 100 µL of cells to n microcentrifuge tube with 900 µL of media. Remove the tube from the tissue culture hood; then, mount 10 µL of the dilution to a hemocytometer. Count the number of cells in one section of the hemocytometer under the microscope. Normally, this number is multiplied by 104 to get the density of cells/mL. However, we have diluted the cells 1:10, so multiply by 105. For example, if 150 cells are counted, the density is 15*10^6 cells/mL.

Cells double every 24-36 hours. Split them to 2-4*10^6 cells/mL every 3-6 days by adding a small amount of cells to a new flask with fresh media. They should never be split below 0.5*10textsuperscript6 cells/mL and should not grow to higher than 15-20*10^6 cells/mL.

2.4 S2 cell transfection

Transfection is the process of inserting foreign DNA into eukaryotic cells. It allows for the expression of labeled proteins, proteins from other cell types, and for expression level control. There are a variety of transfection methods including physical methods like electroporation and microinjection, as well as chemical methods such as calcium phosphate precipitation and lipofection. Lipofection using cationic lipids such as DDAB is advantageous because it results in high transfection efficiency and low cell toxicity. Here, we describe transfection of mCherry-LILAC in the pMT vector, which contains the metallothionein promoter from Drosophila. This allows for the concentration-dependent induction of expression with the addition of copper to the cell media with precise timing. Of note, each cell will uptake a differing plasmid copy number. This causes cell-to-cell variation in expression level given a constant copper sulfate concentration, allowing for analysis of concentration-dependent effects within a single transfection.

Our transfection protocol is based on the protocol developed in Han [1996].

2.4.1 Materials

- Didodecyldimethylammonium bromide
- Plasmid DNA for LILAC expression in insect cells
- 100 mL beaker
- 50 mL conical tube
- Vacuum filter/storage system
- 1.5 mL microcentrifuge tubes
- 0.5 M $CuSO_4$

- Schneider's insect media
- Insect media supplement

2.4.2 Equipment

- Sonicator
- Hemocytometer
- Phase contrast microscope
- Tissue culture hood

2.4.3 Transfection protocol

Make DDAB solution. Begin by making the didodecyldimethylammonium bromide (DDAB) solution at 250 /textmu g/mL in water. DDAB is difficult to solubilize into water. This can be solved by heating up the solution at 60°C until it is no longer cloudy. Then, sonicate for at least 30 minutes to ensure it is in solution. Filter to sterilize using a 0.4 micron filter.

Make DDAB:media mixture. Transfections should be done 2-4 days after cells are split while they are quickly dividing. Begin by mixing the media and the DDAB mixture 2:1. For example, if using a 6 well plate for transfection, each well will need 145 µL of the mixture. Make 7 reactions to have extra just in case. That means 7*145=1015 µL total. Therefore, 677 µL media should be combined with 338 µL of DDAB. Let this sit for five minutes.

Count cells. While waiting for the media:DDAB mixture, count the cells.

Add DNA. For a 6-well plate, add 100-500ug of DNA to a labeled 1.7 mL tube for each well. The amount of DNA needed can vary. It is useful to test a variety of DNA

concentrations to find the optimum conditions. Gently add 145 µL of the media:DDAB mixture to each tube. Let that sit for 15 minutes.

Prepare wells. For transfection, cells should be at $1.35*10^6$ cells/mL. While the DNA and media:DDAB mixture sit, calculate the volumes of cells and media needed to dilute to $1.35*10^6$ cells/mL. For example, if using all 6 2mL wells, make 14 mLs of cells at the desired concentration. If the cells are at $5.4*10^6$ cells/mL, add 3.5 mLs of cells and 10.5 mLs of media to a 15 mL tube. Then add 2mLs of the diluted cells to each well. While waiting for the rest of the 15 minutes, label wells and clean up the work space.

Add transfection reagents to cells. Add 145 µL of DNA and media:DDAB mixture to each cell drop wise and slowly while gently shaking the 6-well plate in a circular motion. Store cells in a dark area, such as a clean styrofoam box.

Induce expression. If using the pMT promoter, the next day, add between 0.5-2 µL of 0.5M $CuSO_4$. The copper will induce the cells to express the protein of interest, and the more copper is added, the more they will express on average. Test various concentrations to find the optimal conditions. Give the cells at least 12 hours to express protein before imaging, especially if using a fluorescent protein, which takes time to fold. If the cells express high concentrations of exogenous proteins for an extended period of time, they often begin to localize the exogenous protein to lysosomes. This can be seen by imaging the cells with fluorescence microscopy.

2.5 TIRF Microscopy

To test designs and mutations of LILAC, we imaged S2 cells expressing either mCherry-tagged LILAC or Lifeact. Fluorescence microscopy allows for the visualization of specifically labelled molecules. There are a number of different fluorescence microscopy methods, most of which illuminate a large volume of the sample. This has two disadvantages: increased photobleaching of the sample, and the illumination of the sample outside of the focal plane

resulting in increased background photons. To avoid this, we image with total internal reflection fluorescence microscopy (TIRFM). With TIRFM, the illumination is on an angle such that it induces total internal reflection, and an evanescent wave is created. This illuminates just a thin layer of the sample at the surface of the glass. This is particularly useful for imaging S2 cells, as the main actin structure, the lamellipodia, is thin and on the surface of the glass. It is also highly favorable for single-molecule imaging of actin filaments in vitro, as filaments are specifically visualized as they come into contact with the glass surface. Here, we image LILAC by exciting either just the mCherry tag (dark) or by exciting the mCherry and LOV2 (light). This allows us to see if there is a difference in actin labeling in the dark versus the light.

Our imaging protocol is based on the protocol described in Buster et al. [2010].

2.5.1 Materials

- Concanavalin A
- 35mm glass bottom dishes

2.5.2 Equipment

- TIRF microscope with mCherry/GFP channels

2.6 Live TIRFM protocol

Prepare dishes for imaging. S2 cells spread on concanavalin A (ConA) coated glass. To prepare dishes for imaging, solubilize ConA at 0.5 mg/mL. Depending on the area of the glass in the dish, add 15-50 µL of ConA to the glass in the dish in the tissue culture hood. Spread the solution gently using the pipette tip, and leave the dishes in the hood for 15-20

minutes until the water evaporates. Put the dishes in a sterile container and store them for later use.

Seed cells for imaging. 12-24 hours post-induction, harvest cells for imaging. Use the pipette to dislodge cells and add 100-300 µL of cells to the ConA-coated glass-bottom dish. Cells take around 30 minutes to spread. To see filopodia in landing cells, image cells immediately to watch them spread.

Prepare the microscope. Make sure the microscope has the appropriate channels for imaging LILAC. Most importantly, a normal mCherry channel (green excitation, red emission filter) is necessary. It is also necessary to excite LILAC. Ideally, simultaneous excitation of mCherry/LILAC with green and blue can be achieved, while observing with the red emission filter. If this is not an option, the green fluorescent protein (GFP) channel (blue excitation, green emission), can be used to excite LILAC, but not visualize it. followed imediately but visualization with the mCherry channel.

Place cells on the TIRF microscope. Because S2 cells grow at room temperature, stage heating and CO_2 is not needed for live imaging. When finding focus, use the mCherry channel, so that it is not necessary to wait 2 minutes for LILAC to return to the dark state for a pre-excitation image. Try to focus on the glass surface, as the actin-rich filopodia and lamellipodia will be found there.

Image cells. After finding a cell, image the cell with the mCherry signal. This gives the pre-excitation image of LILAC in the cell body. Next, excite LILAC with either the GFP channel or the mCherry/LILAC channel. LILAC recruits to actin structures in under one second, and in normal media, recovers to the dark state with a time constant of about one minute. Next, image again with the mCherry channel within a few seconds, giving enough time for LILAC to go to actin structures, but imaging soon enough such that it is still bound. If desired, continue imaging with the mCherry signal for 2 minutes until LILAC recovers to the dark state. LILAC can also be continually excited to continual imaging of actin.

2.7 Protein purification

Expression and purification of proteins is vital to understand the biochemical properties and function of proteins, as well as understanding protein interactions. In this case, purification of LILAC allows for the later determination of the binding affinity between LILAC and actin filaments in the light and dark states. Structural properties of purified LILAC can also be studied using biophysical methods such as circular dichroism, a method for measuring the secondary structure of proteins. There are many protein expression systems, but the simplest is E. coli, as it does not require a biosafety hood. A number of tags can be used to purify proteins, but the most common is the addition of 6 histidine residues, which bind to nickel columns. This expression protocol takes 5 days, but protein can be stored at -80 C.

2.7.1 Materials

- E. coli for protein expression (such as BL21)
- Plasmid DNA for 6xHis-tagged LILAC expression in E. coli
- SOC medium
- LB agar plates with antibiotics
- Autoclaved LB media
- Spectrophotometer cuvettes
- Lysis buffer (50 mM Tris pH8.0, 100 mM NaCl, 5 mM Imidazole)
- Wash buffer (50 mM Tris pH8.0, 100 mM NaCl, 20 mM Imidazole)
- Elution buffer (50 mM Tris pH8.0, 100 mM NaCl, 200 mM Imidazole)
- Dialysis buffer

- Dialysis tubing
- 1.5 mL microcentrifuge tubes
- 50 mL conical tubes

2.7.2 Equipment

- Heated water bath
- Spectrophotometer
- Shaking incubator
- Sonicator
- Centrifuge
- Nickel column
- Stir plate
- Dialysis tubing clips
- Stir bar
- Ice bucket

2.7.3 Purification Protocol

Transform E. coli with LILAC plasmid. Defrost competent E. coli on ice. Add 10-20 ng of DNA to the cells, then wait 5 minutes. Add cells to the heated water bath at 43°C for 45 seconds. Immediately remove cells and place them on ice for at least two minutes. Add 100-300 µL of SOC medium to cells. Shake cells at 250 rpm at 37°C for 30 minutes. Plate

50-100 µL of cells onto the agar plate with antibiotics according to the chosen expression plasmid. Leave in an incubator at 37°C overnight.

Inoculate 5 mL culture. Add antibiotic according to the chosen expression plasmid to 5 mL of autoclaved LB, making sure to flame the LB tube. Gently touch either a pipette tip or inoculating loop to a single colony, flame the LB tube,and briefly swirl the tip or loop in the media to release the colony. Shake overnight at 37°C and 250 rpm.

Inoculate larger culture (1L). Add antibiotic according to the chosen expression plasmid to 1 L of autoclaved LB. Take 1 mL of sample and add to a cuvette as a blank sample. Inoculate 1 L culture with the 5 mL culture. Shake at 37°C and 250 rpm until the OD at 600 nm is 0.6.

Harvest cells. Spin cells at 4,000 xg for 15 minutes to pellet the cells. Pour of the media supernatant. The pellet can be aliquoted into 0.5-1 g aliquots and stored at -80°C indefinitely.

Lysis. From this step forward, try to reduce the light exposure of LILAC as much as possible by covering tubes with foil or using black tubes . Resuspend the cell pellet in 45 mL of lysis buffer. Sonicate cells on ice in a cold room in the dark. Sonication settings depend on instrumentation, however, it is always important to ensure that the sample does not overheat. Additionally, it is important to ensure that the sonicator tip does not contact the tube wall. This can happen when the sample heats up, melts the ice around it, and moves. To prevent this, check on the sample every 20 minutes and adjust its position. Take 50 µL of sample post lysis for gel analysis.

Remove cell debris. Spin cells at 15,000 xg for 40 minutes to pellet cell debris. Take 50 µL of the supernatant for gel analysis.

Purify LILAC using nickel affinity. A large benefit to using an FP-tagged protein is the ease of protein purification. With an FP, the protein is visible by eye, such that it can be seen when the protein binds to the column and elutes off, and the relative concentration

can be visualized. To reduce light exposure, cover the column with aluminum foil and store LILAC in black tubes. When using the nickel column, make sure to always have at least one mL of solution above the column. If it dries out, it can form bubbles, damage the column, and disrupt the protein as it flows through the column. If the nickel column is stored in ethanol, let the ethanol flow through, then equilibrate with water. Prepare the nickel column by flowing at least 5 column volumes of the lysis buffer. Next, flow the supernatant with 6xHis-tagged LILAC over the column, to allow the protein to bind the column. Save the flow through and take 50 µL of the flow through for gel analysis. Flow 10x column volume of wash buffer to remove binding of other proteins to the column. Save the wash flow through and take 50 µL of it for gel analysis. Flow 3x column volume of elution buffer to remove the LILAC from the column. Collect the flow through in 1-2 mL fractions. If using an FP, the fractions with protein will be visibly fluorescent, and the higher concentrations even more so. Determine the concentration of the fractions using a nanodrop, and pool them as necessary.

Dialyze LILAC into the assay buffer. Make a large volume (1-2L) of the dialysis buffer for the next experiment. Be cognizant of how much imidazole is in the buffer, as it changes the recovery time of LOV2 . It is easiest to make a 10X stock and dilute imediately before each dialysis. Cut about 6 inches of dialysis tubing. Rehydrate the tubing in the dialysis buffer for two minutes. Fold over 0.5 inches of the tubing and clamp it with a dialysis tubing clip. Pinch the tubing and wiggle back and forth to open it. Add the protein inside the tubing and fold over and clip the other side. Add the tubing to the dialysis buffer and let it stir slowly, overnight in a cold room. Cover in foil to ensure minimal exposure.

2.8 Actin cosedimentation

When polymerized into filaments, F-actin sediments at 100,000 xg in an ultracentrifuge. This can be used to determine the binding affinity between actin filaments (F-actin) and other proteins, as bound proteins will be pulled into the pellet with the actin filaments.

By titrating the protein of interest (POI) and measuring the cosedimentation with actin, the binding affinity can be determined through fitting with a hyperbolic curve. Here, we detail the protocol for determining the binding affinity of mCherry-Lifeact or mCherry-LILACI539E, a lit-mimetic mutant, with F-actin, derived from Heier et al. [2017]. The lit-mimetic mutant was chosen due to the challenging nature of illuminating protein in an ultracentrifuge. A schematic of the protocol is shown in Figure 2.5.

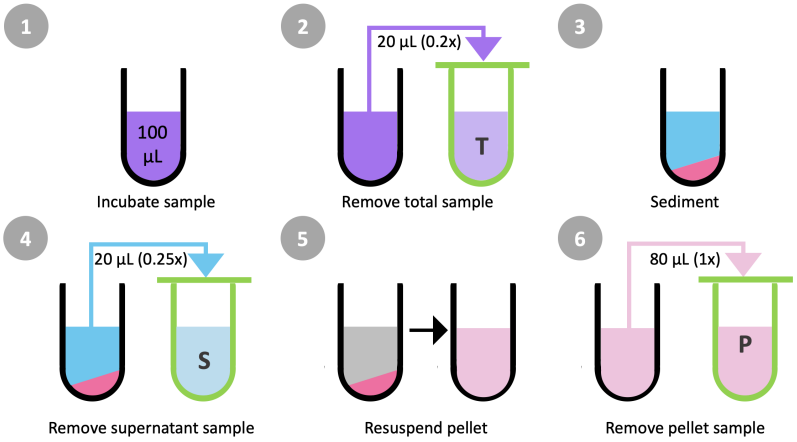

Figure 2.5: Schematic of measuring affinity by cosedimentation. First, samples are incubated. Then, a total sample is removed for analysis. Next, the sample is sedimented, and the supernatent is removed for analysis. Finally, the pellet is resuspended and placed into a new tube for analysis. Green tubes indicate samples to be used for gel electrophoresis. The black tube is an ultracentrifuge-safe tube for sedimentation.

2.8.1 Materials

- Purified actin monomers
- 10x G-buffer 20mM Tris-Base, 2mM $CaCl_2$, 0.1% Azide
- 50x Polymerization salts 2.5 M KCl, 0.1 M $MgCl_2$

- 50x ATP 0,1M
- 0.1 M DTT
- Assay buffer 25 mM KCl, 25 mM imidazole, pH 7.5, 1 mM K-EGTA, 4 mM $MgCl_2$, 1 mM DTT
- Ultracentrifuge tubes
- 1.5 mL microcentrifuge tubes
- Loading buffer

2.8.2 Equipment

- Ultracentrifuge
- Gel electrophoresis tank

2.8.3 Actin cosedimentation protocol

Polymerize actin filaments. Calculate the necessary volume of actin monomers to add to reach a final concentration of 10 uM. For example, if the G-actin stock is 20 uM, to make 100 µL of F-actin, add 50 µL of G-actin stock. Next, add 10 µL 10x G-buffer and 2 µL 0.1M DTT and 34 µL of water. After these have been mixed, add 2 µL 50x ATP and 2 µL of 50x polymerization salts. For quick filaments, let sit at room temperature for at least an hour. For longer filaments, leave at 4°C overnight. To stabilize filaments, add phalloidin to reach a 1:1 monomer to phalloidin ratio. In some cases, phalloidin can compete for binding with other molecules, but it has previously been shown to not compete with Lifeact.

Prepare LA or LILAC-lit. First pre-spin the POI at 50,000xg for at least 10 minutes in an ultracentrifuge tube to remove any aggregates. Transfer to a microcentrifuge tube,

ensuring that any aggregate on the bottom of the tube is not aspirated, and measure the concentration of the protein.

Incubate LA or LILAC-lit with F-actin. Choose the concentration to hold actin at as the POI is titrated. It is important that the actin be well under the approximate binding affinity. In this case, the binding between Lifeact and F-actin has been reported between 2-14 uM, so we will use an actin concentration of 0.5 uM. Binding affinities depend on buffer conditions such as pH and salt, so be sure to keep this in mind. Also, be aware that F-actin begins to depolymerize at low concentrations. Create two sets of samples in ultracentrifuge tubes, half that will incubate with actin and half that do not, to ensure that sedimentation of the POI is due to binding and cosedimentation with actin, not from aggregation. The samples without actin will be the background sedimentation samples. Calculate the volume of POI that must be added for each desired concentration, and the volume of assay buffer to bring the sample to a desired final volume. For example, to create a 100 µL centrifuge sample with a Lifeact final concentration of 1 uM, add 5 µL of 10 uM F-actin, 1 µL of 100 uM Lifeact, and 94 µL of assay buffer. Remove 1/5 of each centrifuge sample (20 uL) and mix with 20 µL of 4x loading buffer and 20 µL of water in microcentrifuge tubes. These are the total samples for gel analysis, and are diluted 4x. Incubate all centrifuge samples at room temperature for 60 minutes in the rotor. Mark with a sharpie the top of the tube in the rotor to more easily remove the supernatant from the pellet without disrupting it.

Sediment F-actin. Spin the centrifuge samples at 100,000xg for 30 minutes.

Remove supernatant. If the supernatent samples are to be saved, remove $\frac{3}{4}$ of the supernatant (60 uL) and mix with 20 µL of 4x loading buffer in microcentrifuge tubes. Be careful to not disrupt the pellet, which will be a clear gel. A benefit to purifying with an mCherry-tagged Lifeact or LILAC is that the pellet will appear pink if the POI is bound. Finally, go back and carefully remove the rest of the supernatant and discard it.

Resuspend pellet. Resuspend the pellet in 1x loading buffer of the centrifuged volume,

in this case 80 uL. To ensure the pellet is suspended, I like to first add 10 µL of loading buffer to each sample, vigorously pipetting and scraping the tip to remove the pellet from the bottom. Then, after letting this sit for 5 minutes, I add the other 70 µL of loading buffer, pipetting vigorously again, and transferring all 80 µL from the ultracentrifuge to microcentrifuge tubes.

Run gel electrophoresis. Boil samples at 95°C for 5 minutes to denature the protein. Then, add samples to gel wells. Ideally, all samples are run on the same gel to be able to compare band intensities. However, there can be a large number of samples, making this difficult. It is most important that the pellet samples with and without actin are on the same gel. If not all samples fit on the gel, stain them together to minimize differences. Take note of what fraction of each sample is added to the well for later analysis, (i.e., 20 µL of the 80 µL sample is $\frac{1}{4}$ of the total sample).

Analyze gel images. Select the first lane of the gel using the rectangle tool in ImageJ. Add this lane using the Analyze¿Gels¿[Select first lane] option in ImageJ. Move the box and use Analyze¿Gels¿[Select next lane] to add the other lanes. Use Analyze¿Gels¿[Plot lanes] to plot the lanes. Use the line tool to draw the band boundaries, and measure the intensity in the area with the wand tool, saving the results. This results in actin and POI band values for each sample.

Fit data. For each group of samples (total, pellet, background), account for loading differences by dividing by the fraction that was added to the gel. For the total sample, multiply by 5, as 1/5 of the sample was removed. Create a reference curve by plotting the concentration of POI added versus the intensity of that band in the total sample. This should be linear, and can serve as a reference for converting between band intensity and concentration. For the pellet, subtract the background sedimentation from the pellet for each sample. Measure the actin for each pellet sample, and divide the actin in each pellet by the average actin in all of the pellets to determine their relative actin amounts. Divide the

POI band intensity for each sample by its corresponding relative actin value, to normalize for loading inconsistencies. Then plot as a function of initial POI concentration. If bound, the amount of POI should be greater than background sedimentation. Also, if the binding does not saturate, there is either too much actin or too little POI at the highest concentrations. Once there is saturated binding, fit this data to a Hill function or hyperbolic curve to determine the binding constant (Figure 2.6).

Hyperbolic fit:

$$Y = \frac{B_{max}C}{K_d + C}$$

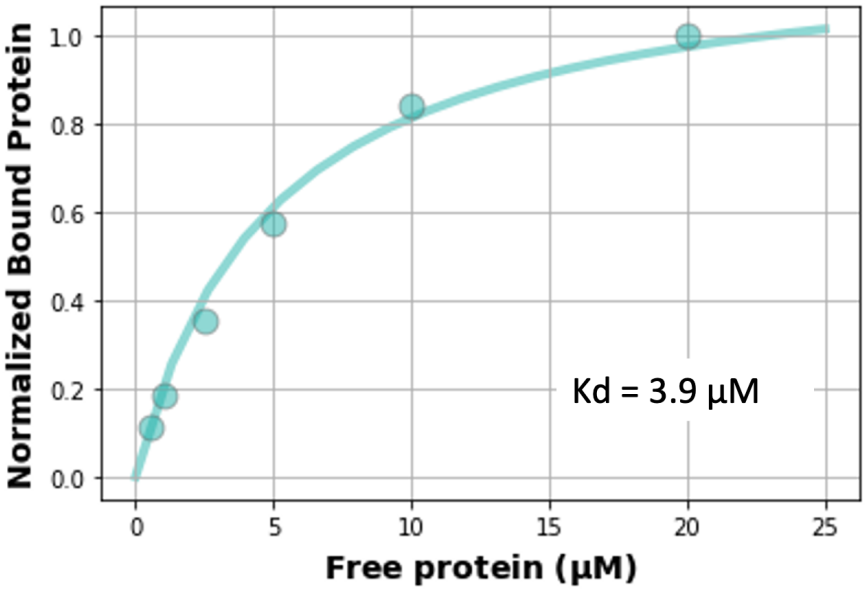

Figure 2.6: Actin cosedimentation of Lifeact. Free protein plotted against bound protein in the pellet after co-sedimentation to determined binding affinities of Lifeact (Kd=3.9 µM). Data were normalized to the maximum observed and fitted to a hyperbola.

2.9 Image Processing

Images taken using LILAC can be processed and analyzed in a variety of ways to gain clearer visualization of actin, insight into LILAC dynamics, and more. All image processing is done in FIJI, an open-source and widely used software. The methods of image acquisition and desired information determine which image processing methods are most useful with LILAC.

2.9.1 Image subtraction

If images of LILAC have been acquired both pre- and post-excitation, image subtraction can be used to highlight the actin structures labeled by LILAC with blue light (Figure 2.7). In FIJI, make a substack of the pre-excitation image. Then, using the Image Calculator plug-in, select the post-excitation image(s) and subtract the pre-excitation substack. If the 32-bit float box is not selected, negative values will be floored to zero. This means that areas such as the center of the cell, where LILAC is depleted post-excitation will all be floored to zero. The contrast will likely need to be adjusted in this image. If the 32-bit float box is selected, enriched, positive values will be white, unchanged values will be zero, and depleted, negative values will be black. This allows for visualization of areas where LILAC is depleted upon excitation. It is suggested to try both and see which images are preferred.

2.9.2 Actin Labeling Ratio

To quantify the labeling of actin for each image, we use the actin labeling ratio (ALR). This is the ratio of the average pixel intensity of the outer lamellipodial actin ring and the average pixel intensity of the cell interior (Figure 2.8a). The higher the ALR, the brighter the lamellipodial actin is in relation to the interior of the cell. This is useful in that it quantifies how bright the actin ring looks when looking at the cell. If just the lamellipodial ring intensity was used, it would be difficult to know if the actin was labeled well, or if the

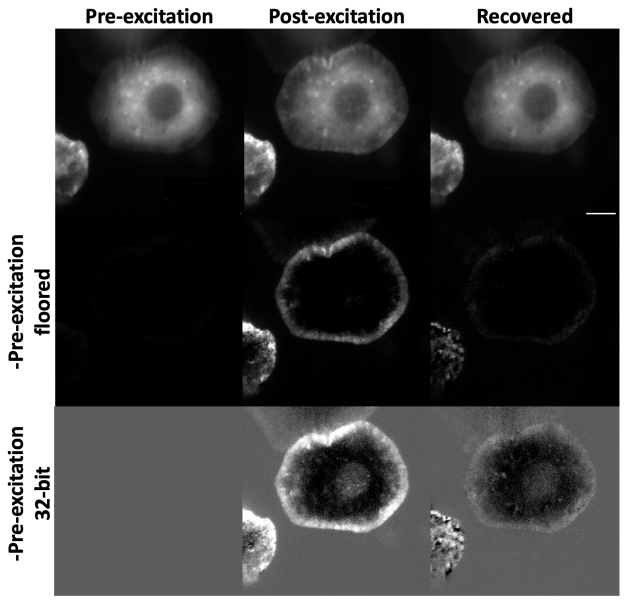

Figure 2.7: Image subtraction highlights actin structures in live cells. TIRF images of an S2 cells expressing LILAC at various stages of excitation in their raw from (top). The pre-excitation image can be subtracted by either flooring negative values (center row) or by outputting a 32-bit float, showing where LILAC has been depleted.

cell was brighter overall. In addition to these pixel intensities, if we also measure the area of each of these, then we can calculate the overall average cell intensity. To measure this, using the freehand selection tool, trace the outer edge of the cell and save the region of interest (ROI) using the [t] shortcut. Next, trace the inner boundary of the lamellipodia and save the ROI. Select both ROIs and use the XOR function to create an ROI that contains only the lamellipodial ring. Use multi measure to record the average pixel intensity for each frame, as well as whatever shape parameters are of interest for both the outer and inner regions.

$$ALR = \frac{mean\ pixel\ intensity_{outer}}{mean\ pixel\ intensity_{inner}}$$

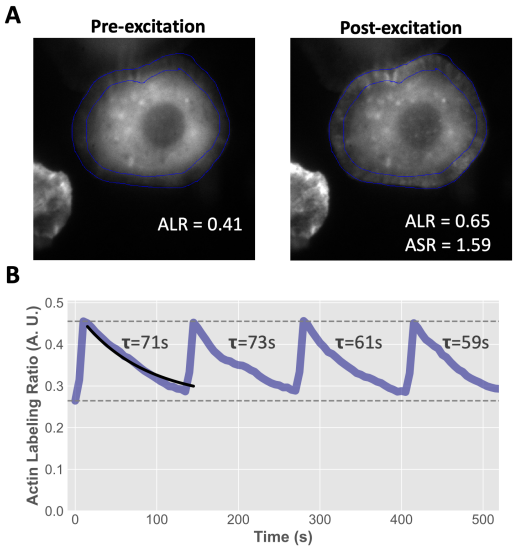

Figure 2.8: Actin labeling ratio (ALR) is used to measure actin binding in S2 cells. (a) TIRF images of an S2 cells expressing LILAC pre- and post-excitation. Blue highlights the traced regions for calculating the ALR. (b) ALR over time for a repeatedly-excited cell. Recovery time constants were calculated using exponential fit.

2.9.3 Switching Ratio

As a proxy for the ratio of LILAC-actin binding in the light versus the dark we use the switching ratio (Figure 2.8a). The switching is defined as the ALR post-excitation and pre-excitation, such that a switching ratio over 1 indicates enriched actin labeling post-excitation.

$$SwitchingRatio = \frac{ALR_{post}}{ALR_{pre}}$$

2.9.4 Recovery Time Constants

It is important to know the recovery time of LILAC when determining how often to excite cells for optimal imaging results. For example, if cells are recovering to the dark state quickly, it is important to minimize the time between blue light excitation and capturing the post-excitation image. Conversely, if cells are recovering slowly, if multiple excitations are desired with both pre and post-excitation images, enough time must pass such that LILAC fully

recovers to the dark state. To do this, when acquiring the images, pulse blue light, then return to the dark state, just imaging the FP. Then acquire the ALR of the cell for each frame, and plot it. Then, fit the data to an exponential fit (Figure 2.8b).

2.9.5 Correlative Imaging

Another advantage of imaging actin with LILAC is the ability to use correlative imaging (Figure 2.9). Correlative imaging is the method of perturbing the fluorescence signal in a controlled manner, and then applying lock-in detection analysis to amplify the signal of interest [Marriott et al., 2008]. This highlights pixels that are responding temporally to the perturbation, allowing for increased visualization of dynamic, but dim pixels. In this case, we modulate the fluorescence using activation of LILAC with blue light. First, identify a rectangular region in the lamellipodia that responds to blue light excitation in FIJI. This response function should look similar to the ALR. Then, sum the intensity of this area for each frame to obtain the response function. Obtain the Pearson correlation coefficient between the response function and the intensity of each pixel along the time axis. To create a single image, use the entire time axis, or to create a movie, use a sliding window.

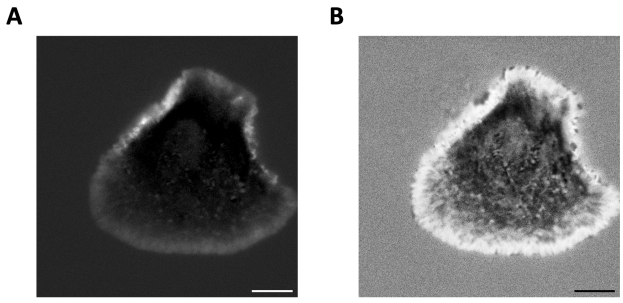

Figure 2.9: Correlative imaging with LILAC. (a) Post-excitation image of an S2 cell with pre-excitation image subtracted. (b) OLID (optical lock-in detection)26 image of an S2 cell. White pixels are correlated, black anticorrelated, and mid-gray are uncorrelated. We used the first 50 frames of a movie (0.5 s/frame) where the excitation pulse arrives in frame 2 to generate the OLID image.

CHAPTER 3

LILAC: ENHANCED ACTIN IMAGING WITH AN OPTOGENETIC LIFEACT

This chapter is derived from the following publication:

Kroll, K. L., French, A. R., Sosnick, T. R., and Rock, R. S. LILAC: Enhanced actin imaging with an optogenetic Lifeact. *Nature Methods* **20**, 214-217 (2023).

3.1 Abstract

Lifeact is a popular peptide-based label of actin filaments in live cells. We have designed an improved Lifeact variant, LILAC, that binds to actin in light using the LOV2 protein. Light control allows the user to modulate actin labeling, enabling image analysis that leverages modulation for an enhanced view of F-actin dynamics in cells. Furthermore, the tool reduces actin perturbations and cell sickness caused by Lifeact overexpression.

3.2 Main

Reliable actin visualization is vital for various fields of biological research. Phalloidin is the gold standard for actin filament visualization; however, it is membrane impermeable and limited to fixed staining. Fluorescent protein-tagged actin monomers, utrophin, F-tractin, actin chromobodies, and Lifeact [Melak et al., 2017] are all alternatives for live-cell imaging. Lifeact, the first 17 amino acids of yeast actin binding protein 140, is the dominant actin filament label in live cells [Riedl et al., 2008].

Lifeact, however, has undesirable effects, including sterility in Drosophila, morphology changes in mesenchymal stem cells, and altered actin patch and cytokinetic ring dynamics in fission yeast [Spracklen et al., 2014, Flores et al., 2019, Courtemanche et al., 2016]. These side effects are likely due to competition between Lifeact and other proteins, such as cofilin and

myosin, for binding at the actin D-loop [Belyy et al., 2020, Kumari et al., 2020]. To address this problem we designed LILAC (Light-Induced Localization to ACtin), an optogenetic tool that has low actin affinity in the dark. When photoactivated, LILAC binds and labels actin filaments in 1 s. LILAC photocycles and returns to the low-affinity state in seconds to minutes, thereby minimizing side effects. Light control also enables additional image analysis capabilities.

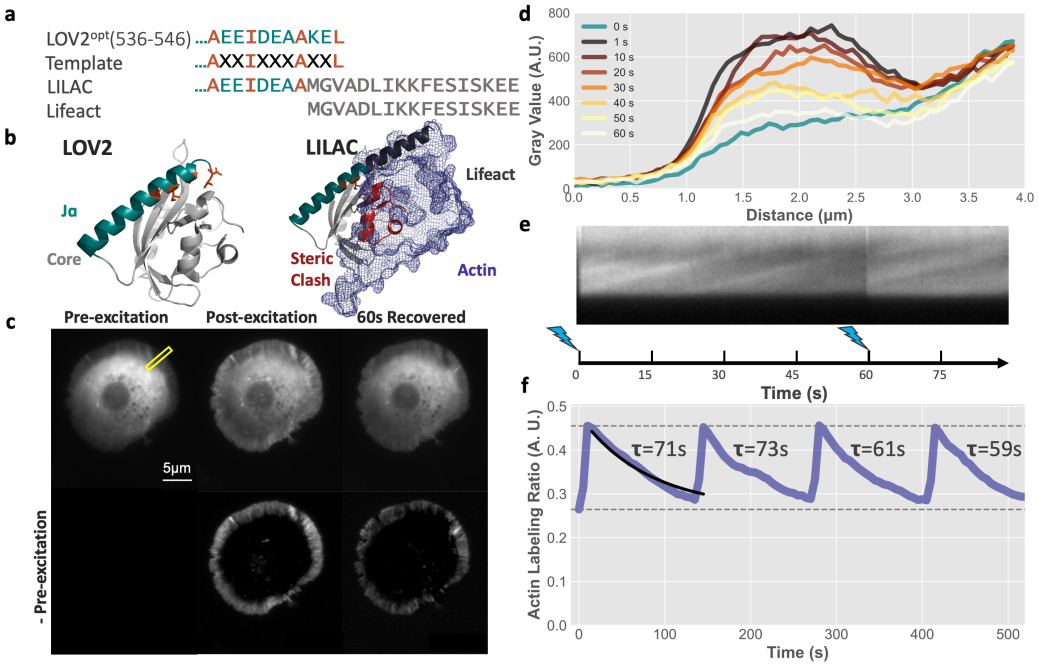

Figure 3.1: LILAC reversibly binds actin in S2 cells. a, Sequences of the LOV2 C-terminal Jα helix (turquoise) and Lifeact (gray). The template was created by integrating Lifeact while retaining the hydrophobic residues (orange) that interact with the core of LOV2. b, Structural representations of LOV2 and LILAC. Actin (blue) is shown bound to Lifeact from Protein Data Bank (PDB) 7AD9. Light gray, LOV2 core; turquoise, Jα helix; orange, key hydrophobic residues. LOV2 residues that sterically clash with actin in the dark state are shown in dark red. The LILAC model was created by extending the Jα helix of AsLOV2 (PDB 2V0W) with the residues of Lifeact in helical form. c, Total internal reflection fluorescence images of a representative S2 cell (from $>$ 300) that is expressing LILAC taken before, during and after excitation with blue light. Scale bar, 5 µm. d, Line scan of the cell area highlighted in yellow in c before blue light excitation at 0 s and 1–60 s after excitation, where 0 µm is outside of the cell. e, Kymograph of the outer cell edge highlighted in yellow in c, where the top is the inside of the cell, and the bottom is outside the cell.

Figure 3.1 continued: f, ALR (actin labeling ratio) of a repeatedly excited cell. The black line is an example single exponential fit of the first recovery. Tau represents the time constant for each recovery, obtained from single exponential fits. Dashed lines indicate the minimum and maximum ALRs.

In our design we used AsLOV2, the second light-sensitive light–oxygen–voltage (LOV) domain from Avena sativa (oat) phototropin 1. In response to blue light the flavin chromophore forms an adduct with C450, resulting in conformational changes in the core [Crosson and Moffat, 2001, Kennis et al., 2004]. These changes disrupt the seven-residue amino-terminal A'α helix and 24-residue carboxy-terminal Jα helix, causing them to unfold [Halavaty and Moffat, 2007]. This light-dependent conformational change of LOV2 has been used in a variety of optogenetics tools [Strickland et al., 2008, French et al., 2017, Niopek et al., 2014, Guntas et al., 2015, Strickland et al., 2012]. Mutations and buffer conditions can alter recovery times [Zayner and Sosnick, 2014, Zayner et al., 2019, 2013, Alexandre et al., 2007] or mimic the photoexcited (I539E) and dark states (C450A) as well as assist in design [Harper et al., 2004, Matsuoka and Tokutomi, 2005, Harper et al., 2003].

Using previous LOV2-based optogenetic platforms as a guide, we designed LILAC to maintain hydrophobic contacts with the Jα helix (Figure 3.1a). These contacts help cage Lifeact in a manner that sterically blocks actin binding when the Jα helix is folded (Figure 3.1b). Upon unfolding of the Jα helix, Lifeact is uncaged and binds actin filaments.

After blue light excitation, Drosophila melanogaster S2 cells expressing mCherry-LILAC have increased fluorescence in the outer lamellipodial actin ring as compared with the dark state (Figure 3.1c and Supplementary Videos 1–4). This labeling decays with a time constant similar to wild-type LOV2, suggesting that dark-state reversion controls actin binding affinity (Figure 3.1d). By subtracting the pre-excitation image, we effectively eliminate the background fluorescence from the cytosolic, unbound LILAC. This subtraction highlights the structures of interest (Figure 3.1c and Figure 3.4a–d), increases the image contrast in the lamellipodium 2.5-fold (Figure 3.41e) and reduces the influence of variations in cellular

thickness. Optimal subtraction requires excess LILAC such that the cytosolic signal is unaffected by actin binding. Lower LILAC expression levels can lead to over-subtraction and regions of negative signal.

Subtraction of the pre-excitation image also enhances kymographs of actin retrograde flow (Figure 3.1e and Figure 3.4c,d). Retrograde flow occurs at a rate of 3.5 ± 0.12 µm/min (mean ± s.e.m.), similar to the rate of 4.0 ± 0.44 µm/min reported previously [Rogers et al., 2003]. Beyond lamellipodia, post-excitation images also show small patches in the cell body (Figure 3.5) and filopodia in landing S2 cells (Figure 3.6). Phalloidin staining confirmed that central and peripheral structures labeled by LILAC and Lifeact are actin rich (Figure 3.7). Moreover, LILAC coupled with pulsed excitation enables other enhanced imaging modes such as optical lock-in detection (OLID) [Marriott et al., 2008] (Figure 3.8), which shows regions of correlated actin labeling. A single excitation pulse train can be analyzed with either background subtraction or OLID, depending upon user need.

To quantify labeling over time, we define the actin labeling ratio (ALR) as the ratio of mean pixel intensity in the actin-rich lamellipodium to the mean pixel intensity of the cell's interior (Figure 3.1f and Figure 3.8c,d). S2 cells expressing larger amounts of LILAC tend to have lower maximum ALRs ($R^2 = 0.27, P = 2.3 * 10^{-6}$, Figure 3.9a), which is likely to be due to a high background level from excess LILAC. We found that the maximum ALRs of LILAC are similar to Lifeact, implying that the activated LILAC binds filamentous (F) actin with a similar affinity and specificity as Lifeact(Figure 3.9c). To confirm this, we expressed mCherry-Lifeact and mCherry-LILACI593E (photoexcited mimetic) and determined their affinity to F-actin through co-sedimentation. The binding affinities of Lifeact and LILACI539E were K_d = 3.9 µM and 3.4 µM, respectively (Figure 3.10), between the reported Lifeact values of 2.0 µM [Riedl et al., 2008] and 14.9 µM [Belyy et al., 2020]. We did not measure the LILAC binding affinity for globular (G) actin given that previous work found no detectable binding of Lifeact to G-actin6.

We define the switching ratio as the fold change of the actin labeling from post- to pre-excitation. LILAC has a switching ratio of 1.6, while Lifeact and LILACI539E have switching ratios of 1, as expected (Figure 3.9d). The maximum switching ratio does not correlate strongly with cell intensity ($R^2 = 0.13, P = 1.3 * 10^{-3}$, Figure 3.9b).

The ALR increases after excitation, followed by recovery to pre-excitation levels. This photo-excitation can be repeated multiple times, with no reduction in efficacy (Figure 3.1f). To test sustained actin labeling, we excited cells for up to 60 s, with little reduction in labeling (Figure 3.11a and Supplementary Videos 3,4). We varied excitation time and found that the maximum switching ratio increased with increased excitation time but saturated between 500 ms and 1 s (Figure 3.11b).

We next examined the dark state recovery process to determine how rapidly the cells reset after imaging. On average, cells recover with a time constant of 63 s, close to the characteristic 80 s in vitro time constant of LOV2 [Halavaty and Moffat, 2007] (Figure 3.12a,b). We repeated this measurement with our T406A/T407A mutation that stabilizes the N-terminal A'α helix, reduces the recovery time constant and increases caging12,17. The average time constant decreased to 50 s, similar to the 54 s time constant measured previously17 (Figure 3.12a,b).

Unexpectedly, we observed considerable cell-to-cell variability in recovery times. For a given cell, however, the first and second recovery times were strongly correlated ($R^2 = 0.64, P = 2.4 * 10^{-17}$, Figure 3.12a). This correlation suggests that each cell has its own dark state recovery time that is linked to its cellular state (for example, metabolite concentrations or pH)20,21. To determine whether we could easily perturb recovery times, we added imidazole to cell media, given that LOV2 recovery time is known to be reduced by imidazole in vitro21. We found that in vivo recovery times depended strongly on imidazole ($R^2 = 0.52, P = 3.5 * 10^{-24}$, Figure 3.12c–e). It decreases the dark state recovery times and cell-to-cell variance without affecting the intracellular correlation between time constants

($R^2 = 0.77, P = 7.3 * 10^{-46}$, Figure 3.12d,e). The strong dependence of LILAC release on imidazole suggests that unbinding from actin is concurrent with dark state recovery. It also shows that imidazole can promote dark-state recovery, which is helpful in generating background-subtracted or OLID movies using multiple excitation cycles.

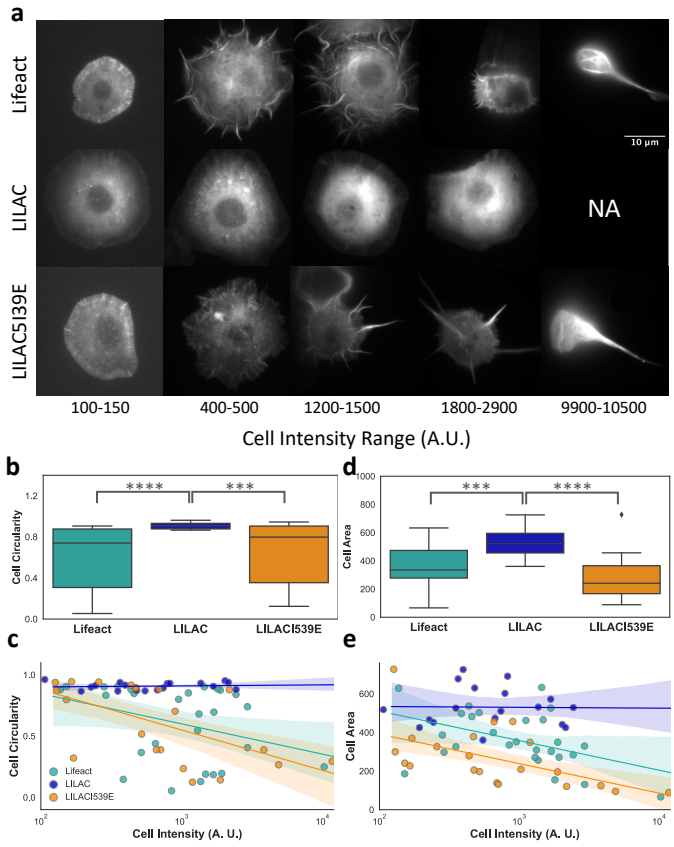

Figure 3.2: LILAC reduces the concentration-dependent side effects of Lifeact. a, Cells at various intensities expressing Lifeact, LILAC and LILACI539E. NA, not applicable. Scale bar, 10 µm. b,d, Quantification of cell circularity (b, $P = 1.57 * 10^{-4}$; LILAC-Lifeact, $P = 3.5 * 10^{-5}$; LILAC-LILACI539E, $P = 4.7 * 10^{-4}$) and cell area (d, $P = 3.77 * 10^{-6}$; LILAC-Lifeact, $P = 6.7 * 10^{-4}$; LILAC-LILACI539E, $P = 7.2 * 10^{-7}$) of Lifeact, LILAC and LILACI539E. The center line represents the median. Boxes span the 25th and 75th percentiles. Whiskers extend from the 25th percentile minus 1.5 fold the interquartile range (IQR) and from the 75th percentile plus 1.5 fold the IQR. Data beyond the whiskers represent outliers and are plotted individually.

Figure 3.2 continued: c,e, Cell circularity (c) and cell area (e) are shown as a function of intensity with a linear regression fit to log-transformed data and shaded regions indicate the 95% confidence interval. Circularity in b and c is arbitrary units (a.u.) and Cell area in d and e is in square microns (μm^2). For b, and d, overall P values are for a one-way ANOVA test (n = 27 for Lifeact, n = 18 for LILAC, n = 23 for LILACI539E), with a post-hoc Dunn test for pairwise P values. ***P $\leq$ 0.001, ****P $\leq$ 0.0001.

We examined the deleterious effects of high mCherry-Lifeact expression on S2 cells. At low expression levels, cells are circular with the characteristic lamellipodial actin ring at the outer edge. However, at increasing concentrations of mCherry-Lifeact, cells form long F-actin bundles and protrusions (Figure 3.2a). Such cells have irregular shapes and impaired spreading onto the coverslips. Due to its minimal F-actin binding in the dark, LILAC reduces these morphological defects. At the highest level of expression, LILAC-expressing cells maintain their circular shape and lack the prominent F-actin bundles (Fig. 2a). Cells overexpressing Lifeact have significantly reduced circularity compared with LILAC (Kruskal–Wallis test, $P = 1.57 * 10^{-4}$, Figure 3.2b,c). Circularity also depends more on Lifeact ($R^2 = 0.12$) than on LILAC expression level ($R^2 = 0.012$). Lifeact-expressing cells also have reduced area as a function of expression ($R^2 = 0.21$). This effect is absent when expressing LILAC ($R^2 = 2.8 * 10^{-4}$, Figure 3.2d,e). Moreover, the photoexcited-mimetic LILACI539E recapitulates the morphological defects seen in S2 cells overexpressing mCherry-Lifeact (Figure 3.2a). Similarly to mCherry-Lifeact, circularity ($R^2 = 0.40$, Figure 3.2b,c) and area ($R^2 = 0.36$, Figure 3.2d,e) correlate with expression level. Overall, we find that LILAC is nearly inert in the dark, even when highly overexpressed, due to effective caging of the Lifeact peptide. This caging minimizes Lifeact-induced perturbations to the actin cytoskeleton and cell morphology.

In conclusion, LILAC enables additional imaging modes that leverage photoswitching while also minimizing cytoskeletal perturbations. By subtracting the pre-excitation image, we substantially reduce the cytosolic background and obtain enhanced actin cytoskeleton images. For cytosolic background subtraction, current methods require a separate cytosolic

fluorescent label, whereas LILAC enables background subtraction with a single construct. LILAC can be tagged with various fluorophores depending on user needs. For example, if tagged with a green fluorescent protein (GFP), excitation of the fluorophore and LOV2 would be simultaneous. This enables the use of a single excitation line but eliminates the option of pre-excitation image subtraction. Alternatively, GFP may be used to label a second protein of interest, which can be imaged given the understanding that such imaging will also excite the LILAC. An image sequence of pre-excitation LILAC, GFP-protein of interest, and post-excitation LILAC would enable the same background subtraction as in Fig. 1c. Thus, LILAC can be used in multiple ways.

3.3 Methods

3.3.1 DNA preparation

A LILAC G-block was purchased from Integrated DNA Technologies and incorporated into a pet21 vector containing 6xHis-mCherry-TEV using Gibson assembly containing AsLOV2 (401–543) with the mutations G528A/I532A/N538E for improved switching [Strickland et al., 2010] to make LOV2opt (Figure 3.3a,b). LOV2 was removed to create the pET21-mCherry-Lifeact vector using the NEB Q5 protocol (Figure 3.3c). Next, we used Gibson assembly to incorporate mCherry-TEV-LILAC into a pMT vector from the Glotzer Laboratory (The University of Chicago) (Figure 3.3d). The TEV protease site was then replaced with a 3xGGS linker using the NEB Q5 protocol (Figure 3.3e). LOV2 was removed to create the pMT-mCherry-Lifeact vector using the NEB Q5 protocol (Figure 3.3f). The T406A/T407A and I539E mutations were created using the NEB Q5 protocol.

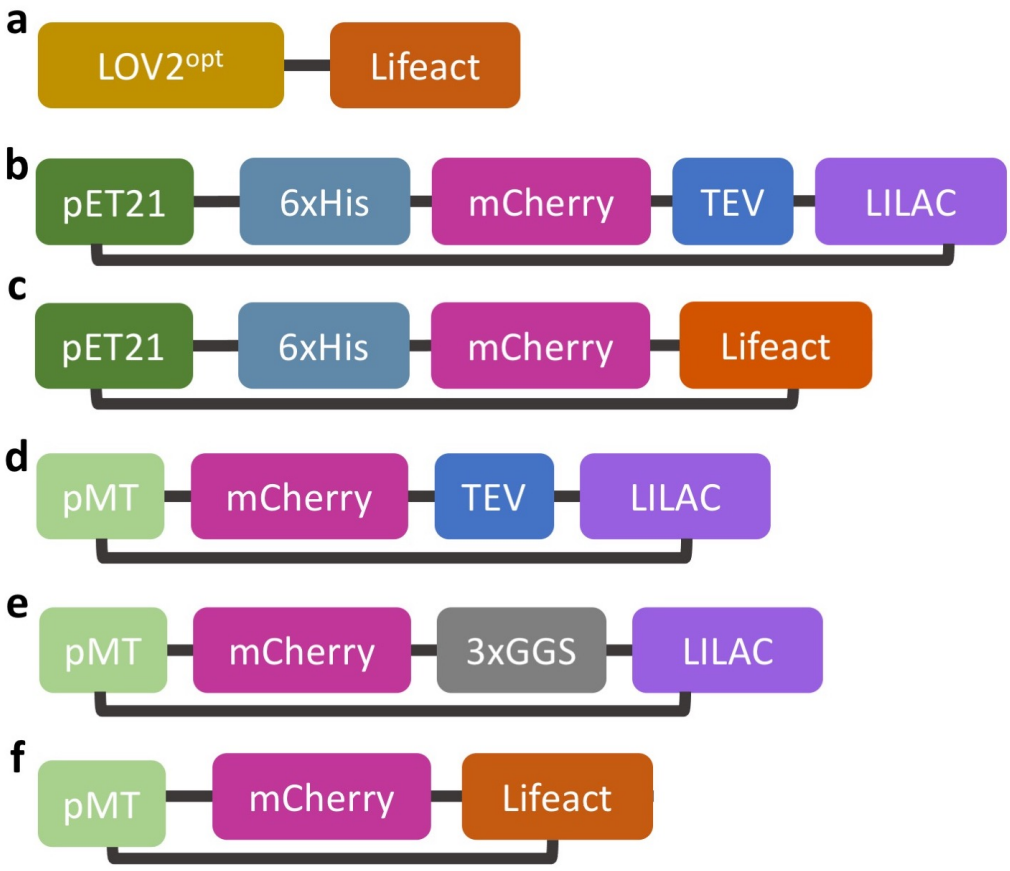

Figure 3.3: LILAC constructs. Schematics of LILAC (a) and other vectors used. a, Schematic of LILAC, including LOV2opt(AsLOV2401-543 G528A/I532A/N538E). Vectors used for protein expression (b,c) and expression in S2 cells (d–f), where TEV is the TEV protease cleavage site.

3.3.2 Cell maintenance

Insect S2 cells from the Fehon Laboratory (The University of Chicago) were maintained in Schneider's insect media (Sigma) with insect media supplement (Sigma), 50 units/ ml penicillin and 50 µg/ml streptomycin (Thermo). Cells were split 1:6 every 4–6 days at around 10–15 million cells/ml at 20 ml in T75 flasks.

3.3.3 Transfection and imaging preparation

Cells were transfected as previously described [Han, 1996]. In brief, 2 ml fast-growing cells were added at 1.35 million cells/ml to a six-well plate. Dimethyldioctadecyl-ammonium bromide (DDAB) at 250 µg/ml was added to the media in a 1:2 ratio and left for 10 min. Then, the DDAB–media mixture was added to 500 ng pMT vector to reach 150 µl and left for 15 min. This was added dropwise to the cells. One day later, cells were induced with 1.5 µl 0.7 M $CuSO_4$. Cells were transferred 1 day later on glass-bottom dishes coated with 15 µl 0.5 mg/ml concanavalinA [Buster et al., 2010]. For Figure 3.12, 1 M pH 7.5 sterile filtered imidazole was added to the media to reach the final desired concentration. Unless otherwise noted, cells were imaged after 45 min to allow for cell spreading.

3.3.4 Fixation and staining

Cells were transfected with either LILAC or Lifeact and spread onto concanavalin A-coated coverslips 1 day after induction. After removal of the media, cells were rinsed with PBS, and 4% paraformaldehyde (diluted in PBS) was added for 15 min under blue light. Cells were permeabilized with 0.2% Triton X-100 in PBS. After rinsing with PBS, cells were stained with Alexa Fluor 488 phalloidin and rinsed again with PBS.

3.3.5 Imaging

Dishes were imaged using a ×100, 1.65 numerical aperture objective (Olympus) on a custom-built total internal reflection microscope using an electron-multiplying charge-coupled device (EMCCD) camera (iXon; Andor Technologies) with an mCherry-specific emission filter. This microscope was controlled with the open source Micro-Manager program (`https://micro-manager.org/`). Unless otherwise noted, cells were excited first with 561 nm, then with 488 nm and 561 nm, and recovery images were taken with 561 nm excitation only, all at 1% power for 500 ms exposure with an electron multiplication gain of 200 with no delay time

between images. This results in an irradiance of 1 W/ cm^2 of blue light, which is 10–20-fold the level typically used to saturate LOV2 [Ruijgrok et al., 2021]. Cells excited more than twice were imaged in exactly the same manner with 5 s between images instead of 500 ms. Cells in Fig. 2 were imaged on the same microscope on the same day to best guarantee that cells of the same brightness are expressing similar protein levels.

3.3.6 Image analysis

Outer and inner rings of the cells were traced by hand, and kymographs were created in FIJI (`https://imagej.net`). Inset images were created using a FIJI macro (`https://imagej.nih.gov/ij/macros/tools/Zoom_in_Images_and_Stacks.txt`). Brightness, cell perimeter, area, circularity and roundness values were exported from FIJI for inner and outer cell areas for each cell. From this, actin labeling ratio (ALR) and switching ratios were calculated.

$$ALR = \frac{mean\ pixel\ intensity_{outer}}{mean\ pixel\ intensity_{inner}}$$

$$SwitchingRatio = \frac{ALR_{post}}{ALR_{pre}}$$

Time constants were calculated by fitting ALR to a single exponential. Data analysis and figures were generated using Python scripts.

We quantified morphological changes by calculating the cell circularity, area and roundness. When cells are circular, this value is 1, and when cells have large perimeters, it approaches 0. R^2 values were calculated using the circularity or the cell area versus the logarithm of the cell intensity:

$$Circularity = \frac{4\pi Area}{Perimeter^2} = \frac{4\pi(\pi r^2)}{(2\pi r)^2}$$

3.3.7 OLID image analysis

OLID analysis was performed in a similar manner to the original report26. We identified a rectangular region of the lamellipodium with LILAC enrichment after a blue light pulse, and summed this region to determine a LILAC response function. This response function had a similar rise and decay as shown in Fig. 1f. We determined the Pearson correlation coefficient for each pixel (along the time axis) with the response function, to generate the single static image shown in Figure 3.8. To generate the related movie, we performed similar correlations using a sliding window over time (30 frames, offset 5 frames at a time), where the window was applied to both the response function and the source movie.

3.3.8 Protein expression and purification

Proteins were expressed and purified as previously described27. In brief, all proteins were expressed in Escherichia coli BL21 (DE3) cells grown in lysogeny broth at 37°C to an optical density at 600 nm of 0.6 and induced with 1 mM isopropyl-β-D-thiogalactopyranoside. After 18 h in the dark, cells were pelleted and resuspended in 50 mM Tris (pH 8.0), 100 mM NaCl, 5 mM imidazole, 5% glycerol. Cells were lysed by sonication and clarified by centrifugation at 14,000 g for 40 min. Proteins were purified using metal affinity chromatography. After purification the protein was dialyzed into assay buffer (25 mM KCl, 25 mM imidazole pH 7.5, 1 mM K-EGTA, 4 mM $MgCl_2$, 1 mM dithiothreitol).

3.3.9 Co-sedimentation

Co-sedimentation assays were performed as previously described [Heier et al., 2017]. In brief, G-actin was polymerized, and filaments were stabilized with phalloidin. After preparation of the protein of interest by a hard spin to remove aggregates (100,000 g for 10 min), protein was incubated with 0.5 µM actin at room temperature for 60 min in assay buffer. After centrifugation at 100,000 g for 30 min, the supernatant was removed and the pellet was

resuspended before analysis of the samples using SDS-PAGE. Gels were analyzed in FIJI (`https://imagej.net`). To account for loading differences, pelleted protein was normalized by pelleted actin in each lane.

$$Y = \frac{B_{max}C}{K_d + C}$$

3.3.10 Statistics and reproducibility

Switching in Figure 3.1c, 3.4a,b, Figure 3.8 was observed at some level in more than 300 cells expressing LILAC under varying conditions in eight biological replicates. Actin patches as seen in Figure 3.5 were observed in 50 LILAC-expressing cells after excitation in eight biological replicates. Filopodial labeling was observed in all five cells that were observed with filopodia. Figure 3.7a is a representative image of 15 Lifeact and phalloidin co-labeled cells. Figure 3.7b is a representative image of 25 LILAC and phalloidin co-labeled cells.

3.3.11 Data availability

The sequence of pMT-mCherry-LILAC has been deposited to GenBank (OP764687).

3.4 Author contributions

K.L.K., A.R.F., T.R.S., and R.S.R. designed research; K.L.K. performed research; K.L.K., T.R.S., and R.S.R. contributed new reagents/analytic tools; K.L.K., T.R.S., and R.S.R. analyzed data; and K.L.K., A.R.F., T.R.S., and R.S.R. wrote the paper.

3.5 Supplementary Figures

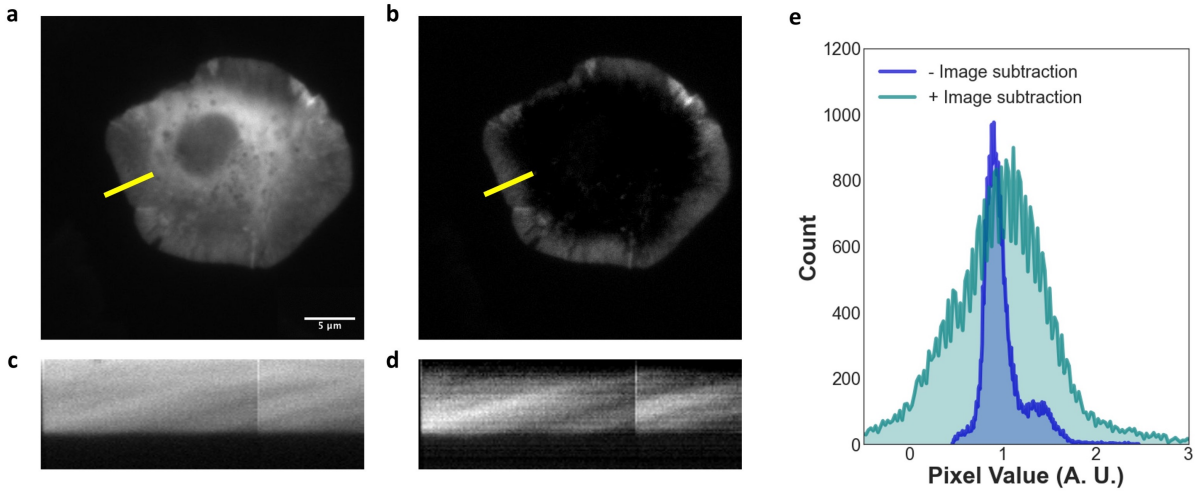

Figure 3.4: LILAC highlights actin structures through background subtraction. TIRF image of an S2 cell expressing LILAC without (a) and with (b) pre-excitation image background subtraction to eliminate cytosolic background. Kymographs of the region in yellow without (c) and with (d) pre-excitation background subtraction. (e) Histograms of normalized pixel intensities in the outer ring of the cell with (CV = 0.58) and without (CV = 0.23) image subtraction.

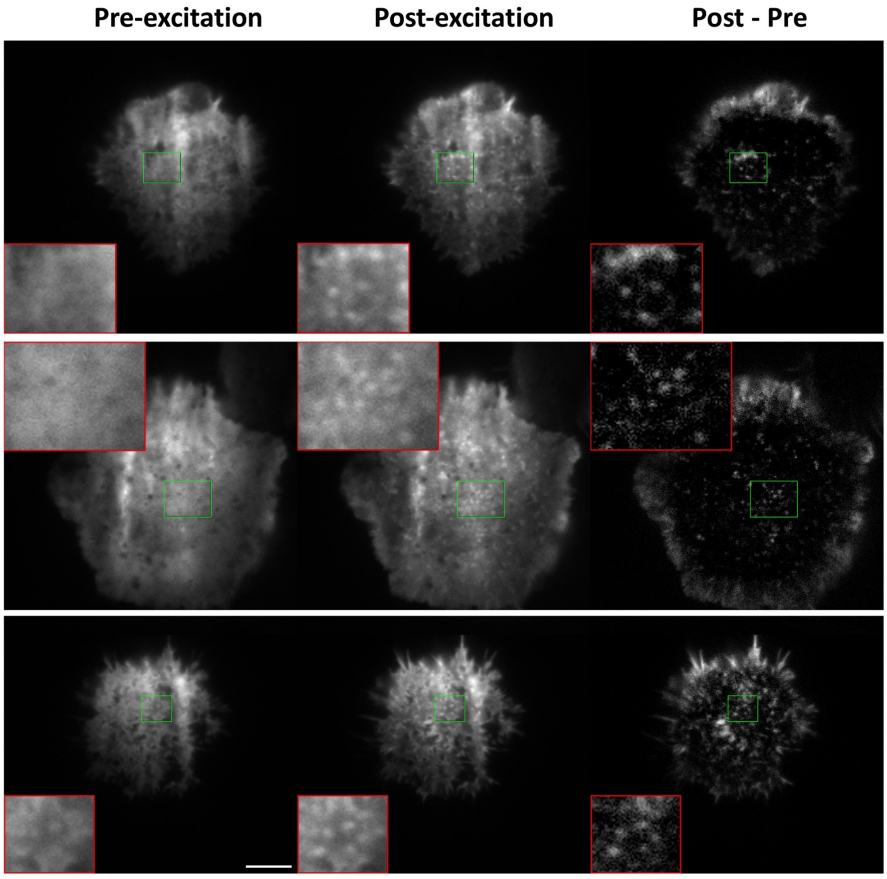

Figure 3.5: LILAC labels actin patches in S2 cells. TIRF images of live S2 cells expressing mCherry-LILAC taken pre- and post-488 nm (blue) laser excitation. Scale bar is 5 µm. Inset images are 3x magnified.

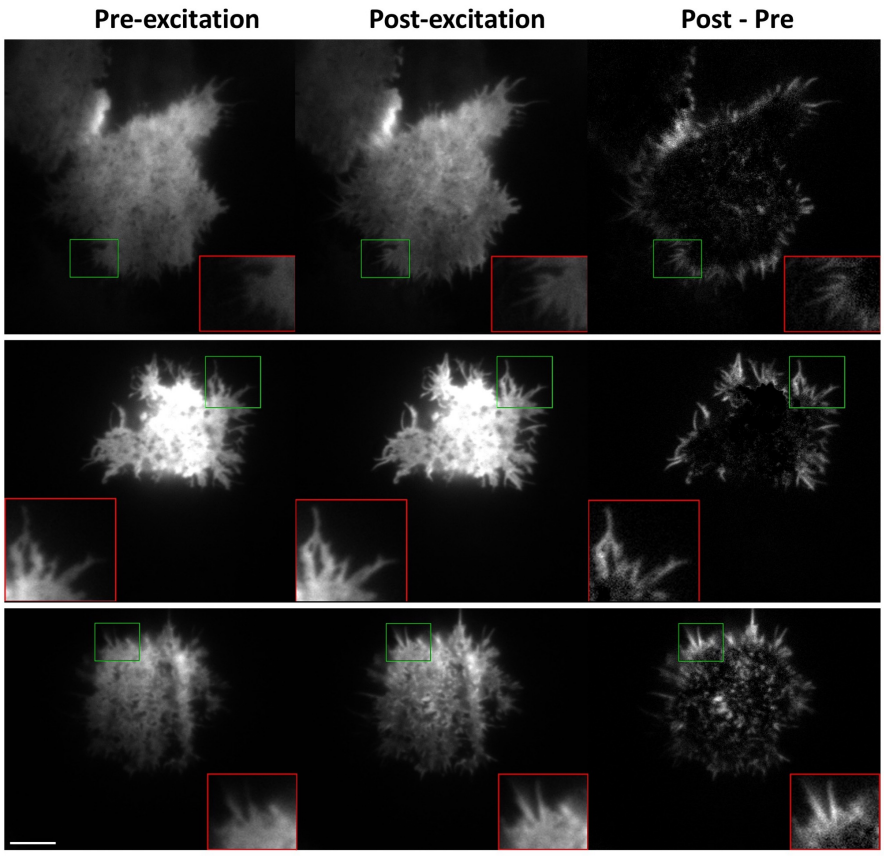

Figure 3.6: LILAC labels filopodia in landing S2 cells. TIRF images of live S2 cells expressing mCherry-LILAC taken pre- and post-488 nm (blue) laser excitation. Cells are imaged as they land on the ConA coated coverslip. Scale bar is 5 µm. Inset images are 2x magnified.

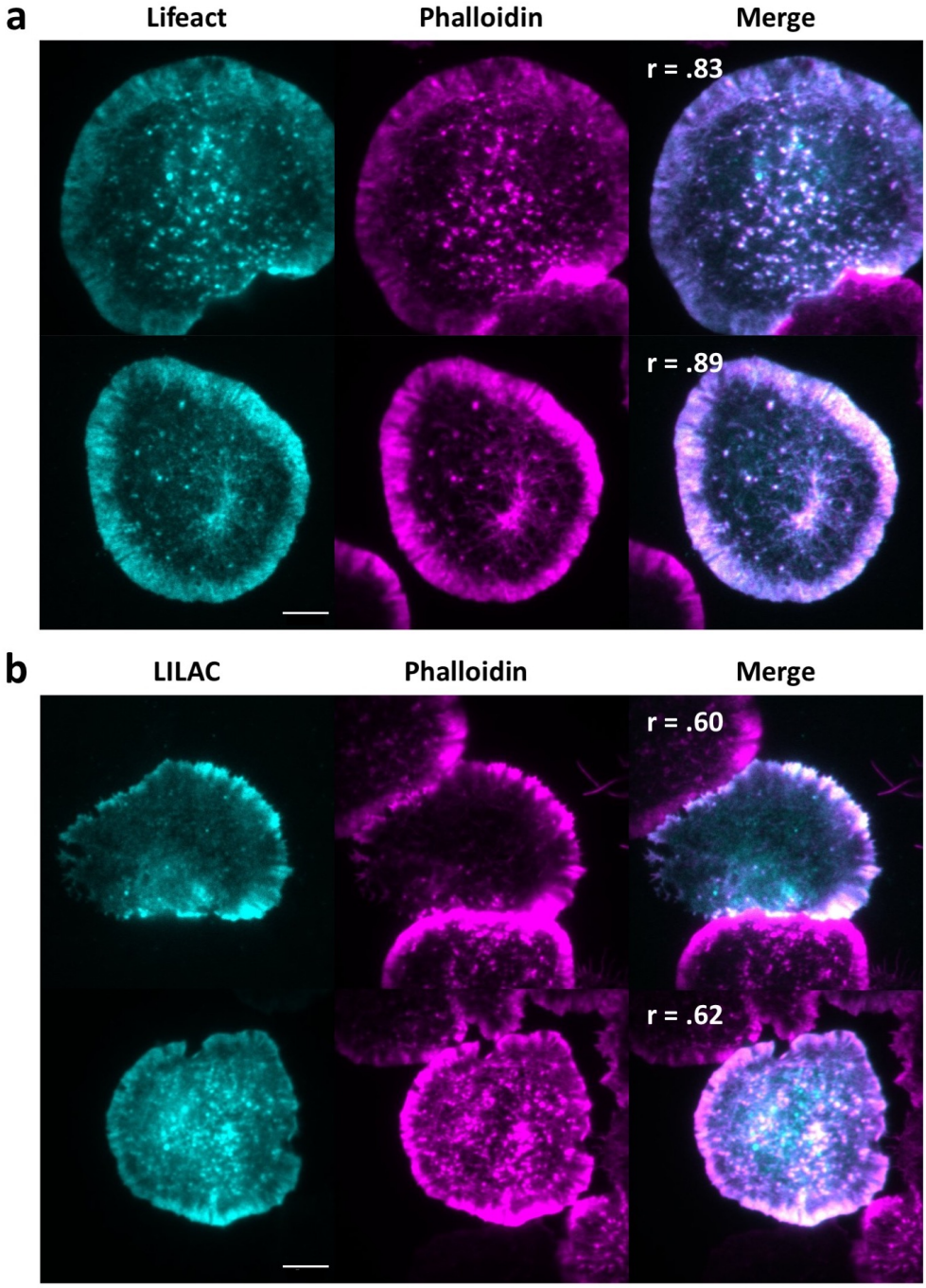

Figure 3.7: Phalloidin, Lifeact, and LILAC co-label actin structures in S2 cells. TIRF images of fixed S2 cells expressing (a) mCherry-Lifeact or (b) mCherry-LILAC stained with phalloidin. Cells were fixed under blue light. Pearson's correlation coefficients are displayed on the merge image. Scale bar is 5 µm.

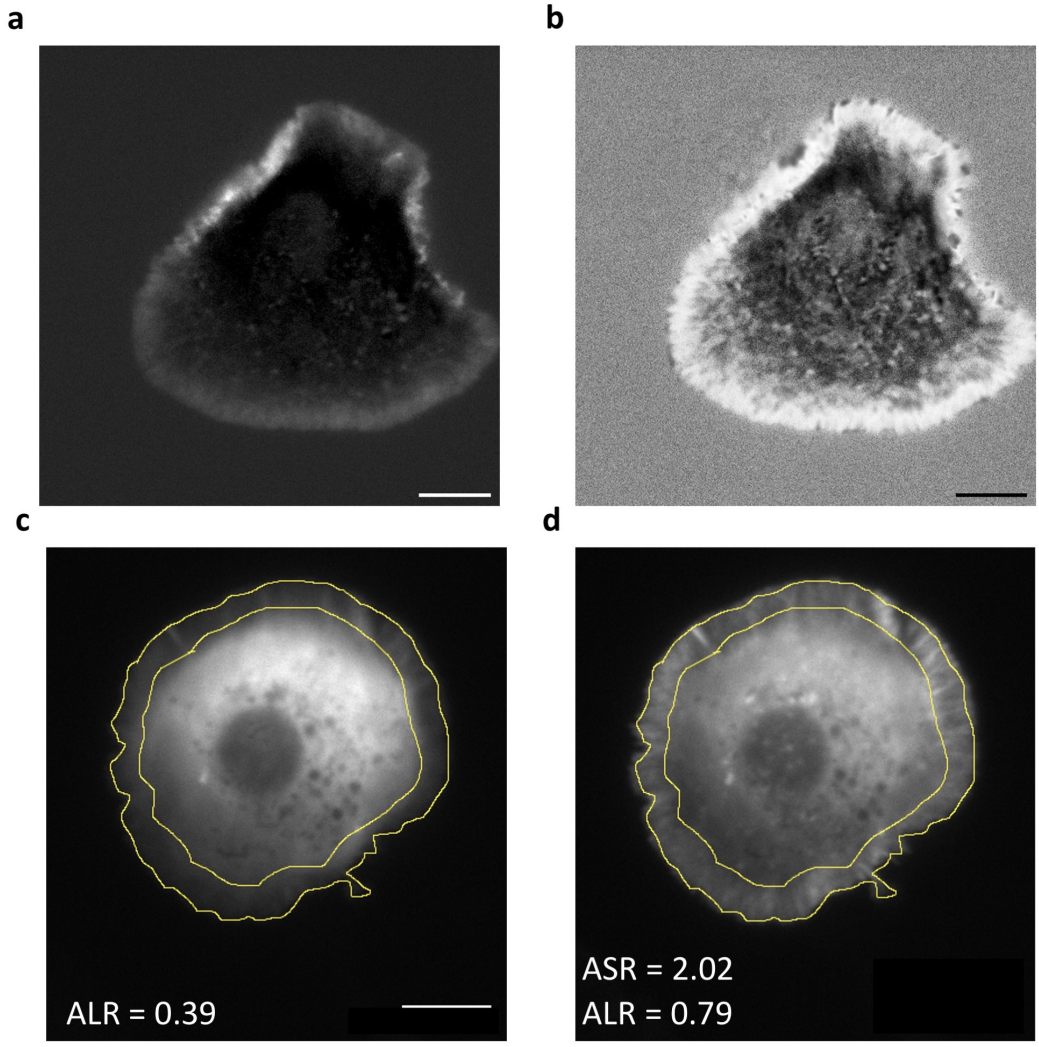

Figure 3.8: Image processing methods with LILAC. (a) Post-excitation image of an S2 cell with pre-excitation image subtracted. (b) OLID (optical lock-in detection) [Marriott et al., 2008] image of an S2 cell. White pixels are correlated, black anticorrelated, and mid-gray are uncorrelated. We used the first 50 frames of a movie (0.5 s/frame) where the excitation pulse arrives in frame 2 to generate the OLID image. An S2 cell expressing mCherry-LILAC before (c) and after (d) blue light excitation. The outer lamellipodial ring and interior disk of cells are hand traced in FIJI (yellow). Scale bar, 5 µm. Actin labeling ratio: $ALR = mean\ pixel\ intensity_{outer}/mean\ pixel\ intensity_{interior}$, actin switching ratio: $ASR = ALR_{post}/ALR_{pre}$.

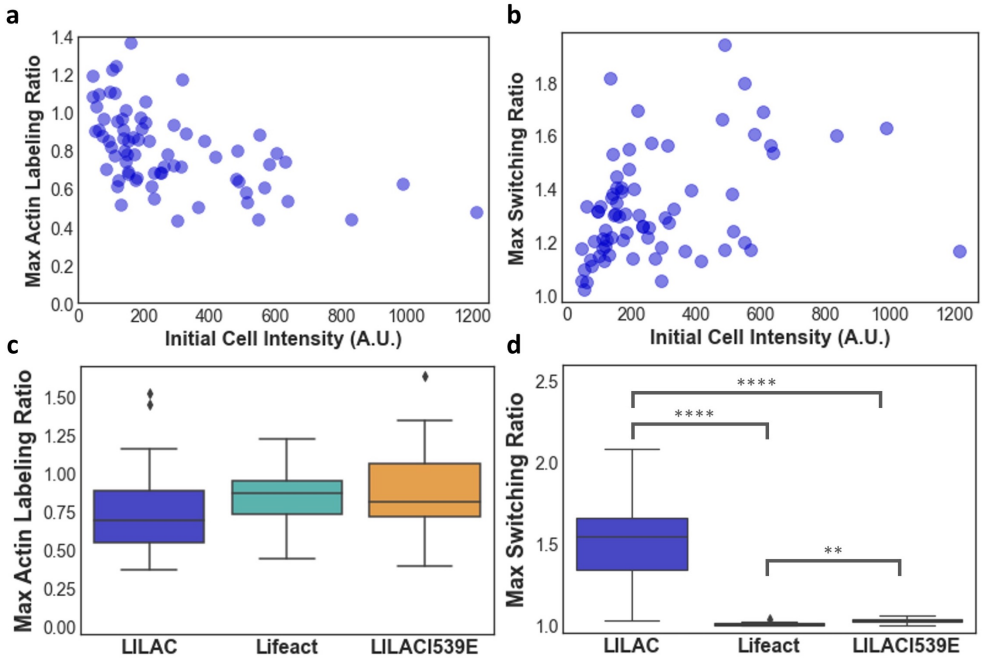

Figure 3.9: Quantification of labeling and switching of LILAC. Max actin labeling ratio (a, $R^2 = 0.27, P = 2.3 * 10^{-6}, n = 72$) and switching ratio (b, $R^2 = 0.13, P = 1.3 * 10^{-3}, n = 72$) of LILAC-expressing cells as a function of cell intensity. Maximum actin labeling (c, $P = 0.11$) and switching ratios (d, $P = 9.66 * 10^{-15}$) of LILAC, Lifeact, and the light-mimic mutant, LILACI539E. The center line represents the median. Boxes span the 25th and 75th percentiles. Whiskers extend from the 25th percentile - 1.5x the interquartile range (IQR) and from the 75th percentile + 1.5x IQR. Data beyond the whiskers represent outliers and are plotted individually. For c and d, P values were determined initially using a one-way ANOVA test ($n = 32$ for Lifeact, $n = 18$ for LILAC, $n = 23$ for LILACI539E). A post-hoc Dunn test was used to determine pairwise P values (LILAC-Lifeact: $P = 1.7 * 10^{-15}$, LILAC-LILACI593E: $P = 1.4 * 10^{-5}$, Lifeact-LILACI593E: $P = 2.4 * 10^{-3}$) ($** = P \leq 0.01, *** = P \leq 0.001, **** = P \leq 0.0001$).

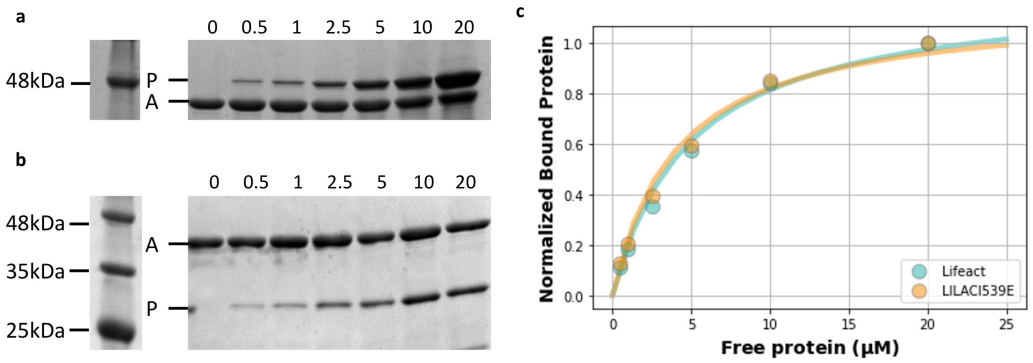

Figure 3.10: Binding of Lifeact and LILAC to F-actin. a,b, SDS-PAGE of the protein of interest (P), either mCherry- LILACI539E (a) or mCherry-Lifeact (b), in the pellet after co-sedimentation with 0.5 µM actin (A). Concentration of free protein added to each lane is labeled above in µM. c, Free protein plotted against bound protein in the pellet after co-sedimentation to determined binding affinities of Lifeact (K_d=3.9 µM) and LILAC539E (K_d=3.4 µM). Data were normalized to the maximum observed and fitted to a hyperbola. The constitutively active form of LILAC was used because excitation of LILAC cannot be maintained in the dark ultracentrifuge.

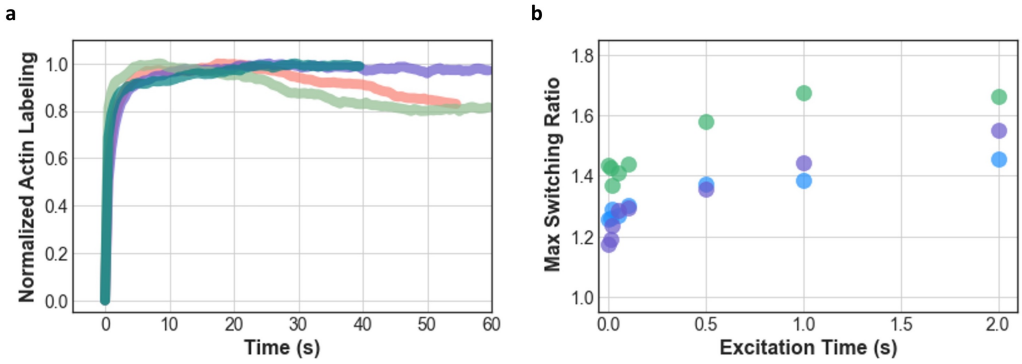

Figure 3.11: LILAC excitation dynamics. a, Min-max normalized actin labeling ratio traces for cells initially in the dark, then activated with blue light continually through the end of the movie. b, Max switching ratios for cells excited for various lengths of time at 1% laser power, colored by cell.

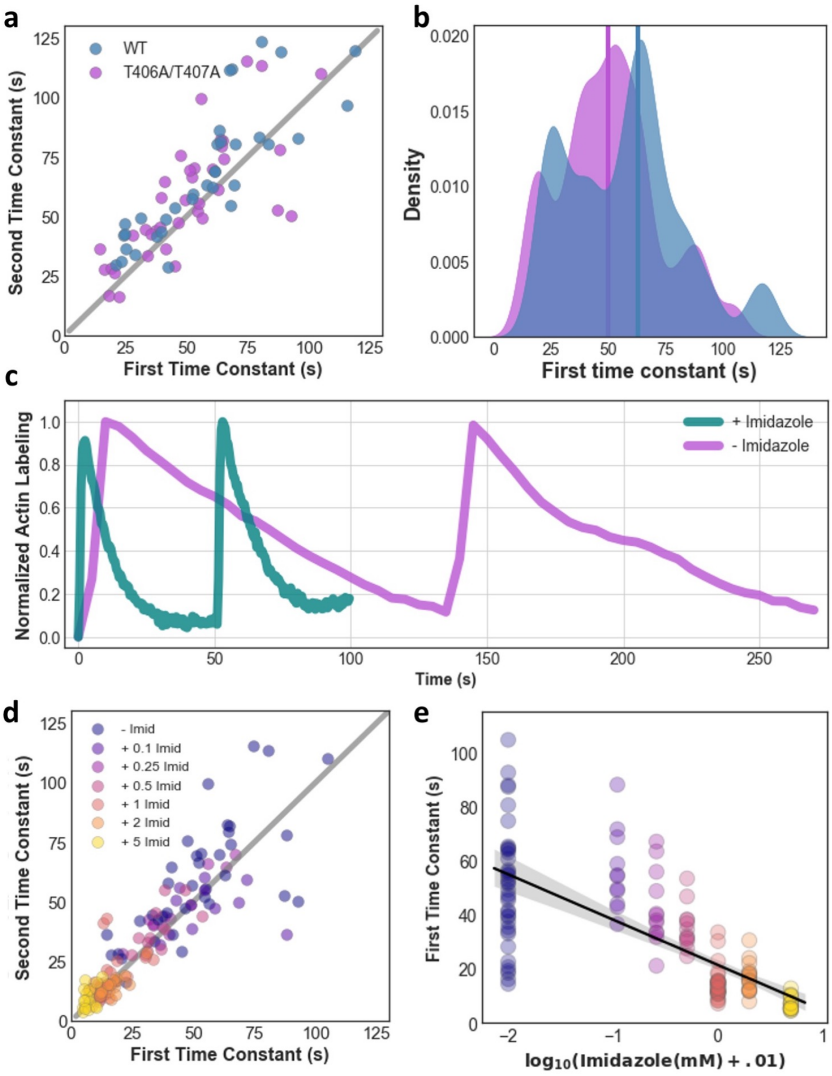

Figure 3.12: Dark state recovery time constants are cell specific and tunable. a, First and second recovery time constants for individual cells expressing wild type ($R^2 = 0.70, n = 34$) and T406A/T407A ($R^2 = 0.56, n = 26$) LILAC. Gray line is X = Y. b, Kernel density estimations of the first time constants for wild type (blue) and T406A/T407A (lilac) LILAC. Mean is indicated by vertical lines. c, Min-max normalized actin labeling ratio traces of LILAC(T406A/T407A)expressing cells with (teal) and without (lilac) 1 mM imidazole. Cells were activated with blue light every 60 and 130 seconds respectively. d, First and second recovery time constants for individual cells expressing LILAC(T406A/T407A) with varying imidazole concentrations ($R^2 = 0.77, n = 128$, Pearson $P = 7.3 * 10^{-46}$). Gray line is X = Y. e, First recovery time constants as a function of imidazole concentration ($R^2 = 0.52$, Pearson $P = 3.5 * 10^{-24}$) with a linear regression fit to log-transformed data and shaded regions indicating the 95% confidence interval. Data with 0 and 1 mM imidazole were taken at different times with different starter cultures of S2 cells than all other concentrations, which were imaged on the same day.

CHAPTER 4

SPATIOTEMPORAL ILLUMINATION OF LILAC

4.1 Spatiotemporal activation of optogenetics

Optogenetics is a particularly powerful tool due to the ease of spatiotemporal control of light. With most methods for modulating protein function, one must choose between spatial and temporal control. For spatial control, we can use promoter systems that express a protein of interest (POI) in specific cell types. Other common methods include siRNAs and microinjection which change protein levels but at relatively slow time scales. Cells must take up the genetic material and use protein expression machinery, which takes on the order of hours depending on the system. Faster alteration can be achieved using the addition of drugs. However, this often has little spatial control, especially in regards to subcellular structure. Some of these methods, do have some level of both spatial and temporal control, but none are as fast, highly resolved, and easy to use as light. What makes optogenetics so remarkable, is that we can control light on the micron and millisecond and sub-micron scale with ease, allowing for unparalleled spatiotemporal control.

4.2 Spatiotemporal illumination of LILAC in cells

Previous work with other optogenetic tools includes induced cell movement, amplification of filopodia generation for limb regeneration, microtubule disassembly, and more [Izquierdo et al., 2018, Cavanaugh et al., 2020, Ruijgrok et al., 2021, Meiring et al., 2022, Oakes et al., 2017, Hughes and Lawrence, 2014, He et al., 2021]. For example, CRY2olig motors, which induce filopodia, formation elucidated the role of filopodia in axolotl limb regeneration. Researchers exposed the regenerating limbs expressing the optogenetic motors to either light or dark observed limb morphology over time [Ruijgrok et al., 2021]. Stone et al. [2019] developed a cofilin-Z-lock construct to subcellular activate cofilin, an actin disassembly protein.

Z-lock blocks the cofilin active site with the LOV2-Zdk interaction, but upon illumination, the disassociate and free cofilin for activity. By illuminating an outer region of the cell, cofilin was locally active, promoting actin remodeling and invadopodia formation. With this technology, researchers can drive cells around towards the light. Similarly, Cavanaugh et al. [2020] induced local cellular contractions at cell-cell junctions using the TULIPs system to subcellularly activate RhoA [Strickland et al., 2012]. In these examples, the specific place and time of activation is critical for understanding the underlying biology. With this in mind, we wanted to investigate if LILAC could be used in a spatiotemporal manner in live cells.

Patterned illumination of LILAC has myriad potential uses both in a cellular context and in vitro. For example, if a cofilin-LILAC chimera could be subcellularly recruited to actin structures of interest, it would promote actin filament disassembly within illuminated areas. As a proof of concept, we subcellularly illuminated LILAC to determine the efficacy of such an illumination system. We also posited that subcellular illumination could further reduce toxicity of Lifeact, and potentially lead to insights about diffusion and kinetics in the cellular milieu. LILAC molecules illuminated in the area of activation have the potential to remain active and travel outside of the activation area and label actin elsewhere. This distance traveled by activated LILAC would theoretically depend on Lifeact-actin binding kinetics and intracellular diffusion rates. For example, the border between illuminated and non-illuminated areas should appear sharper if diffusion and Lifeact off rates are slow.

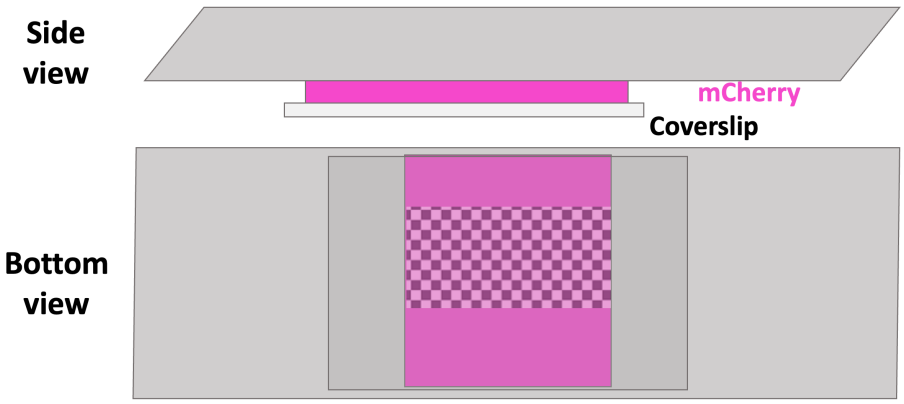

Figure 4.1: Schematic of the sample used for projector calibration. A sample of mCherry is placed between the slide and coverslip, and illuminated here, in a checkered pattern.

4.2.1 Projector setup and alignment

The in-house built TIRF microscope was modified to allow for sub-micron patterning and illumination. Lenses were removed from a video projector to focus the emitted image to infinity. A beamsplitter cube was used to join the projector image with the excitation laser line. Then, a projector plugin was installed to allow for control of the projector illumination with MicroManager.

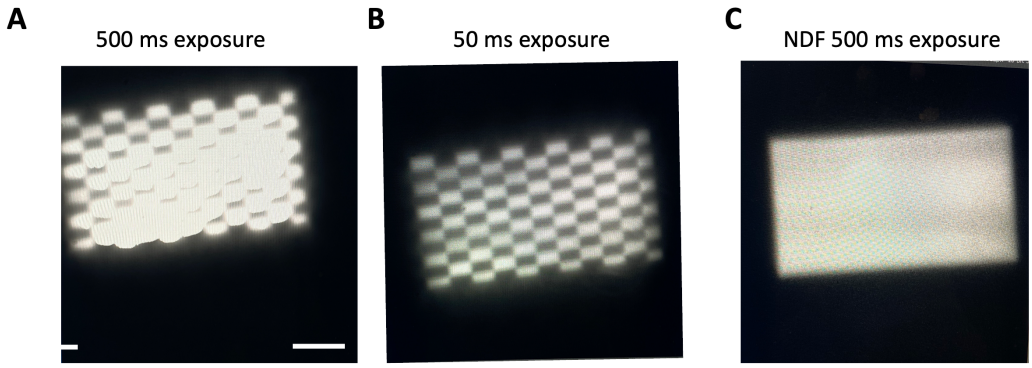

Figure 4.2: Addition of a neutral density filter (NDF) allows for extended exposure time. (a) Without an NDF, the exposure time needed for live-cell imaging results in a highly over-exposed image. However, the 50 ms exposure time allows for crisp visualization of the checkered pattern. (c) With an NDF, the entire projector could be illuminated without overexposure. Scale bar is 5 µm.

To confirm that the projector was aligned properly, we used an mCherry sample and monitored the emitted image, in this example a a checkered pattern, through an mCherry-specific filter (Figure 4.1). An exposure time of 500 ms was chosen, as that is the setting I used for imaging LILAC in S2 cells. However, at 500 ms of exposure, the image was overexposed. This was avoided by using 50 ms exposure times, but warranted another solution for longer time scale imaging (Figure 4.2). We solved this issue by inserting a neutral density filter in front of the projector in order to reduce the projector image intensity. Our filter mount was useful in that it contains two slots, and we have a variety of neutral density filters that can be used in various combinations to create the desired projector intensity. Additionally, the projector plugin allows for illumination of areas highlighted as regions-of-interest in ImageJ. Although this function worked some of the time, it was very sensitive to the calibration and often illuminated areas not in the ROI (Figure 4.3). We continued with the setup as is, making sure to keep in mind the calibration limitations.

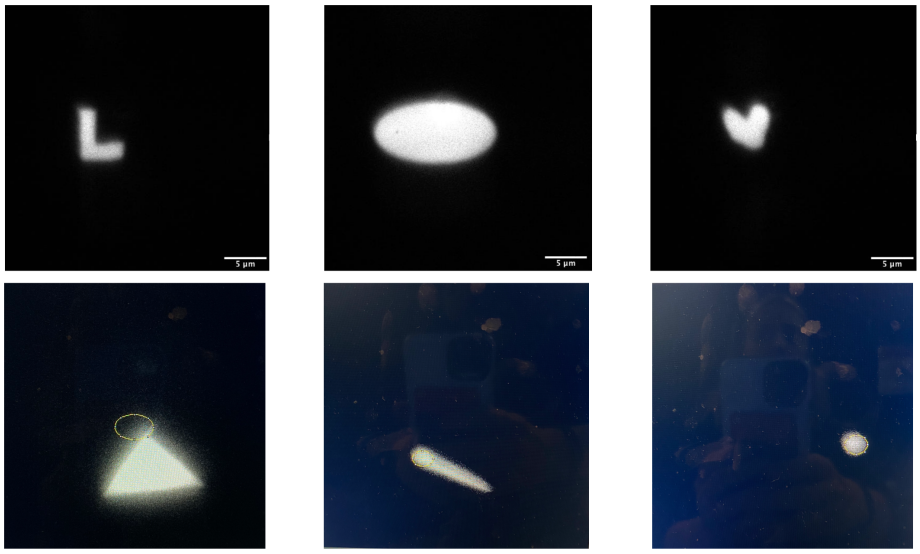

Figure 4.3: Illumination of regions of interest with a projector using TIRF. The projector plugin could be used to illuminate custom regions of interest successful (top). If the calibration was not working, some areas would illuminate outside of the illuminated ROI (yellow, bottom).

4.2.2 Subcellular illumination of LILAC

In an effort to reduce actin labeling outside of the excitation area, we sped up the photocycle by using the LOV2Q513D mutation, which has an in vitro recovery time constant of just 5 seconds, as well as 1mM imidazole [Zayner and Sosnick, 2014]. We posited that LILAC molecules excited in the ROI travel outside of the ROI through diffusion. The sooner LILAC recovers, the less distance it can travel from the ROI whilst activated. Additionally, quick LILAC recovery allows for faster imaging so data can be acquired per day. To determine if LILAC was activating locally, we first excited using the original protocol of excitation with the 488 nm blue laser (Supplementary Video 5). After allowing LILAC to reset for 20-30 seconds, we begin recording and after a few frames, turned on the projector to excite the ROI. For simplification, we began with exciting the entire ROI illuminated by the projector. To visualize this clearly, we subtracted both the pre-illumination image, and the image produced by exciting the ROI without cells in the field of view. With this procedure, we would be confident that if an area was brighter, this was due to changes in labeling, and not the background signal from the projector.

Activation with the projector resulted in increased actin labeling, but labeling did not appear greater in the ROI vs outside (Figure 4.4). The ROI used was large, so we repeated this with a smaller excitation area to see if this led to more clear subcellular recruitment. Reduced excitation area was achieved by placing an index card over half of the image emitted by the projector. However, even with a reduced excitation area, subcellular excitation was not obvious (Figure 4.5). We attempted to illuminate low diffusion areas, such as the lamellipodia, and high diffusion areas, such as the cell interior. However, in low diffusion areas, there is not enough LILAC to label actin structures, and in high diffusion areas, excited LILAC diffuses and label actin throughout the cell. This finding is copacetic, given that diffusion on the length scale of a cell is in milliseconds, while recovery kinetics are on the order of seconds.

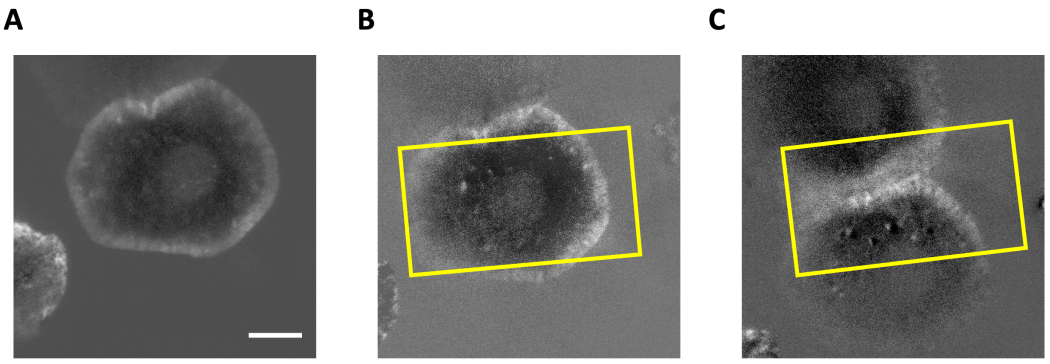

Figure 4.4: Illumination of a large ROI in S2 cells. (a) Pre-excitation subtraction image of an S2 cell illuminated in the entire ROI. (b,c) Pre-excitation subtraction image of the same cell illuminated in the ROI indicated in yellow. In (b) and (c), the projector signal was also subtracted from the image.

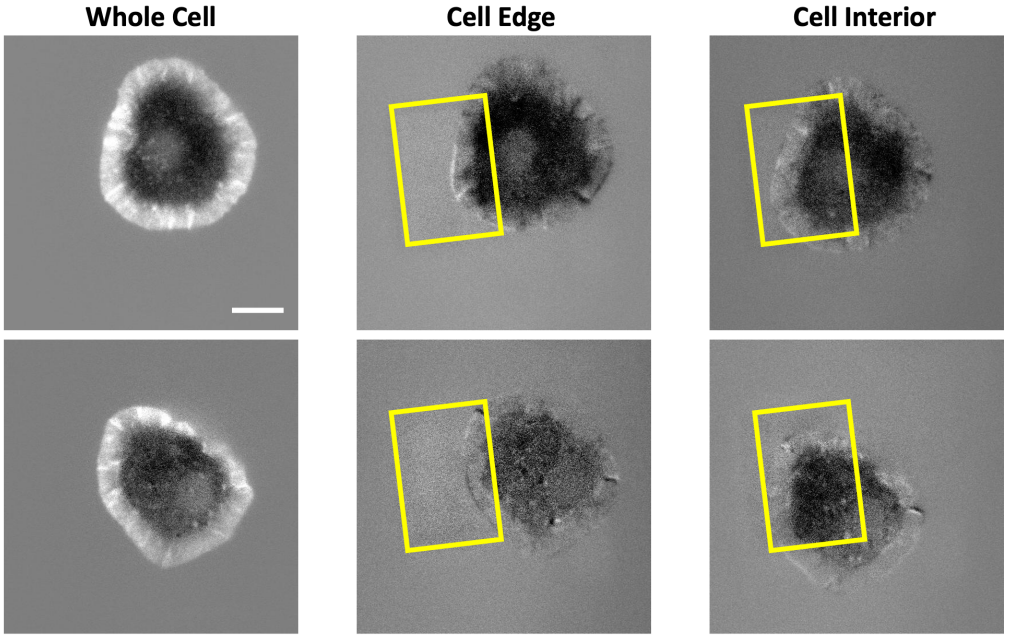

Figure 4.5: Illumination of a small ROI in S2 cells. Pre-excitation subtraction image of an S2 cell illuminated in the entire ROI (left). Pre-excitation subtraction image of the same cell illuminated in the ROI indicated in yellow on either the cell edge (middle) or interior (right). On the left and right, the projector signal was also subtracted from the image.

Unfortunately, subcellular labeling of actin with free LILAC does not seem to be possible, in contrast to successful subcellular recruitment with other optogenetic tools. These other optogenetic tools nearly always rely on membrane-anchored segments, thus substantially reducing the effects of diffusion of excited molecules and recruitment outside of the activated area. The only example of subcellular activation with a non-membrane bound system is opto-katanin [Meiring et al., 2022]. Opto-katanin is unique in that it contains two optogenetic units, a VVD dimerization system for recruitment to microtubules, and an iLID system for recruitment of the catalytic p60 domain. This reduces the dark state binding, as it requires both optogenetic tools to be on for activity. Thus, this likely works despite non being membrane-bound because only one of the two photosenstive domains needs to recover to reduce activity outside of the region of interest. In the future, a membrane-anchored LILAC could potentially subcellularly recruit actin filaments to the membrane with more success. We also could engineer a second photosenstive domain using the opto-katanin model, to reduce activity outside of the illumination area.

4.3 Spatiotemporal patterning of actin with LILAC

4.3.1 Actin patterning methods

Next, we shifted focus to patterning actin with LILAC. We hoped that this would work since by keeping LILAC fixed to a surface, it cannot diffuse, eliminating the issues with subcellular excitation of LILAC. We were motivated to pattern actin filaments in vitro to understand the influence of spatiotemporal dynamics on the interactions of actin and its associated binding proteins. Actin structures in the cells form dynamically in concert with the plethora of actin binding proteins in the cellular milieu including, bundlers, crosslinkers, motors, assembly and disassembly factors, and more. To understand how these parts coalesce, researchers purify actin and its associated proteins and examine their interactions *in vitro*. However,

the spatial organization of actin filaments likely plays a role in how cytoskeletal proteins interact with each other and actin itself. Currently, the most popular way to recapitulate the spatial organization of actin filaments is to micropattern actin nucleation factors, such as pWa [Reymann et al., 2012, Gressin et al., 2015, Letort et al., 2015, Reymann et al., 2010]. The limitations of this approach are that patterns must be pre-established, and that temporal control is not possible. Optogenetics have been applied to pattern microtubules (MTs) [Tas et al., 2018]. LOVpep (of the TULIPs famil)y was fixed to glass, and ePDZ was attached to kinesin, a microtubule motor. Upon light activation, kinesin molecules bound to MTs was recruited to the surface, leading to both MT recruitment and movement by the kinesin motor. In a similar vein, LOVdab, an optogenetic cargo binding domain for myosin, an actin motor, was used to recruit actin filaments to the surface with light [French et al., 2017]. The limit to this approach was that it was not reversible; once recruited, filaments never released. Importantly, both of these system require the expression and purification of molecular motors kinesin and myosin, which are very large and require intensive methods for clean purification of significant amounts of protein. We hoped that LILAC could recruit actin reversibly with a design that is easier to produce.

4.3.2 Fluorescent protein selection

As described previously, we tagged LILAC with a 6xHis tag for purification, as well as an mCherry for fluorescence. MCherry is excited by green (561 nm) light, which allows for independent excitation of LILAC (488 nm) and mCherry (561 nm) with common laser colors. The mCherry tag is not necessary in this assay, as the LILAC should remains fixed to the glass; however, it is still beneficial to keep this tag for a number of reasons. First, protein purification with nickel columns is much easier with a FP. The column turns bright pink when the protein attaches, and the elution is also bright pink. Therefore, it is clear where the protein of interest (POI) is at all times. Also, after LILAC is attached to glass,

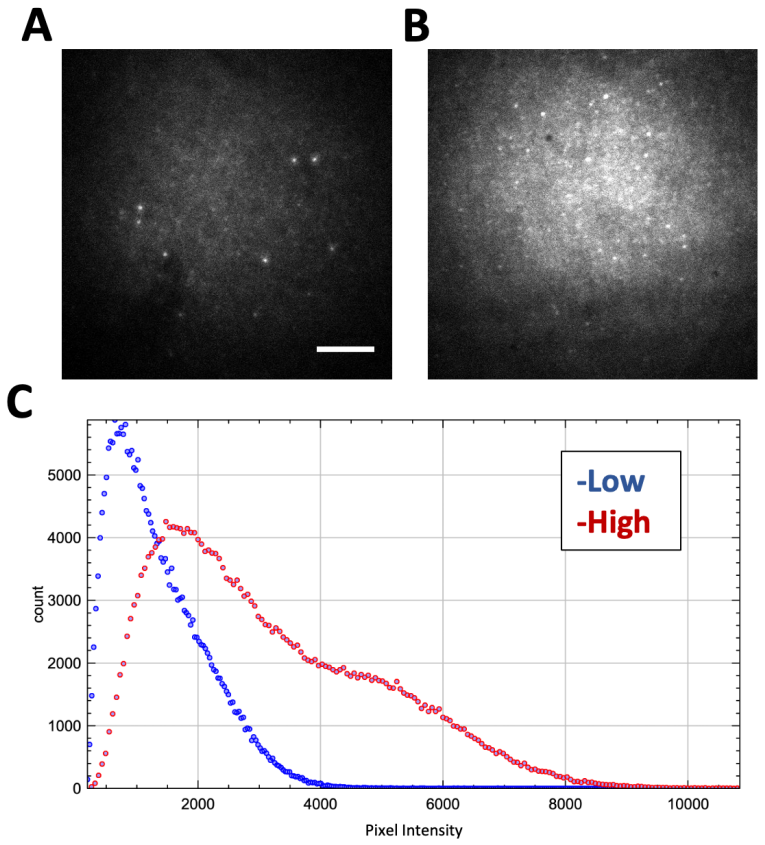

Figure 4.6: Distribution of mCherry-LILAC on functionalized glass. TIRF images of mCherry-LILAC at low (a) and high (b) concentrations. (c) Histograms of pixel intensities in the above images.

the mCherry can be imaged to estimate the relative concentration of LILAC on the glass, as well as the distribution of molecules (Figure 4.6). Bright puncta can also be seen, likely due to the weak oligimerizaiton tendency of mCherry. To visualize actin we needed an even further red-shifted fluorophore so as to not interfere with LILAC or mCherry. Accordingly, we chose an Alexa 647 nm phalloidin to label and stabilize actin filaments.

4.3.3 Imaging method

Conventional widefield fluorescence microscopy illuminates the entire sample, and the illumination beam passes through the entire sample (Figure 4.7a). In contrast, total internal fluorescence (TIRM) micropscopy selectively illuminates only a thin layer close to the glass

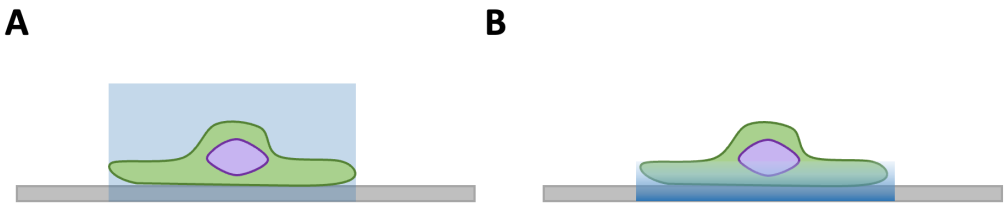

Figure 4.7: Schematic of widefield and TIRF illumination. (a) Schematic of widefield microscopy, where the entire sample is illuminated. (b) Schematic of total internal fluorescence (TIRF) microscopy, where an evanescent wave illuminates a thin layer of the sample close to the glass.

with an evanescent wave (Figure 4.7b). In comparison to widefield, TIRF microscopy has increased resolution and contrast for cellular structures that are near the surface. TIRF is also useful for single molecule imaging of molecules that are near the surface. For actin pattern with LILAC, TIRF is the ideal microscopy technique as we can visualize specifically when actin molecules are close to the glass surface. Therefore, when we see actin filaments in focus with TIRF, we can be confident that they are bound to the surface and not floating in solution above the glass. By monitor the change in actin binding to the surface with and without blue light, we can assess LILAC's ability to pattern actin.

4.3.4 Protein fixation methods

In order to pattern actin with LILAC, we must attach LILAC to a glass surface. There are a number of ways to attach proteins to glass. First, we attempted to stick LILAC onto nitrocellulose-covered glass. This is a common method for creating a non-specifically sticky surface. LILAC was then flowed over the surface allowing it to bind to the surface. To create a flow chamber, we placed two thin pieces of double sided tape onto a slide about 5mm apart and then placed the coverslip on top. It is important to place the functionalized side of the glass down to the inside of the chamber. Then, excess LILAC is washed off, and bovine serum albumin (BSA) is added to bind any exposed area of the nitrocellulose covered glass.

This extra step is important, as when the actin filaments flow over, they must only stick to the glass through binding to LILAC, not through nonspecific binding to the sticky glass. However, with this method, we did not observe any differential binding of actin filaments to the surface with blue light. Possibly with a nonspecific surface, LILAC sticks to the glass in an orientation that occludes binding. Therefore, we decided to try other glass surfaces which specifically orient LILAC.

We then shifted to surfaces that are functionalized for specific binding. Our first attempt was using supported lipid bilayers (SLPs) [Nye and Groves, 2008]. These bilayers were created by filtering vesicles repeatedly until they were very small, then placing them on a surface so that they spread. SLPs can contain lipids with nickel head groups that bind to His-tagged proteins. Nickel binding is convenient for both specificity, and for orienting the molecule. With the His-tag at the N-terminus, the C-terminus of LILAC is free to bind actin. Unfortunately, we found that the SLPs were inconsistent, time consuming, patchy, and did not result in a functional assay.

Our next attempt was using a biotin-avidin system (Figure 4.8). This requires biotinylating LlLAC, which was achieved with an aviTag [Fairhead and Howarth, 2015a]. A small peptide sequence is incorporated into the construct and biotynylated at a specific residue in the sequence. When an aviTagged protein is expressed in cells co-expressing the BirA enzyme, it is biotynlated as it is produced in the cells before purification. With this setup, we began with plasma-cleaned glass. Then, we added biotinylated (BSA), followed by Beta-casein for blocking. We then added neutravidin to bind to the biotin on BSA. LILAC was then flowed into the flow chamber and is fixed to the glass through the connection to neutravidin. Finally, far-red actin is added with an oxygen scavenging system to reduce photobleaching. In the end, LILAC was fixed to the glass with its C-terminus, which contained Lifeact, oriented towards the solution containing labeled actin.

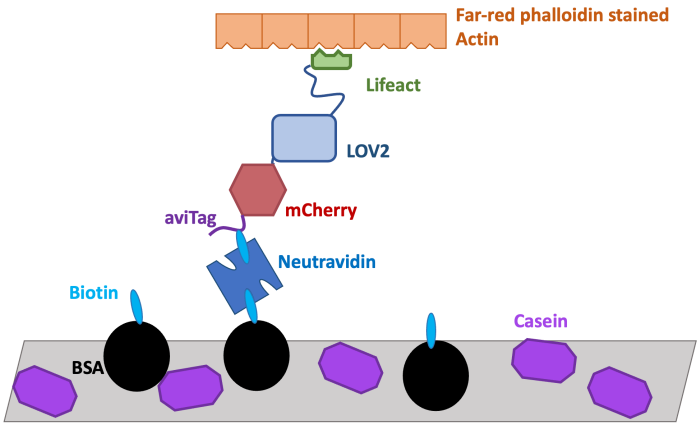

Figure 4.8: Schematic of the surface for in vitro actin patterning. First, the surface is coated with biotinylated bovine serum albumin (BSA). Then, casein is added to block nonspecific binding to the surface. Next, neutravidin is added to bind to the biotinylated BSA. mCherry-LILAC is biotinylated with the aviTag system, and attached to free binding sites on neutravidin. Finally, actin stained with far-red phalloidin in flowed over in assay buffer and an oxygen scavenging system.

4.3.5 Results

We found that the first time we attempted to pattern actin, the actin filaments seemed to bump into the surface without binding in the light or the dark (Supplementary Video 6, Figure 4.9). We thought that this could be due to a non-functional LILAC, but upon further consideration, realized it could be due to buffer conditions. The standard assay buffer contains 25 mM imidazole, which greatly reduces the recovery time of LOV2. Therefore, we hypothesized that LILAC was being activated, but was very quickly returning to the dark state.

Logically, we next repeated the experiment in the absence of imidazole. With these conditions, we were able to recruit actin filaments to the surface with blue light (Supplementary Video 7, Figure 4.10). The filaments seemed to rain down and irreversibly stick to the surface. Unfortunately, there was also binding of some filaments in the dark as well. The release of filaments requires each bound LILAC molecules to revert to the dark state and release the actin subunit. Thus, recovery time, filament length, and LILAC concentration are all factors

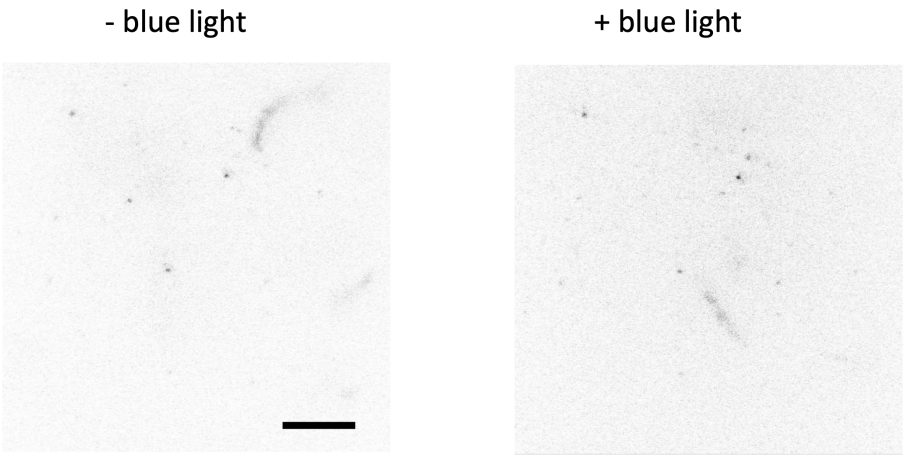

Figure 4.9: LILAC does not recruit filaments in 25 mM imidazole. Representative TIRF images of actin filaments in 25 mM imidazole assay buffer. The filaments bounce off the LILAC on the surface of the glass in both the light and dark. Scale bar is 5 µm.

that can determine the release of actin filaments. Faced with the opposing problem to our previous issue, we decided to titrate imidazole, hoping that there would be a Goldilocks's concentration where LILAC is activated long enough to recruit filaments, but not so long that filaments do not release in the dark.

As imidazole concentration increased, we observed reduced dark state filament binding (Figure 4.11). We also noted that filaments begin to wiggle when returning to the dark (Supplementary Video 8). This implies that segments of the filaments are releasing, but they are trapped at the surface by remaining bound segments. It also implies that reducing the recovery time does aid in the release of filaments. However, we still did not observe sufficient filament release, so we decided to work with smaller actin filaments and reduced LILAC concentration at the surface. Shorter actin filaments were created by shearing them with a pipette against the edge of a microfuge tube. We also reduced the concentration of LILAC on the surface by flowing less LILAC into the chamber. The mCherry signal was lower, confirming that we had less LILAC on the surface. With 6mM imidazole, shorter actin filaments and less LILAC, nearly all filaments quickly release from the slide (Supplementary Video 9, Figure 4.12). Occasionally longer filaments remained, confirming that filament

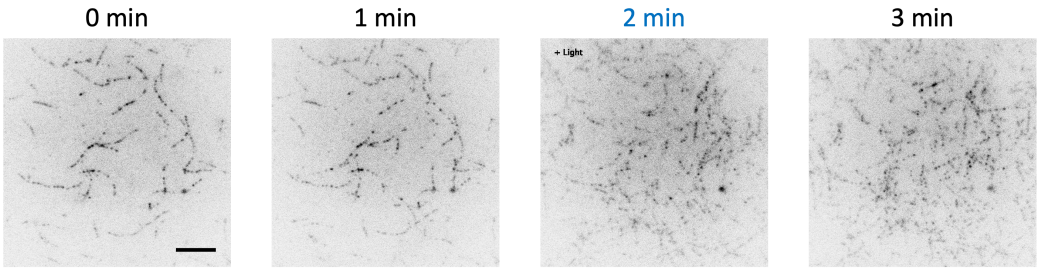

Figure 4.10: LILAC irreversibly not recruits filaments in 0 mM imidazole. Representative TIRF images of actin filaments in 0mM imidazole assay buffer. Some filaments are bound in the dark between 0 and 1 minute, but not many more filaments accrew in that time. Between 1 and 2 minutes, blue light excites LILAC on the surface and filaments recruit to the surface. Between 2 and 3 minutes, the blue light is turned off, but filaments do not release from the surface. Scale bar is 5 µm.

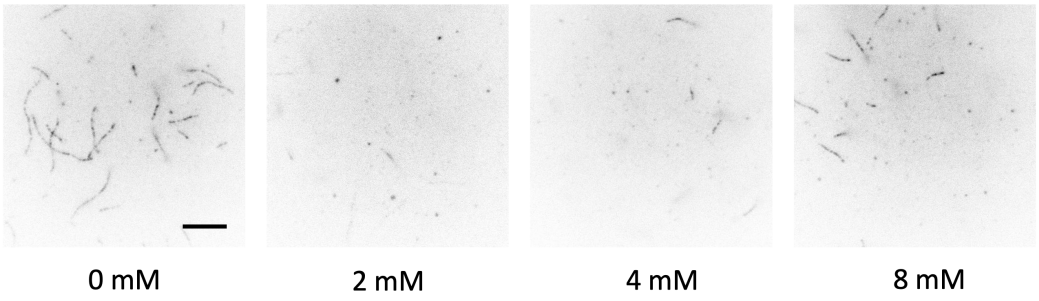

Figure 4.11: Imidazole reduces dark state binding of actin to LILAC. TIRF images of actin filaments on the surface of LILAC-coated glass in the dark. As imidazole increases, filaments stick to the glass less. Scale bar is 5 µm.

length is a factor in release time. The recruitment and release of filaments was quantified, and release time constants averaged 19 and 28 seconds for various quantification methods (Figure 4.13.

With reversible filament recruitment working, we wanted to tweak earlier experiments to reversibly recruit longer filaments. By drastically reducing LILAC concentration (10x) and adding 6mM imidazole, many long filaments released within minutes (Supplementary Video 10). With longer filaments, the sequential landing and release of filaments can be observed. This is easily visualized using kymographs (Figure 4.14). In the two examples shown, filaments first land at one end, and then zip up along the rest of the filament onto

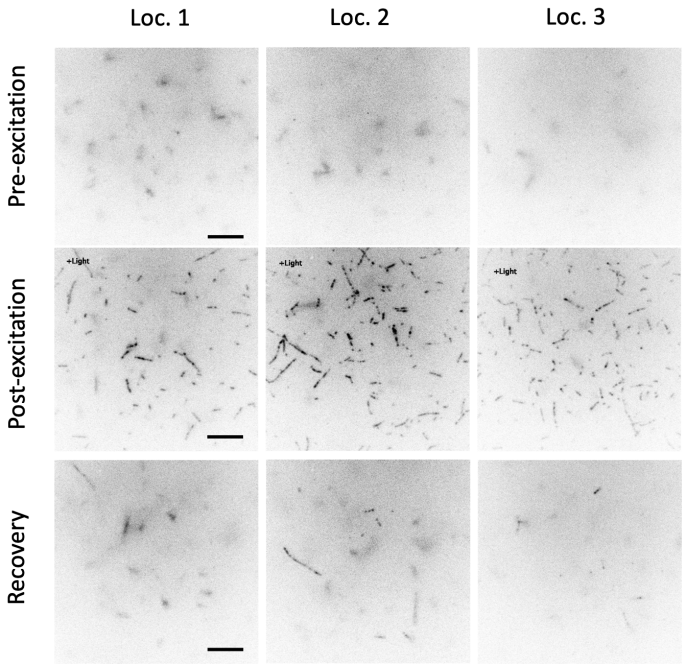

Figure 4.12: Recruitment of filaments is reversible with ideal conditions. TIRF images of sheared actin filaments reversibly recruited to a LILAC-coated glass surface at three locations on the surface. Images are taken with 6mM imidazole, and 0.2 mg/ml of LILAC added to the glass. Scale bar is 5 µm.

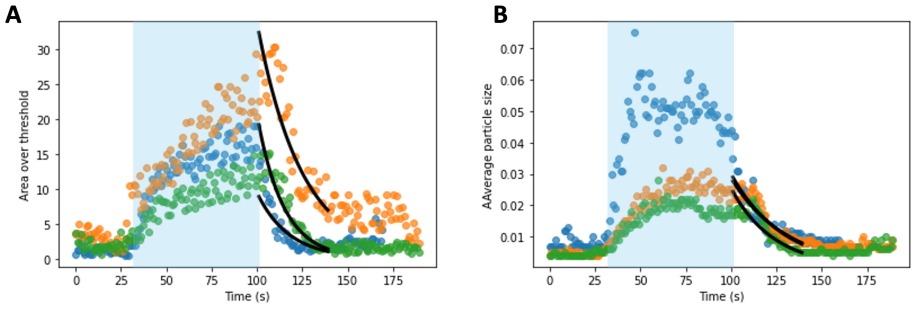

Figure 4.13: Quantification of actin filament recruitment. For three cells, shown in orange, green, and blue, LILAC was activated with light between from t=30 seconds to t=100 seconds. Filament recruitment was quantified using both the average area over a threshold pixel value (a), or the average particle size over a threshold pixel value (b). Using the first method, the average release time constant is 19 seconds, and using the second method it is 28 seconds.

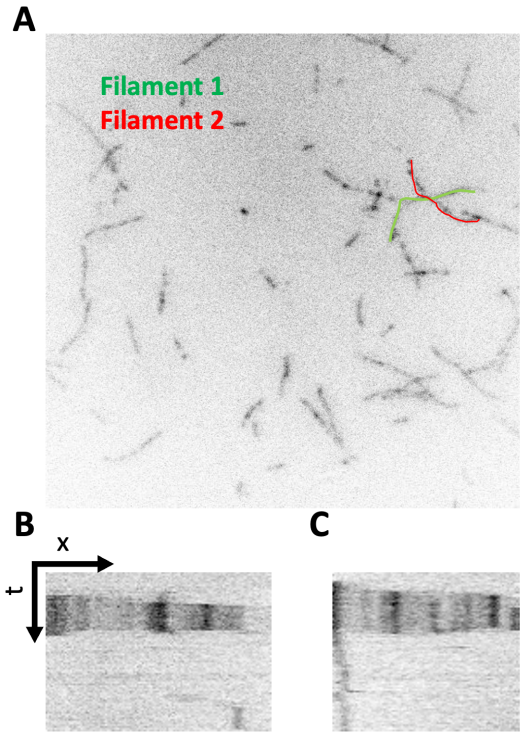

Figure 4.14: Kymographs of filament landing and release. (a) Filaments used for kymograph creation in (b,c). (b,c) Kymographs of filaments 1 and 2 landing and releasing from the LILAC surface. The horizontal axis is x, and vertical axis is time. (b) The filament releases from the center first, anchored by the endpoints. (c) The filament releases from the edges first, anchored by the center.

the glass. The release mechanisms are different, however. Filament 1 first releases from the center, with its two ends as anchor point, while filament 2 first releases on the ends with the center as its anchor point (Figure 4.14b,c). In conclusion, LILAC and imidazole concentrations should be optimized depending on the filament length and desired release time.

Now that we had a functional recruitment system with LILAC, our next goal was to pattern actin onto specific regions of interest (ROI) within the field of view. We used the same projector illumination setup that was used for cells discussed previously. As before, we needed to adjust the projector intensity such that it was bright enough to excite LILAC, but not so bright that the projector signal overpowered the actin signal. We found that the

dual neutral density filter holder did not give sufficient options given our number of filters that fit into the holder, so we switched to a dual neutral density filter wheel, allowing for even easier adjustment of projector intensity.

We began by illuminating the entire projector ROI. This resulted in successful recruitment of filaments into the area. However, the ROI was large, and we wanted to see if we could more precisely pattern filaments. As we did earlier, we placed an index card over part of the projector beam to reduce the illumination area. We found that filaments precisely recruited to the illuminated area, which we visualized by subtracted the pre-excitation from post-excitation image (Figure 4.15a). This recruitment increases over time (Figure 4.15b). We also quantified this recruitment and found that filaments recruit more inside the illumination area versus outside (Figure 4.15c). It is notable that we found recruitment slower with the projector illumination than with the full field-of-view laser illumination, likely due to the differences in illumination intensity. Because the projector is a more broad spectrum illumination, it should be set to a lower intensity to image actin, to reduce the projector signal that leaks into the Alexa-647 emission channel.

With a functional patterning method, we next tested if LILAC could be frozen after purification. Previously, we used freshly purified LILAC, which begins to degrade around 5 days after purification. Degradation is clear through an increase in dark state binding of filaments as well as an increase in puncta in the mCherry channel. This is inconvenient for those looking to use LILAC as a part of more complex assays. We froze freshly dialyzed protein in both the -20 C and -80 C freezers. The -80 C frozen protein showed minimal clumping and dark state binding, and retained reversible recruitment of filaments. Additionally, we spun the thawed sample at 15,000xg for 2 minutes to sediment the clumps we saw in imaging. This step reduced the clumps and dark state binding. We also made new actin filaments which were longer than previously, and obtained movies of filaments up to 20 µm long landing and releasing from the surface (Supplementary Video 11, Figure 4.16).

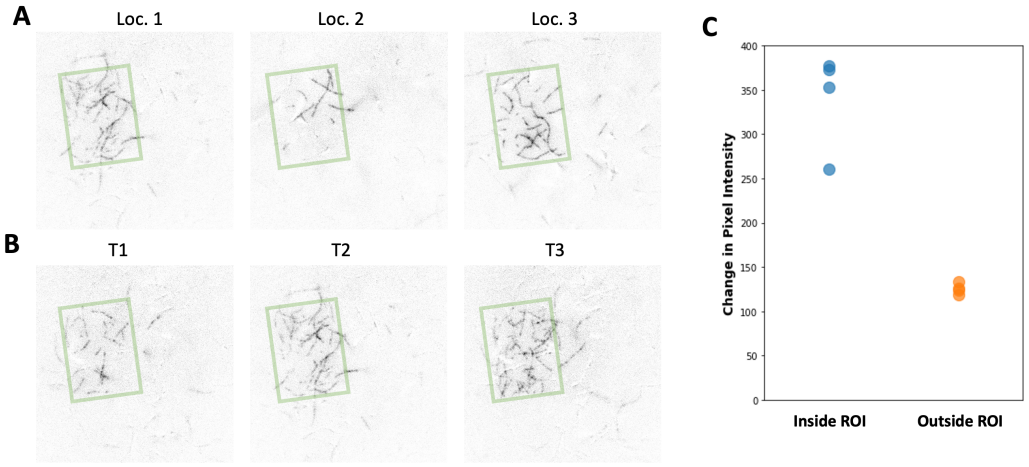

Figure 4.15: LILAC-coated glass patterns actin filaments with light. (a) Pre-post illumination subtraction images at three separate locations. The area inside the green box is illuminated. (b) Pre-post illumination subtraction images over three time points. Increasing length of time allows more filaments to recruit to the area. (c) Quantification of actin recruitment inside and outside of the illuminated region of interest (ROI).

Kymographs of the filaments over time show the variety in filament landing and release methods. Many land on one end and zip up to the other end, while others begin landing in the middle. When releasing, the partially stuck ends appear as fuzzy on the kymograph, since the unstuck ends of the filament are fluctuating in and out of the TIRF field. Overall, the fact that we can obtain such high quality images with thawed LILAC means that LILAC can be easily stored and thawed for use, making for a much more user-friendly system.

Next, we re-calibrated the projector, this time removing the NDFs so that the mCherry signal was bright. This improved the calibration significantly, and allowed for more precise illumination patterns. We even observed filaments that were stuck in the ROI, with the rest of the filament detached and wiggling outside of the ROI. Such a level of precision means that it is possible to do a large number of complex maneuvers with filaments, i.e. clamping down one half at a time to produce a stepping motion.

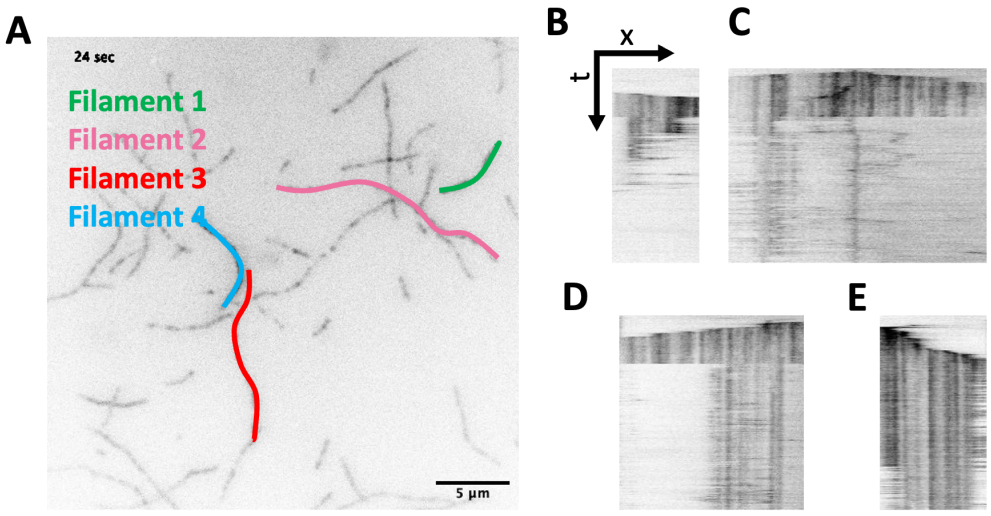

Figure 4.16: Kymographs of filament landing and release. (a) Filaments used for kymograph creation in (b-e). (b-e) Kymographs of filaments landing and releasing from the LILAC surface. The horizontal axis is x, and vertical axis is time. (b) The filament lands from left to right. Next, the edges release before the entire filament releases. (c) The filament lands from the center out. Then, the right half releases shortly before the left half. (d) The filament lands from right to left. The left half quickly releases and the right half remains. (e) Slowly, the filament lands from left to right. The edges of the filament release, first right then the left side.

4.3.6 Conclusions and future work

The foundational work of developing a system for spatiotemporal actin patterning has been completed. Next, creative light patterns should be explored to examine the limitations of just how much control we have over actin with LILAC. Future possibilities include: testing the limits of just how small of an illumination area we can use to precisely pattern single filaments, flashing a light gradients to move filaments from darker to lighter areas, recruiting filaments with particular spacing and observing the effects of cross-linkers, and more.

CHAPTER 5

CONCLUSIONS AND FUTURE WORK

With this work, I have demonstrated the methodology for designing a helical peptide-based optogenetic tool, as well as shown the utility of a light-sensitive actin-binding protein, LILAC. LILAC has two uses currently: as an imaging reagent with reduced morphological defects and novel imaging modes, and as an in vitro actin filament patterning tool. However, there are a vast array of potential applications of LILAC that can be harnessed to address new questions in biology.

5.1 LILAC in sensitive cell types

One aspect that I would have liked to explore more is the use of LILAC in various cell types. There are a number of cell types that are sensitive to Lifeact overexpression which could benefit from the use of LILAC instead. For example, I have heard from colleagues that neurons are particularly challenging. The cells are quite sensitive, and the use of Lifeact requires careful expression level calibration as a first step in many projects. I would be interested in looking at the ideal expression level of Lifeact and LILAC in parallel to see how much more LILAC can be tolerated. I would also be interested to see if LILAC needs less careful, if any, expression level calibration.

5.2 Spatiotemporal cross-linking

The spatial and temporal organization of the actin cytoskeleton is fundamental to cells, yet we currently do not understand the underlying principles of how these filaments self organize. Additionally, it is currently unknown exactly how ABPs recognize specific actin networks, despite many ABPs being well characterized biochemically. These questions could

be addressed by spatiotemporally using LILAC to cross link actin filaments with various interfilament distances to see if these bundlers cosegregate.

In cells, there are two main categories of bundled filaments: tightly packed parallel networks that make up filopodia and microvilli, and widely spaced, mixed polarity networks that make up stress fibers, sarcomeres, and cytokinetic rings [Blanchoin et al., 2014, Winkelman et al., 2016, Bartles, 2000, Michelot and Drubin, 2011, Kadzik et al., 2020, Jansen et al., 2011, Courson and Rock, 2010, Foley and Young, 2014, Ribeiro et al., 2014]. Despite the importance of cross-linkers to actin network structure and stiffness and their spatiotemporal complexity, the field lacks a spatiotemporally controllable cross-linker. I would use a Lifeact-Spectrin(X)-LILAC or "LAAX" chimera as a light-sensitive cross linking protein. With this tool, I would determine if ABPs use interfilament distance to differentiate actin structures. Winkelman et al. [2016] found that compact bundlers fimbrin, fascin, and espin cosegregate from alpha-actinin bundled filaments, suggesting that these proteins recognize interfilament distance. To test this hypothesis, I would image actin filaments as they cross-link with varying interfilament distances and observe if fascin/alpha-actinin recruit to tightly or loosely cross-linked filaments. My first step in creating the light-activated actin LAAX cross-linker would be to add an N-terminal Lifeact peptide to LILAC to anchor one side to a filament. Upon illumination, the second Lifeact peptide would uncage, allowing LAAX to bind two filaments (Figure 5.1). This should provide an interfilament distance of 6 nm, which is similar to the interfilament distance of fascin bundles. To increase the interfilament distance to the nearly 35 nm of alpha-actinin bundles, I could add spectrin repeats (Lifeact-SpectrinX-LILAC), which are 5 nm long (Figure 5.2). If fascin and alpha-actinin recognize interfilament distance, fascin would preferentially colocalize to light activated areas cross-linked with LAAX without spectrin repeats, while alpha-actinin would recruit to bundles made with LAAX with at least 6 spectrin repeats. By controlling interfilament distance at precise locations along a bundle, we could determine if ABPs detect this distance to control

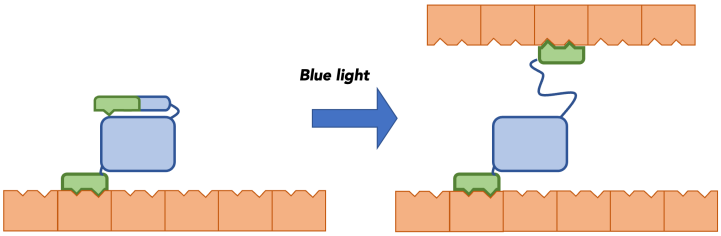

Figure 5.1: Schematic of LAAX. In the dark, the N-terminal Lifeact (green) binds to an actin subunit on a filament (orange). The blue LOV2 of LILAC blocks the second Lifeact from binding another filament. Upon excitation, LOV2 partially unfolds allowing the second Lifeact to cross-link and bind another actin filament.

their spatial patterning.

If LILAC re-caging is too fast or too slow, I could alter the refolding time with previously investigated LOV2 mutations/buffer conditions (range 10 sec to 20 min) [Zayner and Sosnick, 2014, Zayner et al., 2013]. For better visualization, I could label filaments at low concentration of phalloidin for a sparse labeling of filaments, which is necessary for high or super-resolution. When cross-linking filaments, it is possible that the filaments might slide parallel to each other, decreasing the interfilament distance. To reduce this, I would add an L-shaped kinked helix between the N-terminal Lifeact and LOV2. By increasing the rigidity between these subunits, sliding between filaments should be more difficult. The Kovar lab at the University of Chicago has successfully expressed fascin, espin, fimbrin, and alpha-actinin and can assist with plasmids and purification protocols. Other approaches include using other ABPs at the N-terminus of LAAX, such as utrophin or F-tractin [Burkel et al., 2007, Brehm et al., 2004].

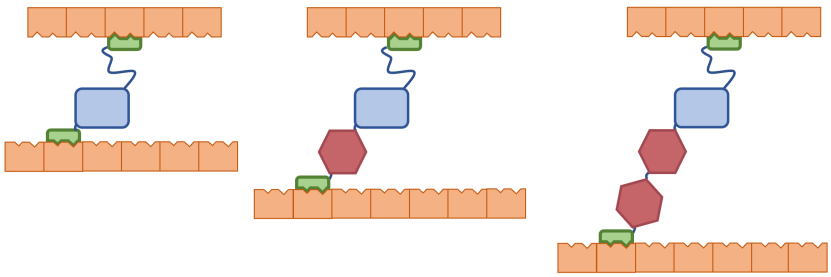

Figure 5.2: Schematic of LAAX with spectrin spacers. When LOV2 (blue) is excited, the N-terminal and C-terminal Lifeact peptides (green) bind to an actin subunit on a filament (orange). Addition of spectrin repeats (red) increases the interfilament distance.

5.3 Alteration of cardiomyocyte dynamics

The coordination of cardiomyocyte contraction in space and time is critical for successful beating of the heart. Therefore, optogenetic tools are an extremely useful method as one can express them in living cells and control them noninvasively with high spatiotemporal resolution. Two main causes of heart arrhythmia are channelopathies, genetic defects in ion channels, and cardiac infarction. Previous use of optogenetics to investigate channelopathies used opsin-based optogenetics [Beiert et al., 2014, Entcheva and Kay, 2021, Wang et al., 2017, Men et al., 2020, Abilez, 2012, Ambrosi et al., 2014]. These light-sensitive ion channels are useful for examining electrical activation and communication between cells and have been used as a less invasive alternative to electrical stimulation. Unlike previous cardiac optogenetics, LILAC could alter the physical, not electrical, properties of beating cardiomyocytes. This could allow us to understand how cardiac mechanotransduction affects cardiomyocyte beating.

During myocardial infarction, reduced blood flow decreases ATP in myocytes [Saleh and Ambrose, 2018, Doenst et al., 2013, Lyon et al., 2015]. Without ATP, cells lack energy for the myosin power stroke. Electrochemical signaling has been extensively studied in myocytes, while less focus has been on the effects of cell stiffening. Deformation triggers mechanotransduction signaling pathways including stretch-activated ion channels and changes in chemical gradients [Doenst et al., 2013, Lyon et al., 2015, Romito et al., 2017, Pasqualini et al., 2016]. Mechanotransduction allows cells to modulate cell stiffness in response to deformation. The extracellular matrix drives the passive biomechanical properties of the heart, while actin and myosin provide active contractile forces [Doenst et al., 2013, Lyon et al., 2015]. Therefore, spatiotemporal reduction of acto-myosin contraction could elucidate how infarction-induced stiffening alters beating dynamics.

To reduce the beating of HL-1 cardiomyocytes illuminated with blue light, I would transfect them with FP-LILAC. Because Lifeact has been shown to compete for binding with myosin through a shared actin binding site [Belyy et al., 2020, Kumari et al., 2020], by uncaging LILAC, I hope to reduce bound myosin, thus stalling beating. Fast Fourier transform (FFT) analysis of videos of beating cells has been previously used to quantify cardiomyocyte beating [Reno et al., 2018, Hossain et al., 2010, Bazan et al., 2011]. If my strategy is successful, the beating amplitude and/or frequency should reduce in the location where LILAC is excited.

Next, I would like to determine how mechanical force affects cardiomyocyte synchronization. Nitsan et al. [2016] showed that cardiomyocytes can be trained to synchronize with mechanical probes mimicking neighboring cells [Nitsan et al., 2016]. This effect lasts for an entire hour post stimulation, unlike electrical stimulation, suggesting long term effects of deformation. Additionally, actomyosin contractility was necessary for this process, but the spatiotemporal effect of actomyosin contractility was not explored [Nitsan et al., 2016, Cohen and Safran, 2018]. To address this, I would illuminate a group of cells with the intent

of stalling them in a ring of varying size and determine the size at which cells inside and outside the ring no longer beat synchronously through FFT video analysis. To investigate the effect of temporally modulating contractility, I would pulse the rings of light and examine synchronicity.

If inducing beating in HL-1 cardiomyocytes proves to be challenging, one could use iPSC derived cardiomyocytes, which have been shown to beat spontaneously [Pushp et al., 2020]. I would increase expression levels and illumination intensity if I find that LILAC is not reducing cell contraction. If the transfection efficiency is low, I would sort cells based on fluorescence intensity with flow cytometry and select LILAC expressing cells. To quantify beating dynamics, I can also image on a gel loaded with fluorescent beads, which has been extensively used in the Gardel lab, here at The University of Chicago.

5.4 Light-powered protein folding motor

Canonical motors like myosin or kinesin walk along filaments using ATP as an energy source [Hartman and Spudich, 2012]. This motion is accomplished by nucleotide state-dependent changes in binding affinities. The lever arm power stroke, or "step" is asymmetrical, leading to a direction bias, so over time there is net movement in one direction along the filament. The essence of this process is an energy cycle, states with different binding affinities, a step, and directional bias. Following this core parts list, LILAC could possibly perform as a motor that is powered directly by light, unlike all canonical motor proteins which rely on chemical energy (Figure 5.3). In the dark state, the AsLOV2's Jα remains folded so that Lifeact is caged and unable to bind actin. Upon blue light absorption, the Jα helix of AsLOV2 unfolds, which releases Lifeact to search and bind actin. In the next step, the Jα helix refolds and returns to the dark state, pulling on the actin filament. In the final step, the Lifeact unbinds and AsLOV2 relaxes back to its ground state where the Lifeact is caged so that when exposed to another light pulse, it can bind a new actin site. This motor thus uses

a light pulse train as an energy source, harnessing the unfolding of the Jα to cage Lifeact and create states with different binding affinities. LILAC accomplishes a step with the partial refolding of the Jα, and the anchoring of the N-terminal of the Jα causes Lifeact to diffuse to binding sites on the left in more than on the right in Figure 5.4. This process can also be viewed as a continuum ratchet, like those described by [Kolomeisky and Fisher, 2007] with varying energy surfaces and conformational probabilities depending on the light versus dark state. When bound at position n, LILAC can rotate. However, because the Lifeact peptide binds along the asymmetric filament, there is an inherent asymmetry. At each of the three rotational positions shown, the core is at a different distance to the three nearby binding sites. This is shown in the graph below. Because position n-1 is on average further, symmetry is broken. It is estimated by nuclear magnetic resonance (NMR) that there is a 2-3 kcal/mol change in binding free energy in the dark and light states of LOV2 available for use by this motor [Yao et al., 2008].

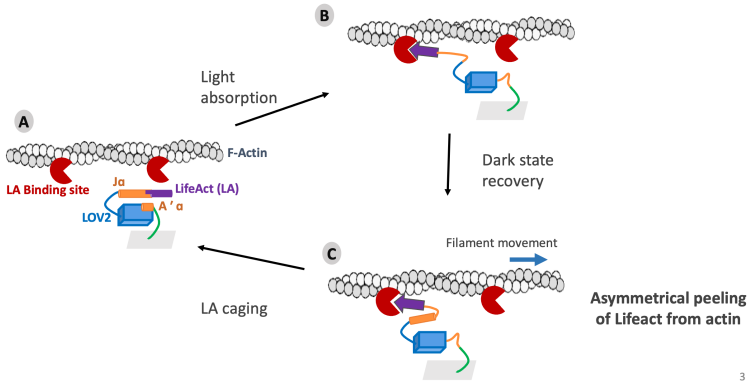

Figure 5.3: Schematic the LILAC motor photocycle. In the dark state, the ASLOV2's Jα remains folded so that Lifeact is caged and unable to bind actin. Upon blue light absorption, the Jα helix of AsLOV2 unfolds, which releases Lifeact to bind actin. In the next step, the Jα helix refolds and returns to the dark state, pulling on the actin filament. In the final step, the Lifeact unbinds and AsLOV2 relaxes back to its ground state where the Lifeact is caged so that when exposed to another light pulse, it can bind a new actin site.

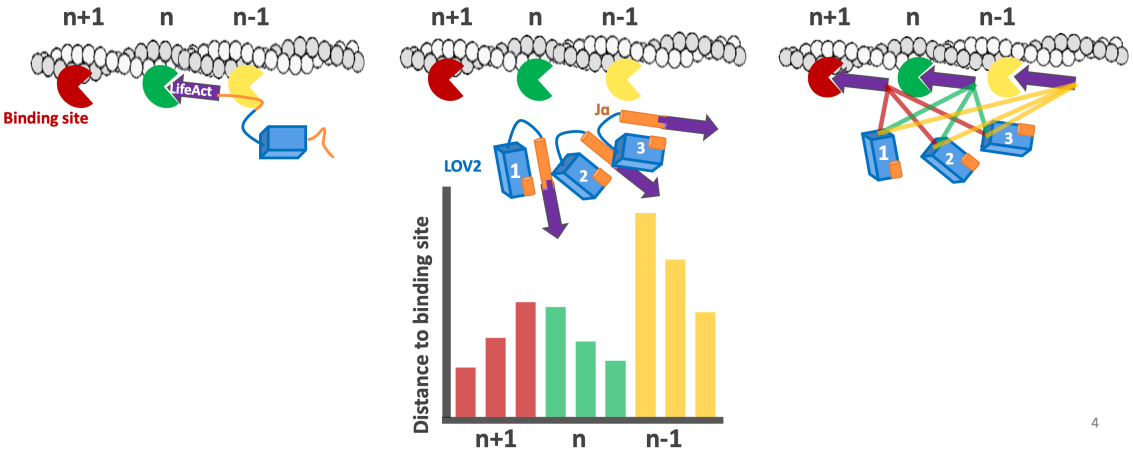

Figure 5.4: Schematic the LILAC motor asymmetry. When bound at position n, LILAC can rotate. However, because the Lifeact peptide binds along the filament, there is an inherent asymmetry. At each of the three rotational positions shown, the core is at a different distance to the three nearby binding sites. This is shown in the graph below.

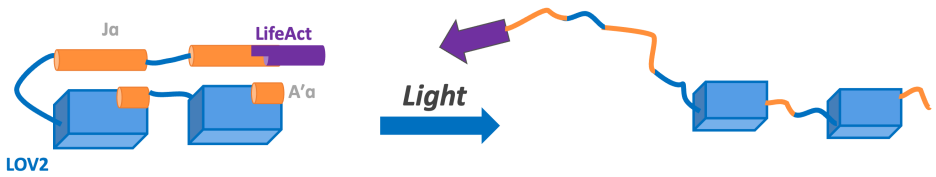

Figure 5.5: Schematic the addition of a second LOV2 domain for lever arm length. A second LOV2 domain inserted between the core and Jα helix extends the motor lever arm.

Functionality of the motor could be assessed using a gliding filament assay. In this assay, many LILAC molecules are fixed to a glass slide and filaments are added. Using red phalloidin labeled actin, the filaments can be visualized by excitement with far-red phalloidin, leaving 488nm free for exciting the LOV2-based motor. Pulsing 488nm light would lead to the binding and unbinding of LILAC to the filaments. Timing is critical for this to work; if LILAC recovers too fast, it cannot bind to a new actin subunit, but if it recovers too slowly, the filament will drift away. Luckily, the photocycle of LOV2 is tunable, and can be changed through sequence mutations, or addition of a base such as imidazole, which deprotonates the flavin mononucleotide of LOV2, leading to a shorter photocycle Zayner and Sosnick [2014], Zayner et al. [2013]. It is also possible that the unfolded Jα and Lifeact would not be long enough to reach the next binding site on actin. This can be addressed by inserting a second LOV2 domain into the loop before the Jα, thus doubling the lever arm length (Figure 5.5). In conclusion, given more time, I would anticipate creating a novel, light-driven protein motor that elucidates the core parts necessary for a protein motor.

5.5 Final remarks

In conclusion, I have developed a useful tool for analyzing the actin cytoskeleton in a number of ways. Thus far, LILAC has been used to improve cytoskeletal imaging by reducing negative side effects of labeling, and allowing for a number of imaging modes. LILAC also can be used to easily pattern actin filaments in a spatiotemporal manner, opening up the ability to answer a number of questions about the fundamental properties of the actin cytoskeleton. I proposed a number of additional ways LILAC can be used to answer myriad questions about the cytoskeleton, and hope that others find even more creative applications for this novel tool.

APPENDIX A

TESTING A SECOND LILAC DESIGN

To ensure that the LILAC design is optimal, we tested a second integration of Lifeact into the Jα helix. This design, known as LILAC2, inserts the Lifeact peptide after I539, aligning A540 of LOV2 with A4 of Lifeact (Figure A.1).

We tested the switching of LILAC2 by imaging mCherry-LILAC2 in insect cells before and after excitation with blue light. S2 cells for lamellipodial rings, allowing for quantification of switching using the pre/post actin labeling ratio (intensity in lamellipodium/intensity in cell interior, Figure A.1). LILAC2 does show increased switching in comparison to Lifeact (t-test p=3.6 e-20). However, LILAC2 has a significantly lower switching ratio than LILAC (t-test p = 1.8 e-4). Therefore, we conclude that LILAC is the ideal integration of Lifeact with the Jα for maximal switching.

Figure A.1: LILAC2 has reduced switching behavior. Left, Sequences of the LOV2 C-terminal Jα helix (turqoise) and Lifeact (gray). The template was created by integrating Lifeact while retaining the hydrophobic residues (orange) that interact with the core of LOV2. LILAC and LILAC2 were integrated to minimize disruption of the core, while inserting Lifeact sufficiently to cage Lifeact binding in the dark. Right, Maximum switching ratios (A.U.) of LILAC, LILAC2, and Lifeact., T-test results: LILAC2-Lifeact p=3.6e-20. LILAC-LILAC2 p=1.8e-4.

APPENDIX B

LILAC LABELING IN U2OS CELLS

We wanted to check that LILAC would label actin in a variety of cell types. U2OS cells were chosen as they were available and have long, beautiful actin structures when healthy. As shown in Figures B.2 and B.2, LILAC specifically labels U2OS actin structures post blue-light illumination in the lamellipodia. However, we did not see the stress fibers that we expected. This is likely due to the lack of a CO_2 and heating system that many use for live imaging of mammalian cells.

U2OS cells were maintained in DMEM (Thermo) +10% fetal bovine serum. Cells were split at 50-80% confluency every 2-3 days in 6-well plates after washing wish DPBS (Sigma) and trypsinizing for 2 minutes. For imaging, cells were seeded onto Delta T dishes (Fisher) for 24 hours. Then, cells were transfected using FuGene (Promega) according to the standard protocol. After 8 hours, media was changed to Fluoribrite DMEM (Thermo) and the dish was heated using a stage heater and objective heater set to 37°C.

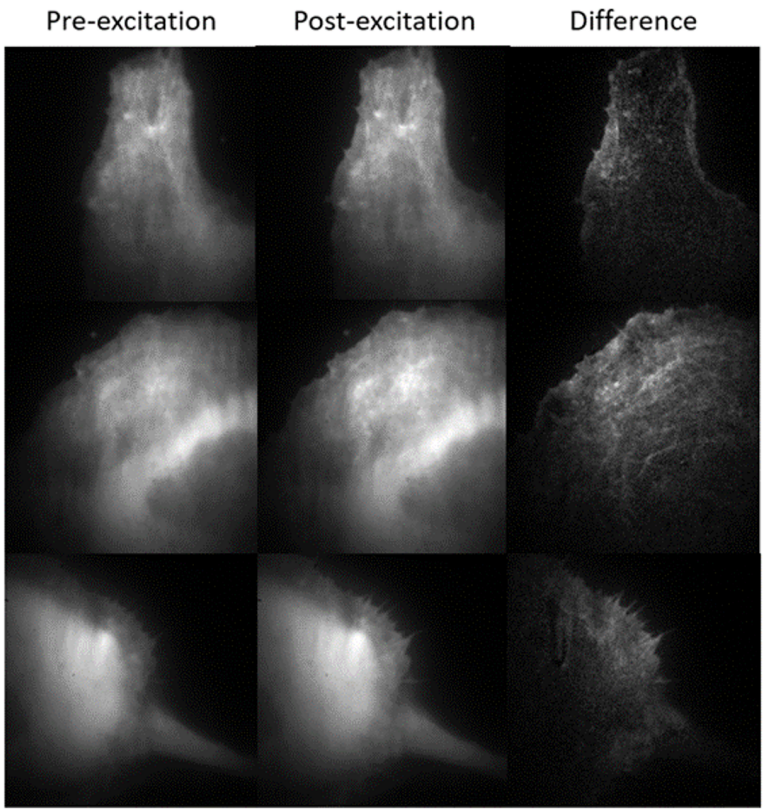

Figure B.1: LILAC labels U2OS actin structures in multiple cells. TIRF images of three U2OS cells expressing LILAC before and after excitation with blue light. The difference between pre and post excitation in shown on the right.

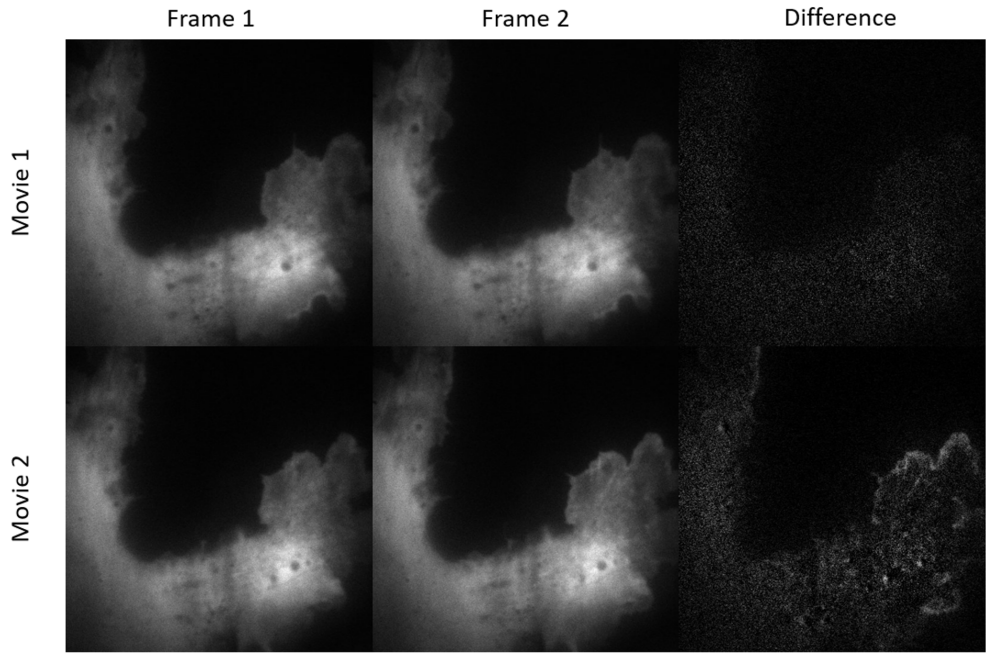

Figure B.2: LILAC specifically labels U2OS actin structures post blue-light illumination. TIRF images extracted from movies of a U2OS cell expressing LILAC. In movie 1, the cell is not exposed to blue light between frames 1 and 2. In movie 2, the cell is excited by blue light between the frames. The difference between the two images in shown in the left column.

REFERENCES

modlAMP: Python for antimicrobial peptides | Bioinformatics | Oxford Academic. URL https://academic.oup.com/bioinformatics/article/33/17/2753/3796392?login=false.

CPT Galaxy Tools, December 2022. URL https://github.com/TAMU-CPT/galaxy-tools. original-date: 2016-09-26T16:00:06Z.

AlphaFold, June 2023. URL https://github.com/deepmind/alphafold. original-date: 2021-06-17T14:06:06Z.

O. J. Abilez. Cardiac optogenetics. In *2012 Annual International Conference of the IEEE Engineering in Medicine and Biology Society*, pages 1386–1389, San Diego, CA, August 2012. IEEE. ISBN 978-1-4577-1787-1 978-1-4244-4119-8. doi: 10.1109/EMBC.2012.6346197. URL http://ieeexplore.ieee.org/document/6346197/.

Antoine Adamantidis, Silvia Arber, Jaideep S Bains, Ernst Bamberg, Antonello Bonci, György Buzsáki, Jessica A Cardin, Rui M Costa, Yang Dan, Yukiko Goda, Ann M Graybiel, Michael Häusser, Peter Hegemann, John R Huguenard, Thomas R Insel, Patricia H Janak, Daniel Johnston, Sheena A Josselyn, Christof Koch, Anatol C Kreitzer, Christian Lüscher, Robert C Malenka, Gero Miesenböck, Georg Nagel, Botond Roska, Mark J Schnitzer, Krishna V Shenoy, Ivan Soltesz, Scott M Sternson, Richard W Tsien, Roger Y Tsien, Gina G Turrigiano, Kay M Tye, and Rachel I Wilson. Optogenetics: 10 years after ChR2 in neurons—views from the community. *Nature Neuroscience*, 18(9): 1202–1212, September 2015. ISSN 1097-6256, 1546-1726. doi: 10.1038/nn.4106. URL https://www.nature.com/articles/nn.4106.

Hillel Adesnik and Lamiae Abdeladim. Probing neural codes with two-photon holographic optogenetics. *Nature Neuroscience*, 24(10):1356–1366, October 2021. ISSN 1097-6256, 1546-1726. doi: 10.1038/s41593-021-00902-9. URL https://www.nature.com/articles/s41593-021-00902-9.

Hiroyuki Aizawa, Masazumi Sameshima, and Ichiro Yahara. A Green Fluorescent Protein-actin Fusion Protein Dominantly Inhibits Cytokinesis, Cell Spreading, and Locomotion in Dictyostelium. *Cell Structure and Function*, 22(3):335–345, 1997. ISSN 0386-7196, 1347-3700. doi: 10.1247/csf.22.335. URL http://www.jstage.jst.go.jp/article/csf1975/22/3/22_3_335/_article.

Maxime T. A. Alexandre, Jos C. Arents, Rienk van Grondelle, Klaas J. Hellingwerf, and John T. M. Kennis. A Base-Catalyzed Mechanism for Dark State Recovery in the *Avena sativa* Phototropin-1 LOV2 Domain. *Biochemistry*, 46(11):3129–3137, March 2007. ISSN 0006-2960, 1520-4995. doi: 10.1021/bi062074e. URL https://pubs.acs.org/doi/10.1021/bi062074e.

Christina M Ambrosi and Emilia Entcheva. Optogenetics‘ promise: pacing and cardioversion by light? *Future Cardiology*, 10(1):1–4, January 2014. ISSN 1479-6678, 1744-8298. doi: 10.2217/fca.13.89. URL https://www.futuremedicine.com/doi/10.2217/fca.13.89.

Christina M. Ambrosi, Aleksandra Klimas, Jinzhu Yu, and Emilia Entcheva. Cardiac applications of optogenetics. *Progress in Biophysics and Molecular Biology*, 115(2-3): 294–304, August 2014. ISSN 00796107. doi: 10.1016/j.pbiomolbio.2014.07.001. URL https://linkinghub.elsevier.com/retrieve/pii/S0079610714000637.

James R Bartles. Parallel actin bundles and their multiple actin-bundling proteins. *Current Opinion in Cell Biology*, 12(1):72–78, February 2000. ISSN 09550674. doi: 10.1016/S0955-0674(99)00059-9. URL https://linkinghub.elsevier.com/retrieve/pii/S0955067499000599.

Jennifer L. Bays and Kris A. DeMali. Vinculin in cell–cell and cell–matrix adhesions. *Cellular and Molecular Life Sciences*, 74(16):2999–3009, August 2017. ISSN 1420-682X, 1420-9071. doi: 10.1007/s00018-017-2511-3. URL http://link.springer.com/10.1007/s00018-017-2511-3.

Carlos Bazan, David Torres Barba, Peter Blomgren, and Paul Paolini. Image Processing Techniques for Assessing Contractility in Isolated Neonatal Cardiac Myocytes. *International Journal of Biomedical Imaging*, 2011:1–9, 2011. ISSN 1687-4188, 1687-4196. doi: 10.1155/2011/729732. URL http://www.hindawi.com/journals/ijbi/2011/729732/.

Thomas Beiert, Tobias Bruegmann, and Philipp Sasse. Optogenetic activation of Gq signalling modulates pacemaker activity of cardiomyocytes. *Cardiovascular Research*, 102(3): 507–516, June 2014. ISSN 1755-3245, 0008-6363. doi: 10.1093/cvr/cvu046. URL https://academic.oup.com/cardiovascres/article-lookup/doi/10.1093/cvr/cvu046.

Brittany J Belin, Lauren M Goins, and R Dyche Mullins. Comparative analysis of tools for live cell imaging of actin network architecture. *BioArchitecture*, 4(6):189–202, June 2014. ISSN 1949-0992, 1949-100X. doi: 10.1080/19490992.2014.1047714. URL https://www.tandfonline.com/doi/full/10.1080/19490992.2014.1047714.

Alexander Belyy, Felipe Merino, Oleg Sitsel, and Stefan Raunser. Structure of the Lifeact–F-actin complex. *PLOS Biology*, 18(11):e3000925, November 2020. ISSN 1545-7885. doi: 10.1371/journal.pbio.3000925. URL https://dx.plos.org/10.1371/journal.pbio.3000925.

Debasis Bera, Lei Qian, Teng-Kuan Tseng, and Paul H. Holloway. Quantum Dots and Their Multimodal Applications: A Review. *Materials*, 3(4):2260–2345, March 2010. ISSN 1996-1944. doi: 10.3390/ma3042260. URL http://www.mdpi.com/1996-1944/3/4/2260.

Laurent Blanchoin, Rajaa Boujemaa-Paterski, Cécile Sykes, and Julie Plastino. Actin Dynamics, Architecture, and Mechanics in Cell Motility. *Physiological Reviews*, 94(1):235–263, January 2014. ISSN 0031-9333, 1522-1210. doi: 10.1152/physrev.00018.2013. URL https://www.physiology.org/doi/10.1152/physrev.00018.2013.

Francesca Boccafoschi, Cecilia Mosca, Martina Ramella, Guido Valente, and Mario Cannas. The effect of mechanical strain on soft (cardiovascular) and hard (bone) tissues: Common pathways for different biological outcomes. *Cell Adhesion & Migration*, 7(2):165–173, March 2013. ISSN 1933-6918, 1933-6926. doi: 10.4161/cam.23020. URL http://www.tandfonline.com/doi/abs/10.4161/cam.23020.

Maria A. Brehm, Isabell Schreiber, Uwe Bertsch, Albrecht Wegner, and Georg W. Mayr. Identification of the actin-binding domain of Ins(1,4,5) *P* 3 3-kinase isoform B (IP3K-B). *Biochemical Journal*, 382(1):353–362, August 2004. ISSN 0264-6021, 1470-8728. doi: 10.1042/BJ20031751. URL https://portlandpress.com/biochemj/article/382/1/353/78609/Identification-of-the-actin-binding-domain-of-Ins.

Eric R. Brooks and John B. Wallingford. Multiciliated Cells. *Current Biology*, 24(19):R973–R982, October 2014. ISSN 09609822. doi: 10.1016/j.cub.2014.08.047. URL https://linkinghub.elsevier.com/retrieve/pii/S0960982214010604.

Thomas A. Bunch, Yevgenya Grinblat, and Lawrence S.B. Goldstein. Characterization and use of the *Drosophila* metallothionein promoter in cultured *Drosophila melanogaster* cells. *Nucleic Acids Research*, 16(3):1043–1061, 1988. ISSN 0305-1048, 1362-4962. doi: 10.1093/nar/16.3.1043. URL https://academic.oup.com/nar/article-lookup/doi/10.1093/nar/16.3.1043.

Brian M. Burkel, George von Dassow, and William M. Bement. Versatile fluorescent probes for actin filaments based on the actin-binding domain of utrophin. *Cell Motility and the Cytoskeleton*, 64(11):822–832, November 2007. ISSN 08861544, 10970169. doi: 10.1002/cm.20226. URL https://onlinelibrary.wiley.com/doi/10.1002/cm.20226.

Daniel W. Buster, Jonathan Nye, Joseph E. Klebba, and Gregory C. Rogers. Preparation of Drosophila S2 cells for Light Microscopy. *Journal of Visualized Experiments*, (40):1982, June 2010. ISSN 1940-087X. doi: 10.3791/1982. URL http://www.jove.com/index/Details.stp?ID=1982.

Kate E. Cavanaugh, Michael F. Staddon, Edwin Munro, Shiladitya Banerjee, and Margaret L. Gardel. RhoA Mediates Epithelial Cell Shape Changes via Mechanosensitive Endocytosis. *Developmental Cell*, 52(2):152–166.e5, January 2020. ISSN 15345807. doi: 10.1016/j.devcel.2019.12.002. URL https://linkinghub.elsevier.com/retrieve/pii/S1534580719310238.

Martin Chalfie, Yuan Tu, Ghia Euskirchen, William W. Ward, and Douglas C. Prasher. Green Fluorescent Protein as a Marker for Gene Expression. *Science*, 263(5148):802–805, February 1994. ISSN 0036-8075, 1095-9203. doi: 10.1126/science.8303295. URL https://www.science.org/doi/10.1126/science.8303295.

Lu Chen, Muneaki Nakamura, Tony D. Schindler, David Parker, and Zev Bryant. Engineering controllable bidirectional molecular motors based on myosin. *Nature Nanotechnology*, 7(4):252–256, April 2012. ISSN 1748-3387, 1748-3395. doi: 10.1038/nnano.2012.19. URL https://www.nature.com/articles/nnano.2012.19.

Wenqing Chen, Chen Li, Wanmin Liang, Yunqi Li, Zhuoheng Zou, Yunxuan Xie, Yangzeng Liao, Lin Yu, Qianyi Lin, Meiying Huang, Zesong Li, and Xiao Zhu. The Roles of Optogenetics and Technology in Neurobiology: A Review. *Frontiers in Aging Neuroscience*, 14:867863, April 2022. ISSN 1663-4365. doi: 10.3389/fnagi.2022.867863. URL https://www.frontiersin.org/articles/10.3389/fnagi.2022.867863/full.

John M. Christie, Michael Salomon, Kazunari Nozue, Masamitsu Wada, and Winslow R. Briggs. LOV (light, oxygen, or voltage) domains of the blue-light photoreceptor phototropin (nph1): Binding sites for the chromophore flavin mononucleotide. *Proceedings of the National Academy of Sciences*, 96(15):8779–8783, July 1999. ISSN 0027-8424, 1091-6490. doi: 10.1073/pnas.96.15.8779. URL https://pnas.org/doi/full/10.1073/pnas.96.15.8779.

William C. Claycomb, Nicholas A. Lanson, Beverly S. Stallworth, Daniel B. Egeland, Joseph B. Delcarpio, Anthony Bahinski, and Nicholas J. Izzo. HL-1 cells: A cardiac muscle cell line that contracts and retains phenotypic characteristics of the adult cardiomyocyte. *Proceedings of the National Academy of Sciences*, 95(6):2979–2984, March 1998. ISSN 0027-8424, 1091-6490. doi: 10.1073/pnas.95.6.2979. URL https://pnas.org/doi/full/10.1073/pnas.95.6.2979.

Ohad Cohen and Samuel A. Safran. Theory of frequency response of mechanically driven cardiomyocytes. *Scientific Reports*, 8(1):2237, February 2018. ISSN 2045-2322. doi: 10.1038/s41598-018-20307-2. URL https://www.nature.com/articles/s41598-018-20307-2.

Lindsey M. Costantini, Mikhail Baloban, Michele L. Markwardt, Megan A. Rizzo, Feng Guo, Vladislav V. Verkhusha, and Erik L. Snapp. A palette of fluorescent proteins optimized for diverse cellular environments. *Nature Communications*, 6(1):7670, July 2015. ISSN 2041-1723. doi: 10.1038/ncomms8670. URL https://www.nature.com/articles/ncomms8670.

David S. Courson and Ronald S. Rock. Actin Cross-link Assembly and Disassembly Mechanics for a-Actinin and Fascin. *Journal of Biological Chemistry*, 285(34):26350–26357, August 2010. ISSN 00219258. doi: 10.1074/jbc.M110.123117. URL https://linkinghub.elsevier.com/retrieve/pii/S0021925820596002.

Naomi Courtemanche, Thomas D. Pollard, and Qian Chen. Avoiding artefacts when counting polymerized actin in live cells with LifeAct fused to fluorescent proteins. *Nature Cell Biology*, 18(6):676–683, June 2016. ISSN 1465-7392, 1476-4679. doi: 10.1038/ncb3351. URL http://www.nature.com/articles/ncb3351.

Sean Crosson and Keith Moffat. Structure of a flavin-binding plant photoreceptor domain: Insights into light-mediated signal transduction. *Proceedings of the National Academy of Sciences*, 98(6):2995–3000, March 2001. ISSN 0027-8424, 1091-6490. doi: 10.1073/pnas.051520298. URL https://pnas.org/doi/full/10.1073/pnas.051520298.

Sean Crosson and Keith Moffat. Photoexcited Structure of a Plant Photoreceptor Domain Reveals a Light-Driven Molecular Switch. *The Plant Cell*, 14(5):1067–1075, May 2002. ISSN 1040-4651, 1532-298X. doi: 10.1105/tpc.010475. URL https://academic.oup.com/plcell/article/14/5/1067-1075/6009734.

Karl Deisseroth. Optogenetics: 10 years of microbial opsins in neuroscience. *Nature Neuroscience*, 18(9):1213–1225, September 2015. ISSN 1097-6256, 1546-1726. doi: 10.1038/nn.4091. URL https://www.nature.com/articles/nn.4091.

Torsten Doenst, Tien Dung Nguyen, and E. Dale Abel. Cardiac Metabolism in Heart Failure: Implications Beyond ATP Production. *Circulation Research*, 113(6):709–724, August 2013. ISSN 0009-7330, 1524-4571. doi: 10.1161/CIRCRESAHA.113.300376. URL https://www.ahajournals.org/doi/10.1161/CIRCRESAHA.113.300376.

Roberto Dominguez and Kenneth C. Holmes. Actin Structure and Function. *Annual Review of Biophysics*, 40(1):169–186, June 2011. ISSN 1936-122X, 1936-1238. doi: 10.1146/annurev-biophys-042910-155359. URL https://www.annualreviews.org/doi/10.1146/annurev-biophys-042910-155359.

Liting Duan, Jen Hope, Qunxiang Ong, Hsin-Ya Lou, Namdoo Kim, Comfrey McCarthy, Victor Acero, Michael Z. Lin, and Bianxiao Cui. Understanding CRY2 interactions for optical control of intracellular signaling. *Nature Communications*, 8(1):547, September 2017. ISSN 2041-1723. doi: 10.1038/s41467-017-00648-8. URL https://www.nature.com/articles/s41467-017-00648-8.

Emilia Entcheva and Matthew W. Kay. Cardiac optogenetics: a decade of enlightenment. *Nature Reviews Cardiology*, 18(5):349–367, May 2021. ISSN 1759-5002, 1759-5010. doi: 10.1038/s41569-020-00478-0. URL http://www.nature.com/articles/s41569-020-00478-0.

Michael Fairhead and Mark Howarth. Site-Specific Biotinylation of Purified Proteins Using BirA. In Arnaud Gautier and Marlon J. Hinner, editors, *Site-Specific Protein Labeling*, volume 1266, pages 171–184. Springer New York, New York, NY, 2015a. ISBN 978-1-4939-2271-0 978-1-4939-2272-7. doi: 10.1007/978-1-4939-2272-7_12. URL https://link.springer.com/10.1007/978-1-4939-2272-7_12.

Michael Fairhead and Mark Howarth. Site-Specific Biotinylation of Purified Proteins Using BirA. In Arnaud Gautier and Marlon J. Hinner, editors, *Site-Specific Protein Labeling*, volume 1266, pages 171–184. Springer New York, New York, NY, 2015b. ISBN 978-1-4939-2271-0 978-1-4939-2272-7. doi: 10.1007/978-1-4939-2272-7_12. URL https://link.springer.com/10.1007/978-1-4939-2272-7_12. Series Title: Methods in Molecular Biology.

Luis R. Flores, Michael C. Keeling, Xiaoli Zhang, Kristina Sliogeryte, and Núria Gavara. Lifeact-TagGFP2 alters F-actin organization, cellular morphology and biophysical behaviour. *Scientific Reports*, 9(1):3241, March 2019. ISSN 2045-2322. doi: 10.1038/s41598-019-40092-w. URL https://www.nature.com/articles/s41598-019-40092-w.

Kate S. Foley and Paul W. Young. The non-muscle functions of actinins: an update. *Biochemical Journal*, 459(1):1–13, April 2014. ISSN 0264-6021, 1470-8728. doi: 10.1042/BJ20131511. URL https://portlandpress.com/biochemj/article/459/1/1/46646/The-non-muscle-functions-of-actinins-an-update.

Alexander R. French, Tobin R. Sosnick, and Ronald S. Rock. Investigations of human myosin VI targeting using optogenetically controlled cargo loading. *Proceedings of the National Academy of Sciences*, 114(9), February 2017. ISSN 0027-8424, 1091-6490. doi: 10.1073/pnas.1614716114. URL https://pnas.org/doi/full/10.1073/pnas.1614716114.

Laurène Gressin, Audrey Guillotin, Christophe Guérin, Laurent Blanchoin, and Alphée Michelot. Architecture Dependence of Actin Filament Network Disassembly. *Current Biology*, 25(11):1437–1447, June 2015. ISSN 09609822. doi: 10.1016/j.cub.2015.04.011. URL https://linkinghub.elsevier.com/retrieve/pii/S0960982215004248.

Gurkan Guntas, Ryan A. Hallett, Seth P. Zimmerman, Tishan Williams, Hayretin Yumerefendi, James E. Bear, and Brian Kuhlman. Engineering an improved light-induced dimer (iLID) for controlling the localization and activity of signaling proteins. *Proceedings of the National Academy of Sciences*, 112(1):112–117, January 2015. ISSN 0027-8424, 1091-6490. doi: 10.1073/pnas.1417910112. URL https://pnas.org/doi/full/10.1073/pnas.1417910112.

Andrei S. Halavaty and Keith Moffat. N- and C-Terminal Flanking Regions Modulate Light-Induced Signal Transduction in the LOV2 Domain of the Blue Light Sensor Phototropin 1 from *Avena sativa* ›. *Biochemistry*, 46(49):14001–14009, December 2007. ISSN 0006-2960, 1520-4995. doi: 10.1021/bi701543e. URL https://pubs.acs.org/doi/10.1021/bi701543e.

K Han. An efficient DDAB-mediated transfection of Drosophila S2 cells. *Nucleic Acids Research*, 24(21):4362–4363, November 1996. ISSN 13624962. doi: 10.1093/nar/24.21.4362. URL https://academic.oup.com/nar/article-lookup/doi/10.1093/nar/24.21.4362.

Shannon M. Harper, Lori C. Neil, and Kevin H. Gardner. Structural Basis of a Phototropin Light Switch. *Science*, 301(5639):1541–1544, September 2003. ISSN 0036-8075, 1095-9203. doi: 10.1126/science.1086810. URL https://www.science.org/doi/10.1126/science.1086810.

Shannon M. Harper, John M. Christie, and Kevin H. Gardner. Disruption of the LOV-Ja Helix Interaction Activates Phototropin Kinase Activity. *Biochemistry*, 43(51):16184–16192, December 2004. ISSN 0006-2960, 1520-4995. doi: 10.1021/bi048092i. URL https://pubs.acs.org/doi/10.1021/bi048092i.

M. Amanda Hartman and James A. Spudich. The myosin superfamily at a glance. *Journal of Cell Science*, 125(7):1627–1632, April 2012. ISSN 1477-9137, 0021-9533. doi: 10.1242/jcs.094300. URL https://journals.biologists.com/jcs/article/125/7/1627/33209/The-myosin-superfamily-at-a-glance.

Lian He, Peng Tan, Lei Zhu, Kai Huang, Nhung T. Nguyen, Rui Wang, Lei Guo, Ling Li, Yuhan Yang, Zixian Huang, Yun Huang, Gang Han, Junfeng Wang, and Yubin Zhou. Circularly permuted LOV2 as a modular photoswitch for optogenetic engineering. *Nature Chemical Biology*, 17(8):915–923, August 2021. ISSN 1552-4450, 1552-4469. doi: 10.1038/s41589-021-00792-9. URL http://www.nature.com/articles/s41589-021-00792-9.

Jonathon A. Heier, Daniel J. Dickinson, and Adam V. Kwiatkowski. Measuring Protein Binding to F-actin by Co-sedimentation. *Journal of Visualized Experiments*, (123):55613, May 2017. ISSN 1940-087X. doi: 10.3791/55613. URL https://www.jove.com/video/55613/measuring-protein-binding-to-f-actin-by-co-sedimentation.

Mohammad Mosharraf Hossain, Eiichi Shimizu, Masato Saito, Sathuluri Ramachandra Rao, Yoshinori Yamaguchi, and Eiichi Tamiya. Non-invasive characterization of mouse embryonic stem cell derived cardiomyocytes based on the intensity variation in digital beating video. *The Analyst*, 135(7):1624, 2010. ISSN 0003-2654, 1364-5528. doi: 10.1039/c0an00208a. URL http://xlink.rsc.org/?DOI=c0an00208a.

Robert M. Hughes and David S. Lawrence. Optogenetic Engineering: Light-Directed Cell Motility. *Angewandte Chemie International Edition*, 53(41):10904–10907, October 2014. ISSN 14337851. doi: 10.1002/anie.201404198. URL https://onlinelibrary.wiley.com/doi/10.1002/anie.201404198.

Tomohiro Ishii, Koji Sato, Toshiyuki Kakumoto, Shigenori Miura, Kazushige Touhara, Shoji Takeuchi, and Takao Nakata. Light generation of intracellular Ca2+ signals by a genetically encoded protein BACCS. *Nature Communications*, 6(1):8021, August 2015. ISSN 2041-1723. doi: 10.1038/ncomms9021. URL https://www.nature.com/articles/ncomms9021.

Emiliano Izquierdo, Theresa Quinkler, and Stefano De Renzis. Guided morphogenesis through optogenetic activation of Rho signalling during early Drosophila embryogenesis. *Nature Communications*, 9(1):2366, June 2018. ISSN 2041-1723. doi: 10.1038/s41467-018-04754-z. URL https://www.nature.com/articles/s41467-018-04754-z.

Silvia Jansen, Agnieszka Collins, Changsong Yang, Grzegorz Rebowski, Tatyana Svitkina, and Roberto Dominguez. Mechanism of Actin Filament Bundling by Fascin. *Journal of Biological Chemistry*, 286(34):30087–30096, August 2011. ISSN 00219258. doi: 10.1074/jbc.M111.251439. URL https://linkinghub.elsevier.com/retrieve/pii/S0021925819760852.

Zhiheng Jia, Virginijus Valiunas, Zongju Lu, Harold Bien, Huilin Liu, Hong-Zhang Wang, Barbara Rosati, Peter R. Brink, Ira S. Cohen, and Emilia Entcheva. Stimulating Cardiac Muscle by Light: Cardiac Optogenetics by Cell Delivery. *Circulation: Arrhythmia and Electrophysiology*, 4(5):753–760, October 2011. ISSN 1941-3149, 1941-3084. doi: 10.1161/CIRCEP.111.964247. URL https://www.ahajournals.org/doi/10.1161/CIRCEP.111.964247.

Jyotsna Joshi, Michael Rubart, and Wuqiang Zhu. Optogenetics: Background, Methodological Advances and Potential Applications for Cardiovascular Research and Medicine. *Frontiers in Bioengineering and Biotechnology*, 7:466, January 2020. ISSN 2296-4185. doi: 10.3389/fbioe.2019.00466. URL https://www.frontiersin.org/article/10.3389/fbioe.2019.00466/full.

Rachel S. Kadzik, Kaitlin E. Homa, and David R. Kovar. F-Actin Cytoskeleton Network Self-Organization Through Competition and Cooperation. *Annual Review of Cell and Developmental Biology*, 36(1):35–60, October 2020. ISSN 1081-0706, 1530-8995. doi: 10.1146/annurev-cellbio-032320-094706. URL https://www.annualreviews.org/doi/10.1146/annurev-cellbio-032320-094706.

Fuun Kawano, Hideyuki Suzuki, Akihiro Furuya, and Moritoshi Sato. Engineered pairs of distinct photoswitches for optogenetic control of cellular proteins. *Nature Communications*, 6(1):6256, February 2015. ISSN 2041-1723. doi: 10.1038/ncomms7256. URL https://www.nature.com/articles/ncomms7256.

John T. M. Kennis, Ivo H. M. van Stokkum, Sean Crosson, Magdalena Gauden, Keith Moffat, and Rienk van Grondelle. The LOV2 Domain of Phototropin: A Reversible Photochromic Switch. *Journal of the American Chemical Society*, 126(14):4512–4513, April 2004. ISSN 0002-7863, 1520-5126. doi: 10.1021/ja031840r. URL https://pubs.acs.org/doi/10.1021/ja031840r.

Yongdeok Kim, Yiyuan Yang, Xiaotian Zhang, Zhengwei Li, Abraham Vázquez-Guardado, Insu Park, Jiaojiao Wang, Andrew I. Efimov, Zhi Dou, Yue Wang, Junehu Park, Haiwen Luan, Xinchen Ni, Yun Seong Kim, Janice Baek, Joshua Jaehyung Park, Zhaoqian Xie, Hangbo Zhao, Mattia Gazzola, John A. Rogers, and Rashid Bashir. Remote control of muscle-driven miniature robots with battery-free wireless optoelectronics. *Science Robotics*, 8(74):eadd1053, January 2023. ISSN 2470-9476. doi: 10.1126/scirobotics.add1053. URL https://www.science.org/doi/10.1126/scirobotics.add1053.

Anatoly B. Kolomeisky and Michael E. Fisher. Molecular Motors: A Theorist's Perspective. *Annual Review of Physical Chemistry*, 58(1):675–695, May 2007. ISSN 0066-426X, 1545-1593. doi: 10.1146/annurev.physchem.58.032806.104532. URL https://www.annualreviews.org/doi/10.1146/annurev.physchem.58.032806.104532.

Kourtney L. Kroll, Alexander R. French, Tobin R. Sosnick, and Ronald S. Rock. LILAC: enhanced actin imaging with an optogenetic Lifeact. *Nature Methods*, 20(2):214–217, February 2023. ISSN 1548-7091, 1548-7105. doi: 10.1038/s41592-022-01761-3. URL https://www.nature.com/articles/s41592-022-01761-3.

Anil Kumar, Darcy C. Burns, M. Sameer Al-Abdul-Wahid, and G. Andrew Woolley. A Circularly Permuted Photoactive Yellow Protein as a Scaffold for Photoswitch Design. *Biochemistry*, 52(19):3320–3331, May 2013. ISSN 0006-2960, 1520-4995. doi: 10.1021/bi400018h. URL https://pubs.acs.org/doi/10.1021/bi400018h.

Archana Kumari, Shubham Kesarwani, Manjunath G Javoor, Kutti R Vinothkumar, and Minhajuddin Sirajuddin. Structural insights into actin filament recognition by commonly used cellular actin markers. *The EMBO Journal*, 39(14), July 2020. ISSN 0261-4189, 1460-2075. doi: 10.15252/embj.2019104006. URL https://onlinelibrary.wiley.com/doi/10.15252/embj.2019104006.

Keel Yong Lee, Sung-Jin Park, David G. Matthews, Sean L. Kim, Carlos Antonio Marquez, John F. Zimmerman, Herdeline Ann M. Ardoña, Andre G. Kleber, George V. Lauder, and Kevin Kit Parker. An autonomously swimming biohybrid fish designed with human cardiac biophysics. *Science*, 375(6581):639–647, February 2022. ISSN 0036-8075, 1095-9203. doi: 10.1126/science.abh0474. URL https://www.science.org/doi/10.1126/science.abh0474.

Gaëlle Letort, Antonio Z. Politi, Hajer Ennomani, Manuel Théry, Francois Nedelec, and Laurent Blanchoin. Geometrical and Mechanical Properties Control Actin Filament Organization. *PLOS Computational Biology*, 11(5):e1004245, May 2015. ISSN 1553-7358. doi: 10.1371/journal.pcbi.1004245. URL https://dx.plos.org/10.1371/journal.pcbi.1004245.

Feng Liu, Huimin Hu, Mengying Deng, Zongqin Xiang, Yuting Guo, Xinmeng Guan, Dong Li, Qinxue Hu, Wenliang Lei, Hongjuan Peng, and Jun Chu. A Bright Monomeric Near-Infrared Fluorescent Protein with an Excitation Peak at 633 nm for Labeling Cellular Protein and Reporting Protein–Protein Interaction. *ACS Sensors*, 7(7):1855–1866, July 2022. ISSN 2379-3694, 2379-3694. doi: 10.1021/acssensors.2c00286. URL https://pubs.acs.org/doi/10.1021/acssensors.2c00286.

Hongtao Liu, Xuhong Yu, Kunwu Li, John Klejnot, Hongyun Yang, Dominique Lisiero, and Chentao Lin. Photoexcited CRY2 Interacts with CIB1 to Regulate Transcription and Floral Initiation in *Arabidopsis*. *Science*, 322(5907):1535–1539, December 2008. ISSN 0036-8075, 1095-9203. doi: 10.1126/science.1163927. URL https://www.science.org/doi/10.1126/science.1163927.

Xiaocen Lu, Yi Shen, and Robert E. Campbell. Engineering Photosensory Modules of Non-Opsin-Based Optogenetic Actuators. *International Journal of Molecular Sciences*, 21(18): 6522, September 2020. ISSN 1422-0067. doi: 10.3390/ijms21186522. URL https://www.mdpi.com/1422-0067/21/18/6522.

Oana I. Lungu, Ryan A. Hallett, Eun Jung Choi, Mary J. Aiken, Klaus M. Hahn, and Brian Kuhlman. Designing Photoswitchable Peptides Using the AsLOV2 Domain. *Chemistry & Biology*, 19(4):507–517, April 2012. ISSN 10745521. doi: 10.1016/j.chembiol.2012.02.006. URL https://linkinghub.elsevier.com/retrieve/pii/S1074552112000798.

Robert C. Lyon, Fabian Zanella, Jeffrey H. Omens, and Farah Sheikh. Mechanotransduction in Cardiac Hypertrophy and Failure. *Circulation Research*, 116(8):1462–1476, April 2015. ISSN 0009-7330, 1524-4571. doi: 10.1161/CIRCRESAHA.116.304937. URL https://www.ahajournals.org/doi/10.1161/CIRCRESAHA.116.304937.

Gerard Marriott, Shu Mao, Tomoyo Sakata, Jing Ran, David K. Jackson, Chutima Petchprayoon, Timothy J. Gomez, Erica Warp, Orapim Tulyathan, Holly L. Aaron, Ehud Y. Isacoff, and Yuling Yan. Optical lock-in detection imaging microscopy for contrast-enhanced imaging in living cells. *Proceedings of the National Academy of Sciences*, 105(46): 17789–17794, November 2008. ISSN 0027-8424, 1091-6490. doi: 10.1073/pnas.0808882105. URL https://pnas.org/doi/full/10.1073/pnas.0808882105.

Daisuke Matsuoka and Satoru Tokutomi. Blue light-regulated molecular switch of Ser/Thr kinase in phototropin. *Proceedings of the National Academy of Sciences*, 102(37):13337–13342, September 2005. ISSN 0027-8424, 1091-6490. doi: 10.1073/pnas.0506402102. URL https://pnas.org/doi/full/10.1073/pnas.0506402102.

Joyce C.M. Meiring, Ilya Grigoriev, Wilco Nijenhuis, Lukas C. Kapitein, and Anna Akhmanova. Opto-katanin, an optogenetic tool for localized, microtubule disassembly. *Current Biology*, 32(21):4660–4674.e6, November 2022. ISSN 09609822. doi: 10.1016/j.cub.2022.09.010. URL https://linkinghub.elsevier.com/retrieve/pii/S0960982222014543.

Michael Melak, Matthias Plessner, and Robert Grosse. Actin visualization at a glance. *Journal of Cell Science*, 130(3):525–530, February 2017. ISSN 0021-9533. doi: 10.1242/jcs.189068. URL https://journals.biologists.com/jcs/article/130/3/525/56578/Actin-visualization-at-a-glance.

Jing Men, Airong Li, Jason Jerwick, Zilong Li, Rudolph E. Tanzi, and Chao Zhou. Non-invasive red-light optogenetic control of Drosophila cardiac function. *Communications Biology*, 3(1):336, June 2020. ISSN 2399-3642. doi: 10.1038/s42003-020-1065-3. URL https://www.nature.com/articles/s42003-020-1065-3.

Alphée Michelot and David G. Drubin. Building Distinct Actin Filament Networks in a Common Cytoplasm. *Current Biology*, 21(14):R560–R569, July 2011. ISSN 09609822. doi: 10.1016/j.cub.2011.06.019. URL https://linkinghub.elsevier.com/retrieve/pii/S0960982211006646.

Victor Muñoz and Luis Serrano. Elucidating the folding problem of helical peptides using empirical parameters. *Nature Structural & Molecular Biology*, 1(6):399–409, June 1994. ISSN 1545-9993, 1545-9985. doi: 10.1038/nsb0694-399. URL https://www.nature.com/doifinder/10.1038/nsb0694-399.

Diana C. Muñoz-Lasso, Carlos Romá-Mateo, Federico V. Pallardó, and Pilar Gonzalez-Cabo. Much More Than a Scaffold: Cytoskeletal Proteins in Neurological Disorders. *Cells*, 9(2):358, February 2020. ISSN 2073-4409. doi: 10.3390/cells9020358. URL https://www.mdpi.com/2073-4409/9/2/358.

Alex T Müller, Gisela Gabernet, Jan A Hiss, and Gisbert Schneider. modlAMP: Python for antimicrobial peptides. *Bioinformatics*, 33(17):2753–2755, September 2017. ISSN 1367-4803, 1367-4811. doi: 10.1093/bioinformatics/btx285. URL https://academic.oup.com/bioinformatics/article/33/17/2753/3796392.

Muneaki Nakamura, Lu Chen, Stuart C. Howes, Tony D. Schindler, Eva Nogales, and Zev Bryant. Remote control of myosin and kinesin motors using light-activated gearshifting. *Nature Nanotechnology*, 9(9):693–697, September 2014. ISSN 1748-3387, 1748-3395. doi: 10.1038/nnano.2014.147. URL https://www.nature.com/articles/nnano.2014.147.

Dean E. Natwick and Sean R. Collins. Optimized iLID Membrane Anchors for Local Optogenetic Protein Recruitment. *ACS Synthetic Biology*, 10(5):1009–1023, May 2021. ISSN 2161-5063, 2161-5063. doi: 10.1021/acssynbio.0c00511. URL https://pubs.acs.org/doi/10.1021/acssynbio.0c00511.

Dominik Niopek, Dirk Benzinger, Julia Roensch, Thomas Draebing, Pierre Wehler, Roland Eils, and Barbara Di Ventura. Engineering light-inducible nuclear localization signals for precise spatiotemporal control of protein dynamics in living cells. *Nature Communications*, 5(1):4404, July 2014. ISSN 2041-1723. doi: 10.1038/ncomms5404. URL https://www.nature.com/articles/ncomms5404.

Ido Nitsan, Stavit Drori, Yair E. Lewis, Shlomi Cohen, and Shelly Tzlil. Mechanical communication in cardiac cell synchronized beating. *Nature Physics*, 12(5):472–477, May 2016. ISSN 1745-2473, 1745-2481. doi: 10.1038/nphys3619. URL http://www.nature.com/articles/nphys3619.

Jeffrey A. Nye and Jay T. Groves. Kinetic Control of Histidine-Tagged Protein Surface Density on Supported Lipid Bilayers. *Langmuir*, 24(8):4145–4149, April 2008. ISSN 0743-7463, 1520-5827. doi: 10.1021/la703788h. URL https://pubs.acs.org/doi/10.1021/la703788h.

Patrick W. Oakes, Elizabeth Wagner, Christoph A. Brand, Dimitri Probst, Marco Linke, Ulrich S. Schwarz, Michael Glotzer, and Margaret L. Gardel. Optogenetic control of RhoA reveals zyxin-mediated elasticity of stress fibres. *Nature Communications*, 8(1):15817, June 2017. ISSN 2041-1723. doi: 10.1038/ncomms15817. URL https://www.nature.com/articles/ncomms15817.

Mei Shan Ong, Shuo Deng, Clarissa Esmeralda Halim, Wanpei Cai, Tuan Zea Tan, Ruby Yun-Ju Huang, Gautam Sethi, Shing Chuan Hooi, Alan Prem Kumar, and Celestial T. Yap. Cytoskeletal Proteins in Cancer and Intracellular Stress: A Therapeutic Perspective. *Cancers*, 12(1):238, January 2020. ISSN 2072-6694. doi: 10.3390/cancers12010238. URL https://www.mdpi.com/2072-6694/12/1/238.

Wout Oosterheert, Björn U. Klink, Alexander Belyy, Sabrina Pospich, and Stefan Raunser. Structural basis of actin filament assembly and aging. *Nature*, 611(7935):374–379, November 2022. ISSN 0028-0836, 1476-4687. doi: 10.1038/s41586-022-05241-8. URL https://www.nature.com/articles/s41586-022-05241-8.

Nataliya Panchuk-Voloshina, Rosaria P. Haugland, Janell Bishop-Stewart, Mahesh K. Bhalgat, Paul J. Millard, Fei Mao, Wai-Yee Leung, and Richard P. Haugland. Alexa Dyes, a Series of New Fluorescent Dyes that Yield Exceptionally Bright, Photostable Conjugates.

Journal of Histochemistry & Cytochemistry, 47(9):1179–1188, September 1999. ISSN 0022-1554, 1551-5044. doi: 10.1177/002215549904700910. URL http://journals.sagepub.com/doi/10.1177/002215549904700910.

Pierre Paoletti, Graham C. R. Ellis-Davies, and Alexandre Mourot. Optical control of neuronal ion channels and receptors. *Nature Reviews Neuroscience*, 20(9):514–532, September 2019. ISSN 1471-003X, 1471-0048. doi: 10.1038/s41583-019-0197-2. URL https://www.nature.com/articles/s41583-019-0197-2.

Hyerim Park, Na Yeon Kim, Sangkyu Lee, Nury Kim, Jihoon Kim, and Won Do Heo. Optogenetic protein clustering through fluorescent protein tagging and extension of CRY2. *Nature Communications*, 8(1):30, June 2017. ISSN 2041-1723. doi: 10.1038/s41467-017-00060-2. URL https://www.nature.com/articles/s41467-017-00060-2.

Sung-Jin Park, Mattia Gazzola, Kyung Soo Park, Shirley Park, Valentina Di Santo, Erin L. Blevins, Johan U. Lind, Patrick H. Campbell, Stephanie Dauth, Andrew K. Capulli, Francesco S. Pasqualini, Seungkuk Ahn, Alexander Cho, Hongyan Yuan, Ben M. Maoz, Ragu Vijaykumar, Jeong-Woo Choi, Karl Deisseroth, George V. Lauder, L. Mahadevan, and Kevin Kit Parker. Phototactic guidance of a tissue-engineered soft-robotic ray. *Science*, 353(6295):158–162, July 2016. ISSN 0036-8075, 1095-9203. doi: 10.1126/science.aaf4292. URL https://www.science.org/doi/10.1126/science.aaf4292.

Francine Parker, Thomas G. Baboolal, and Michelle Peckham. Actin Mutations and Their Role in Disease. *International Journal of Molecular Sciences*, 21(9):3371, May 2020. ISSN 1422-0067. doi: 10.3390/ijms21093371. URL https://www.mdpi.com/1422-0067/21/9/3371.

Francesco S. Pasqualini, Alexander P. Nesmith, Renita E. Horton, Sean P. Sheehy, and Kevin Kit Parker. Mechanotransduction and Metabolism in Cardiomyocyte Microdomains. *BioMed Research International*, 2016:1–17, 2016. ISSN 2314-6133, 2314-6141. doi: 10.1155/2016/4081638. URL https://www.hindawi.com/journals/bmri/2016/4081638/.

Pallavi Pushp, Bijayalaxmi Sahoo, Frederico C. Ferreira, Joaquim M. Sampaio Cabral, Ana Fernandes-Platzgummer, and Mukesh K. Gupta. Functional comparison of beating cardiomyocytes differentiated from umbilical cord-derived mesenchymal/stromal stem cells and human foreskin-derived induced pluripotent stem cells. *Journal of Biomedical Materials Research Part A*, 108(3):496–514, March 2020. ISSN 1549-3296, 1552-4965. doi: 10.1002/jbm.a.36831. URL https://onlinelibrary.wiley.com/doi/10.1002/jbm.a.36831.

Dilson E. Rassier. Sarcomere mechanics in striated muscles: from molecules to sarcomeres to cells. *American Journal of Physiology-Cell Physiology*, 313(2):C134–C145, August 2017. ISSN 0363-6143, 1522-1563. doi: 10.1152/ajpcell.00050.2017. URL https://www.physiology.org/doi/10.1152/ajpcell.00050.2017.

Allison Reno, Andrew Hunter, Yang Li, Tong Ye, and Ann Foley. Quantification of Cardiomyocyte Beating Frequency Using Fourier Transform Analysis. *Photonics*, 5(4): 39, October 2018. ISSN 2304-6732. doi: 10.3390/photonics5040039. URL http://www.mdpi.com/2304-6732/5/4/39.

Anne-Cécile Reymann, Jean-Louis Martiel, Théo Cambier, Laurent Blanchoin, Rajaa Boujemaa-Paterski, and Manuel Théry. Nucleation geometry governs ordered actin networks structures. *Nature Materials*, 9(10):827–832, October 2010. ISSN 1476-1122, 1476-4660. doi: 10.1038/nmat2855. URL https://www.nature.com/articles/nmat2855.

Anne-Cécile Reymann, Rajaa Boujemaa-Paterski, Jean-Louis Martiel, Christophe Guérin, Wenxiang Cao, Harvey F. Chin, Enrique M. De La Cruz, Manuel Théry, and Laurent Blanchoin. Actin Network Architecture Can Determine Myosin Motor Activity. *Science*, 336 (6086):1310–1314, June 2012. ISSN 0036-8075, 1095-9203. doi: 10.1126/science.1221708. URL https://www.science.org/doi/10.1126/science.1221708.

Euripedes de Almeida Ribeiro, Nikos Pinotsis, Andrea Ghisleni, Anita Salmazo, Petr V. Konarev, Julius Kostan, Björn Sjöblom, Claudia Schreiner, Anton A. Polyansky, Eirini A. Gkougkoulia, Mark R. Holt, Finn L. Aachmann, Bojan Žagrović, Enrica Bordignon, Katharina F. Pirker, Dmitri I. Svergun, Mathias Gautel, and Kristina Djinović-Carugo. The Structure and Regulation of Human Muscle a-Actinin. *Cell*, 159(6):1447–1460, December 2014. ISSN 00928674. doi: 10.1016/j.cell.2014.10.056. URL https://linkinghub.elsevier.com/retrieve/pii/S0092867414014287.

Leonardo Ricotti, Barry Trimmer, Adam W. Feinberg, Ritu Raman, Kevin K. Parker, Rashid Bashir, Metin Sitti, Sylvain Martel, Paolo Dario, and Arianna Menciassi. Biohybrid actuators for robotics: A review of devices actuated by living cells. *Science Robotics*, 2 (12):eaaq0495, November 2017. ISSN 2470-9476. doi: 10.1126/scirobotics.aaq0495. URL https://www.science.org/doi/10.1126/scirobotics.aaq0495.

Julia Riedl, Alvaro H Crevenna, Kai Kessenbrock, Jerry Haochen Yu, Dorothee Neukirchen, Michal Bista, Frank Bradke, Dieter Jenne, Tad A Holak, Zena Werb, Michael Sixt, and Roland Wedlich-Soldner. Lifeact: a versatile marker to visualize F-actin. *Nature Methods*, 5(7):605–607, July 2008. ISSN 1548-7091, 1548-7105. doi: 10.1038/nmeth.1220. URL http://www.nature.com/articles/nmeth.1220.

Erik A. Rodriguez, Robert E. Campbell, John Y. Lin, Michael Z. Lin, Atsushi Miyawaki, Amy E. Palmer, Xiaokun Shu, Jin Zhang, and Roger Y. Tsien. The Growing and Glowing Toolbox of Fluorescent and Photoactive Proteins. *Trends in Biochemical Sciences*, 42(2): 111–129, February 2017. ISSN 09680004. doi: 10.1016/j.tibs.2016.09.010. URL https://linkinghub.elsevier.com/retrieve/pii/S0968000416301736.

Stephen L. Rogers, Ursula Wiedemann, Nico Stuurman, and Ronald D. Vale. Molecular requirements for actin-based lamella formation in Drosophila S2 cells. *Journal of Cell Biology*, 162(6):1079–1088, September 2003. ISSN 1540-8140, 0021-9525. doi:

10.1083/jcb.200303023. URL https://rupress.org/jcb/article/162/6/1079/33667/Molecular-requirements-for-actinbased-lamella.

Eva Romito, Tarek Shazly, and Francis G. Spinale. In vivo assessment of regional mechanics post-myocardial infarction: A focus on the road ahead. *Journal of Applied Physiology*, 123 (4):728–745, October 2017. ISSN 8750-7587, 1522-1601. doi: 10.1152/japplphysiol.00589.2015. URL https://www.physiology.org/doi/10.1152/japplphysiol.00589.2015.

Paul V. Ruijgrok, Rajarshi P. Ghosh, Sasha Zemsky, Muneaki Nakamura, Rui Gong, Lin Ning, Robert Chen, Vipul T. Vachharajani, Alexander E. Chu, Namrata Anand, Raphael R. Eguchi, Po-Ssu Huang, Michael Z. Lin, Gregory M. Alushin, Jan T. Liphardt, and Zev Bryant. Optical control of fast and processive engineered myosins in vitro and in living cells. *Nature Chemical Biology*, 17(5):540–548, May 2021. ISSN 1552-4450, 1552-4469. doi: 10.1038/s41589-021-00740-7. URL http://www.nature.com/articles/s41589-021-00740-7.

Tatsuya Sakai, Takatoshi Kagawa, Masahiro Kasahara, Trevor E. Swartz, John M. Christie, Winslow R. Briggs, Masamitsu Wada, and Kiyotaka Okada. *Arabidopsis* nph1 and npl1: Blue light receptors that mediate both phototropism and chloroplast relocation. *Proceedings of the National Academy of Sciences*, 98(12):6969–6974, June 2001. ISSN 0027-8424, 1091-6490. doi: 10.1073/pnas.101137598. URL https://pnas.org/doi/full/10.1073/pnas.101137598.

Moussa Saleh and John A Ambrose. Understanding myocardial infarction. *F1000Research*, 7:1378, September 2018. ISSN 2046-1402. doi: 10.12688/f1000research.15096.1. URL https://f1000research.com/articles/7-1378/v1.

Nathan C Shaner, Robert E Campbell, Paul A Steinbach, Ben N G Giepmans, Amy E Palmer, and Roger Y Tsien. Improved monomeric red, orange and yellow fluorescent proteins derived from Discosoma sp. red fluorescent protein. *Nature Biotechnology*, 22 (12):1567–1572, December 2004. ISSN 1087-0156, 1546-1696. doi: 10.1038/nbt1037. URL https://www.nature.com/articles/nbt1037.

Andrew J. Spracklen, Tiffany N. Fagan, Kaylee E. Lovander, and Tina L. Tootle. The pros and cons of common actin labeling tools for visualizing actin dynamics during Drosophila oogenesis. *Developmental Biology*, 393(2):209–226, September 2014. ISSN 00121606. doi: 10.1016/j.ydbio.2014.06.022. URL https://linkinghub.elsevier.com/retrieve/pii/S0012160614003182.

Orrin J. Stone, Neha Pankow, Bei Liu, Ved P. Sharma, Robert J. Eddy, Hui Wang, Andrew T. Putz, Frank D. Teets, Brian Kuhlman, John S. Condeelis, and Klaus M. Hahn. Optogenetic control of cofilin and aTAT in living cells using Z-lock. *Nature Chemical Biology*, 15(12): 1183–1190, December 2019. ISSN 1552-4450, 1552-4469. doi: 10.1038/s41589-019-0405-4. URL http://www.nature.com/articles/s41589-019-0405-4.

Devin Strickland, Keith Moffat, and Tobin R. Sosnick. Light-activated DNA binding in a designed allosteric protein. *Proceedings of the National Academy of Sciences*, 105(31): 10709–10714, August 2008. ISSN 0027-8424, 1091-6490. doi: 10.1073/pnas.0709610105. URL https://pnas.org/doi/full/10.1073/pnas.0709610105.

Devin Strickland, Xiaolan Yao, Grzegorz Gawlak, Michael K Rosen, Kevin H Gardner, and Tobin R Sosnick. Rationally improving LOV domain–based photoswitches. *Nature Methods*, 7(8):623–626, August 2010. ISSN 1548-7091, 1548-7105. doi: 10.1038/nmeth.1473. URL http://www.nature.com/articles/nmeth.1473.

Devin Strickland, Yuan Lin, Elizabeth Wagner, C Matthew Hope, Josiah Zayner, Chloe Antoniou, Tobin R Sosnick, Eric L Weiss, and Michael Glotzer. TULIPs: tunable, light-controlled interacting protein tags for cell biology. *Nature Methods*, 9(4):379–384, April 2012. ISSN 1548-7091, 1548-7105. doi: 10.1038/nmeth.1904. URL http://www.nature.com/articles/nmeth.1904.

Wei-Chun Tang, Yen-Ting Liu, Cheng-Han Yeh, Chieh-Han Lu, Chiao-Hui Tu, Yi-Ling Lin, Yu-Chun Lin, Tsui-Ling Hsu, Liang Gao, Shu-Wei Chang, Peilin Chen, and Bi-Chang Chen. Optogenetic manipulation of cell migration with high spatiotemporal resolution using lattice lightsheet microscopy. *Communications Biology*, 5(1):879, August 2022. ISSN 2399-3642. doi: 10.1038/s42003-022-03835-6. URL https://www.nature.com/articles/s42003-022-03835-6.

Roderick P. Tas, Chiung-Yi Chen, Eugene A. Katrukha, Mathijs Vleugel, Maurits Kok, Marileen Dogterom, Anna Akhmanova, and Lukas C. Kapitein. Guided by Light: Optical Control of Microtubule Gliding Assays. *Nano Letters*, 18(12):7524–7528, December 2018. ISSN 1530-6984. doi: 10.1021/acs.nanolett.8b03011. URL https://doi.org/10.1021/acs.nanolett.8b03011. Publisher: American Chemical Society.

Amir Taslimi, Justin D. Vrana, Daniel Chen, Sofya Borinskaya, Bruce J. Mayer, Matthew J. Kennedy, and Chandra L. Tucker. An optimized optogenetic clustering tool for probing protein interaction and function. *Nature Communications*, 5(1):4925, September 2014. ISSN 2041-1723. doi: 10.1038/ncomms5925. URL https://www.nature.com/articles/ncomms5925.

Amir Taslimi, Brian Zoltowski, Jose G Miranda, Gopal P Pathak, Robert M Hughes, and Chandra L Tucker. Optimized second-generation CRY2–CIB dimerizers and photoactivatable Cre recombinase. *Nature Chemical Biology*, 12(6):425–430, June 2016. ISSN 1552-4450, 1552-4469. doi: 10.1038/nchembio.2063. URL https://www.nature.com/articles/nchembio.2063.

Kathryn Tunyasuvunakool, Jonas Adler, Zachary Wu, Tim Green, Michal Zielinski, Augustin Žídek, Alex Bridgland, Andrew Cowie, Clemens Meyer, Agata Laydon, Sameer Velankar, Gerard J. Kleywegt, Alex Bateman, Richard Evans, Alexander Pritzel, Michael Figurnov, Olaf Ronneberger, Russ Bates, Simon A. A. Kohl, Anna Potapenko, Andrew J. Ballard, Bernardino Romera-Paredes, Stanislav Nikolov, Rishub Jain, Ellen Clancy, David

Reiman, Stig Petersen, Andrew W. Senior, Koray Kavukcuoglu, Ewan Birney, Pushmeet Kohli, John Jumper, and Demis Hassabis. Highly accurate protein structure prediction for the human proteome. *Nature*, 596(7873):590–596, August 2021. ISSN 0028-0836, 1476-4687. doi: 10.1038/s41586-021-03828-1. URL https://www.nature.com/articles/s41586-021-03828-1.

Saranyaraajan Varadarajan, Shahana A. Chumki, Rachel E. Stephenson, Eileen R. Misterovich, Jessica L. Wu, Claire E. Dudley, Ivan S. Erofeev, Andrew B. Goryachev, and Ann L. Miller. Mechanosensitive calcium flashes promote sustained RhoA activation during tight junction remodeling. *Journal of Cell Biology*, 221 (4):e202105107, April 2022. ISSN 0021-9525, 1540-8140. doi: 10.1083/jcb.202105107. URL https://rupress.org/jcb/article/221/4/e202105107/213049/Mechanosensitive-calcium-flashes-promote-sustained.

Andrew P. Voorhees and Hai-Chao Han. Biomechanics of Cardiac Function. In Ronald Terjung, editor, *Comprehensive Physiology*, pages 1623–1644. Wiley, 1 edition, September 2015. ISBN 978-0-470-65071-4. doi: 10.1002/cphy.c140070. URL https://onlinelibrary.wiley.com/doi/10.1002/cphy.c140070.

A. Catalina Vélez-Ortega and Gregory I. Frolenkov. Building and repairing the stereocilia cytoskeleton in mammalian auditory hair cells. *Hearing Research*, 376:47–57, May 2019. ISSN 03785955. doi: 10.1016/j.heares.2018.12.012. URL https://linkinghub.elsevier.com/retrieve/pii/S0378595518304830.

Elizabeth Wagner and Michael Glotzer. Local RhoA activation induces cytokinetic furrows independent of spindle position and cell cycle stage. *Journal of Cell Biology*, 213(6):641–649, June 2016. ISSN 0021-9525, 1540-8140. doi: 10.1083/jcb.201603025. URL https://rupress.org/jcb/article/213/6/641/38641/Local-RhoA-activation-induces-cytokinetic-furrows.

Hui Wang, Marco Vilela, Andreas Winkler, Miroslaw Tarnawski, Ilme Schlichting, Hayretin Yumerefendi, Brian Kuhlman, Rihe Liu, Gaudenz Danuser, and Klaus M Hahn. LOVTRAP: an optogenetic system for photoinduced protein dissociation. *Nature Methods*, 13 (9):755–758, September 2016. ISSN 1548-7091, 1548-7105. doi: 10.1038/nmeth.3926. URL https://www.nature.com/articles/nmeth.3926.

Yanwen Wang, Wee Khang Lin, William Crawford, Haibo Ni, Emma L. Bolton, Huma Khan, Julia Shanks, Gil Bub, Xin Wang, David J. Paterson, Henggui Zhang, Antony Galione, Steven N. Ebert, Derek A. Terrar, and Ming Lei. Optogenetic Control of Heart Rhythm by Selective Stimulation of Cardiomyocytes Derived from Pnmt+ Cells in Murine Heart. *Scientific Reports*, 7(1):40687, January 2017. ISSN 2045-2322. doi: 10.1038/srep40687. URL https://www.nature.com/articles/srep40687.

Steven M. White, Phillip E. Constantin, and William C. Claycomb. Cardiac physiology at the cellular level: use of cultured HL-1 cardiomyocytes for studies of cardiac muscle cell structure and function. *American Journal of Physiology-Heart and Circulatory Physiology*,

286(3):H823–H829, March 2004. ISSN 0363-6135, 1522-1539. doi: 10.1152/ajpheart.00986.2003. URL https://www.physiology.org/doi/10.1152/ajpheart.00986.2003.

Jonathan D. Winkelman, Cristian Suarez, Glen M. Hocky, Alyssa J. Harker, Alisha N. Morganthaler, Jenna R. Christensen, Gregory A. Voth, James R. Bartles, and David R. Kovar. Fascin- and a-Actinin-Bundled Networks Contain Intrinsic Structural Features that Drive Protein Sorting. *Current Biology*, 26(20):2697–2706, October 2016. ISSN 09609822. doi: 10.1016/j.cub.2016.07.080. URL https://linkinghub.elsevier.com/retrieve/pii/S0960982216308740.

Rui Xu and Shaojun Du. Overexpression of Lifeact-GFP Disrupts F-Actin Organization in Cardiomyocytes and Impairs Cardiac Function. *Frontiers in Cell and Developmental Biology*, 9:746818, October 2021. ISSN 2296-634X. doi: 10.3389/fcell.2021.746818. URL https://www.frontiersin.org/articles/10.3389/fcell.2021.746818/full.

Xiaolan Yao, Michael K Rosen, and Kevin H Gardner. Estimation of the available free energy in a LOV2-Ja photoswitch. *Nature Chemical Biology*, 4(8):491–497, August 2008. ISSN 1552-4450, 1552-4469. doi: 10.1038/nchembio.99. URL https://www.nature.com/articles/nchembio.99.

Josiah P. Zayner and Tobin R. Sosnick. Factors That Control the Chemistry of the LOV Domain Photocycle. *PLoS ONE*, 9(1):e87074, January 2014. ISSN 1932-6203. doi: 10.1371/journal.pone.0087074. URL https://dx.plos.org/10.1371/journal.pone.0087074.

Josiah P. Zayner, Tilo Mathes, Tobin R. Sosnick, and John T. M. Kennis. Helical Contributions Mediate Light-Activated Conformational Change in the LOV2 Domain of *Avena sativa* Phototropin 1. *ACS Omega*, 4(1):1238–1243, January 2019. ISSN 2470-1343, 2470-1343. doi: 10.1021/acsomega.8b02872. URL https://pubs.acs.org/doi/10.1021/acsomega.8b02872.

Josiah P. Zayner, Chloe Antoniou, Alexander R. French, Ronald J. Hause, and Tobin R. Sosnick. Investigating Models of Protein Function and Allostery With a Widespread Mutational Analysis of a Light-Activated Protein. *Biophysical Journal*, 105(4):1027–1036, August 2013. ISSN 00063495. doi: 10.1016/j.bpj.2013.07.010. URL https://linkinghub.elsevier.com/retrieve/pii/S0006349513007935.

Jianhua Zhang, Gisela F. Wilson, Andrew G. Soerens, Chad H. Koonce, Junying Yu, Sean P. Palecek, James A. Thomson, and Timothy J. Kamp. Functional Cardiomyocytes Derived From Human Induced Pluripotent Stem Cells. *Circulation Research*, 104(4), February 2009. ISSN 0009-7330, 1524-4571. doi: 10.1161/CIRCRESAHA.108.192237. URL https://www.ahajournals.org/doi/10.1161/CIRCRESAHA.108.192237.

Zijian Zhang, Nicolas Denans, Yingfei Liu, Olena Zhulyn, Hannah D. Rosenblatt, Marius Wernig, and Maria Barna. Author Correction: Optogenetic manipulation of cellular communication using engineered myosin motors. *Nature Cell Biology*, 23(3):293–293, March 2021. ISSN 1465-7392, 1476-4679. doi: 10.1038/s41556-021-00650-9. URL https://www.nature.com/articles/s41556-021-00650-9.

Brian D. Zoltowski, Carsten Schwerdtfeger, Joanne Widom, Jennifer J. Loros, Alexandrine M. Bilwes, Jay C. Dunlap, and Brian R. Crane. Conformational Switching in the Fungal Light Sensor Vivid. *Science*, 316(5827):1054–1057, May 2007. ISSN 0036-8075, 1095-9203. doi: 10.1126/science.1137128. URL https://www.science.org/doi/10.1126/science.1137128.

Brian D Zoltowski, Brian Vaccaro, and Brian R Crane. Mechanism-based tuning of a LOV domain photoreceptor. *Nature Chemical Biology*, 5(11):827–834, November 2009. ISSN 1552-4450, 1552-4469. doi: 10.1038/nchembio.210. URL https://www.nature.com/articles/nchembio.210.